Surface Orientation Dependent Corrosion Damage and Temperature Dependent Mechanical Property Degradation of Sensitized AA5083-H116 Alloys

Robert Jeffrey Mills

Dissertation submitted to the faculty of the Virginia Polytechnic Institute and State University in partial fulfillment for of the requirements for the degree of

Doctor of Philosophy
In
Materials Science and Engineering

Scott W. Case
Brian Y. Lattimer
Sean G. Corcoran
Alan P. Druschitz

September 21, 2018
Blacksburg, VA

Keywords: 5XXX aluminum, sensitization, corrosion damage, surface orientation, sensitization-corrosion mechanical response

Surface Orientation Dependent Corrosion Damage and Temperature Dependent Mechanical Property Degradation of Sensitized AA5083-H116 Alloys

Robert Jeffrey Mills

Abstract

This study relates the sensitization process microstructural changes of 5083-H116 to its resulting corrosion resistance and mechanical performance. Alcoa 5083-H116 was sensitized in an environmental chamber at 100°C for up to ~1500 hours and 150°C up to ~2000 hours, revealing different degrees of sensitization based on exposure times. Microstructural characterization was conducted on etched sensitized samples. Additionally, samples were subjected to accelerated corrosion scenarios for subsequent microstructural examination and subsequent mechanical (tension and tensile creep) testing. To connect the laboratory studies to the field exposure, Novelis 5083-H116 was sensitized at 100°C; dog bone samples were created and exposed for two years in a beach environment to investigate possible sensitization and corrosion effects. It was found that the sensitization at 100°C and 150°C of Alcoa 5083-H116 led to recrystallization from the as-received (AR) state of the material (3 mg/cm²). The degree of sensitization of 61 mg/cm² recrystallized the grain size the most from the AR state. The higher sensitization temperature of 150°C caused higher thickness loss and mass-loss rates (MR) for the intergranular corrosion (IGC) susceptible sensitization levels. Accelerated corrosion on different surface orientations led to different corrosion mechanisms (parallel IGC vs. perpendicular IGC). While 5083-H116 material corroded on the rolled surface led to a uniform exfoliation damage on 150°C sensitization exposure, the 100°C rolled surface only exhibited pitting corrosion damage. The through plate thickness corrosion damage, however, exhibited a corrosion susceptible-resistant-susceptible (C-SRS) pattern. Mechanical properties were assessed for the various conditions in terms of room temperature tension testing and elevated temperature creep tests. Sensitization affected yield strength but did not play a role in ultimate tensile strength. The presence of corrosion damage lowered yield strength and ultimate tensile strength of the IGC susceptible sensitized 5083-H116, with the through thickness corrosion damage reducing the properties more than corrosion of the rolled surface. Material sensitized at 150°C and then corroded had a greater reduction in room temperature mechanical properties. Creep testing was performed at elevated temperatures, and it was found the solely sensitized 5083-H116 at 100°C or 150°C behaved the same as as-received

5083-H116. When corrosion damage was introduced, creep rupture times and secondary creep rates were changed. Once the corroded section area was accounted for, no significant difference in Larson-Miller parameters was observed.

Surface Orientation Dependent Corrosion Damage and Temperature Dependent Mechanical Property Degradation of Sensitized AA5083-H116 Alloys

Robert Jeffrey Mills

General Audience Abstract

Aluminum is frequently replacing steel in the hulls of U.S. and Australians naval ships. It is preferred because of its lower density than steel and higher corrosion resistance which reduces the need to paint topside surfaces. However, when aluminum alloys that are used in ship construction are exposed to elevated temperatures, the corrosion resistance ca be considerably decreased. Furthermore, fire resistance is always a concern on naval ships. Accordingly, we are interested in predicting how aluminum ships that may have previously corroded respond to fires. In this study, a laboratory technique was used to speed up the corrosion process of these ship hull aluminum alloys. Some samples were thermally exposed in the laboratory for microscopic analysis, corrosion testing, and subsequent mechanical testing. To connect the laboratory studies to the field exposure, thermally exposed samples were placed on a beach for two years to investigate further environmental damages. It was found that the laboratory thermal exposure weakened the aluminum alloy. The thermally exposed alloys were weakened to the corrosion process. Different surfaces of the thermally exposed plates had different corrosion damage mechanisms. Mechanical properties were assessed for the various conditions in terms of room temperature tension testing and elevated temperature creep tests. Thermal exposure affected yield strength (the ability of the material to stretch) but did not play a role in ultimate tensile strength (maximum strength prior to breaking). The presence of corrosion damage lowered yield strength and ultimate tensile strength of the corrosion susceptible thermally exposed alloy. Creep testing (constant applied stress testing) was performed at elevated temperatures (representative of fire damage scenarios), and it was found that the solely thermally exposed alloy behaved the same as as-received alloy in terms of failure mechanisms. When corrosion damage was introduced, creep rupture times (time until material fails by breaking into two pieces) was reduced. Once the corrosion damage was accounted for, mechanical properties could be more accurately represented, and failure times (conditions in the alloy needs to be replaced on ships) were predicted for the alloy.

Dedication

For Kirsten, your love, support, and presence helped me near the end of my PhD journey. I admire your kindheartedness and comfort from our relationship through the unexpected challenges during my dissertation writing.

For my parents, you helped guide me early in life and your love and support has led to me go to VT and beyond. You both inspired me greatly from a young age and pushed me to strive for excellence in all aspects of my life. Your presence during undergraduate education, MS research, and PhD research helped me conquer this challenge and surpass my own expectations to become a doctor.

For my grandparents, all three of you helped ensure I did well in school and life through your love towards me. Grandpa Mills and Grandma Mills, being in your presence, seeing your unbreakable work ethic, and watching Jeopardy as a small child with you created my desire for a pursuit in higher education. Grandma Riddle, your company and resilience helped guide me to navigate the world no matter what life threw at me. I'm glad to have been able to spend as much earthly time with each of you and I dedicate this dissertation in memory of all three of you.

For my friends and family, you all have supported me over the years and helped me stay sane during my education and life pursuits. All of my cousins (too many to name), you are all wonderful and always fun to be around. My brothers (non-biological), Greg, Josh, and Michael, our times hanging out, watching cartoons, and playing video games are some of my best memories. To my collegiate family, Marc, Ben, Derek, and Shelby, our times hanging out, discussing life and research, and tearing up the dance floor will always be with me. My sister (non-bilogical) and former roommate, Megan, you are a good role model and you helped me finish my research.

Acknowledgements

The following list is for all of the people who helped me along the way through advice, conversation, or experimental setup.

Dr. Scott Case, your support and guidance over the past few years has helped me grow as a student of engineering and as a person. Our conversations about research and what I can do to improve my research and how I present my work has encouraged me to work harder and become a better researcher.

Dr. Brian Lattimer, I'm very grateful to you for picking me up in the Extreme Lab initially and for all of your support and guidance since summer 2014. Your knowledge of fire related material testing was detrimental to my progress and PhD research.

Dr. Sean Corcoran, your corrosion course and knowledge of corrosion inspired me and sparked my interest in corrosion for my PhD research.

Dr. Alan Druschitz, your knowledge of physical metallurgy and support over the years inspired my interest in learning more about the microstructure of my alloy during my PhD research.

Dr. Patrick Summers, I'm very grateful to you especially for picking me for an interview in summer 2014 and for guiding me for nearly a year in how to be a better researcher through experiments and our conversations.

Dr. Adrian Mouritz, your communications and collaboration helped ensure my publication in Corrosion Science.

Mac McCord, I greatly value your knowledge and training on Instron and MTS machines. Without your help, my creep experiments would have unsuccessful.

Office of Naval Research, my research was possible thanks to funding through grant N000141310590.

Australian DSTO (Zenka Mathys, Veronica Jeleniewski, Ian Burch), your support and implementation of the Novelis 5083-H116 Cowley Beach exposure helped ensure Chapter 8 of my dissertation was possible.

Dr. Joe Starr, your support over the years and initial introduction to the Extreme lab helped inspire me to get my PhD.

Dr. Christian Rippe, your presence and help with random pieces of equipment like the MTS load frame and the induction heating system helped ensure my research was a success.

Dr. Jonathan Hodges, your friendship, knowledge, and willingness to listen to me rant about my research endeavor was invaluable. Your support with the DIC system was very enlightening as well.

Manuel Umanzor, your assistance in discussions about etching metal alloys and your help with SEM characterization was greatly appreciated.

Taylor Pesek, for helping me machine dog bones from time to time and for your insight into the machining process.

Marc Thompson, your support and time when working on my qualifier, pre-lim, and practice defense were greatly appreciated and you pushed me to think critically when explaining my research.

Stefan Kraft, our conversations about materials science and how to perform research was fun and motivational.

Yuqin Li, your presence and disposition for letting me talk about my research and help in the lab was greatly appreciated.

Maggie Goetz, your support with DIC speckling and creep experiment discussions were invaluable.

Doug Hartley, your help with etching and corrosion experiments and willingness to learn motivated me to be a better researcher and engineer.

Table of Contents

List of Figures

List of Tables

1 Introduction

Naval vessels throughout the world require light-weight, high-strength corrosion resistant alloys to comprise main structural and hull components and increase performance. Specifically, the US Navy's Littoral Combat Ships, Joint High Speed Vessels, and Ship-to-Shore Connectors, along with AUS naval ships of the Armidale class use 5XXX aluminum alloys because of their superior properties [1], [2]. However, one performance limitation of these alloys is associated with temperature sensitivity or sensitization. In particular, 5083, 5456, and their tempers are widely used alloys which experience this problem. Sensitization occurs in 5XXX aluminum alloys with >3% Mg content by altering the microstructure for corrosion susceptibility in the sea environment [3]. For 5083-H116 specifically, sensitization occurs from long-term exposure to elevated temperatures in the range of 40-200ºC, which cause β (Al_3Mg_2) phase nucleation and grain growth along α phase grain boundaries (GB) [3]–[6]. The sensitization effect may result from heat from many sources, such as engine heat, solar radiation, and damage from fires. This problem became further recognized in the early 2000s when more than 200 vessels containing 5083-H321 aluminum were diagnosed as susceptible to intergranular corrosion (IGC) [4]. During exposure in the corrosive saltwater environment, the anodic β phase is preferentially attacked compared to the α aluminum matrix, leading to lifetime degradation of the alloy in terms of atmospheric, pitting, exfoliation damage, IGC, and/or stress-corrosion cracking (SCC) [7], [8]. Various factors that could alter the extent of corrosion damage are sensitization temperature and time, exposed surface orientation, β phase coverage along GB, grain size alterations, and corrosive environment content/exposure time. An improved understanding of the relationships among sensitization, corrosion, microstructure, and mechanical properties can lead to more defined removal parameters for damaged 5083-H116 in naval vessels.

2 Theoretical Background and Related Work

2.1 5XXX Alloy Microstructure-Property Relationships

2.1.1 Chemical Composition

Shipbuilding requires a high-strength, light-weight alloy that resists corrosion damage. Typically, 5XXX alloys are chosen for these components. Various elements are added to pure aluminum to improve properties such as strength and hardness. In 5XXX alloys, magnesium (Mg), manganese (Mn), zinc (Zn), silicon (Si), chromium (Cr), and iron (Fe) are most abundant, and there are trace amounts of nickel (Ni) and copper (Cu) [9]. Magnesium is the main alloying constituent ranging from 1-5 wt%; it is added to aluminum strengthen the solid solution and improve hardening ability [9], [10]. Manganese is added to improve strength and control grain structure, while zinc is added to improve the strength slightly, and with other elements like magnesium, it can help control the aging process [11]. Silicon is generally added to an aluminum alloy to reduce the melting temperature and improve fluidity [12]. Chromium can help control grain size, prevent recrystallization, and affect electrical resistivity [11]. Iron generally appears in aluminum as an impurity but can also slightly improve strength of the 5XXX alloys [10].

2.1.2 Phases and Precipitates

Figure 2-1 illustrates the phase diagram for an Al-Mg binary system. The notable phases present in 5XXX alloys at temperatures below 450°C are α (aluminum) and β (Al_3Mg_2) phases [13]. Aluminum has a face-centered-cubic (FCC) crystal structure, magnesium has a hexagonal closed-packing crystal structure, and the β phase has a complex FCC crystal structure [13]–[15]. The solubility of Mg in Al is 18.6% at the eutectic temperature, so in 5XXX alloys, magnesium will be soluble in Al, and the β phase will be a stable phase below 450°C (1173 K) [16], [17]. Other phases are present in the Al-Mg phase diagram, but are less important since 5XXX alloys have lesser amounts of Mg.

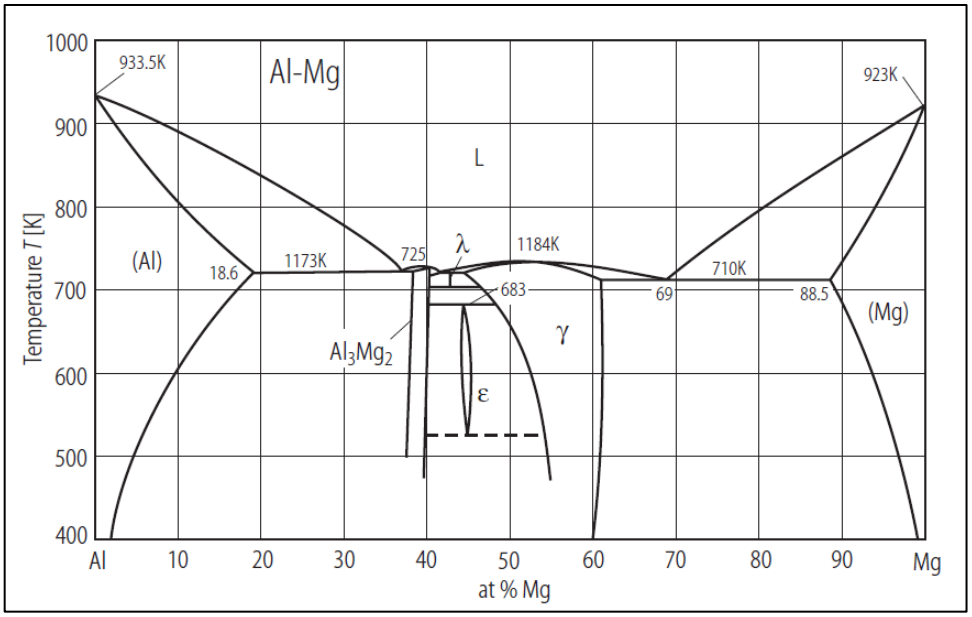

Figure 2-1 Aluminum-magnesium phase diagram [17]. [Reproduced with permission]

An example of the expected amounts of α and β for 5083 alloys is presented in Figure 2-2. Using a tie-line and the lever rule for 4.4% Mg, it is found that 93% Mg is dissolved in solution as part of the aluminum α matrix and that 7% is precipitated in the β phase at 150ºC [12]. This β percentage and morphology, combined with exposure to heat, contributes to corrosion damage to the corrosion resistant 5083-H116.

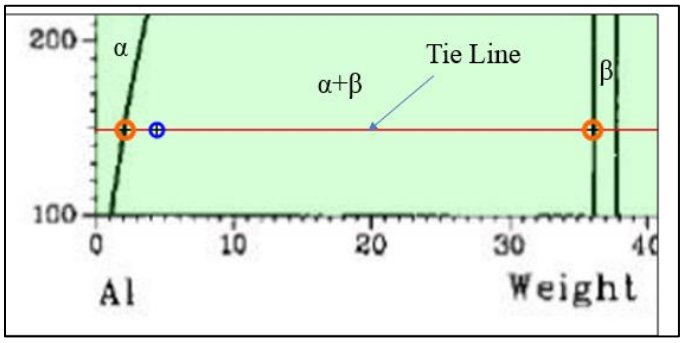

Figure 2-2 Example of α and β amounts at 150ºC for 5083-H116 using a tie-line and the lever rule [16], [18], [19]. [Reproduced with permission]

Along with the β precipitate, 5XXX alloys contain other elements in addition to Al and Mg; thus, other precipitates can be found throughout the microstructure. The following five precipitates were found in 5083 in the as-received (AR) state: Al-(Fe,Si,Mn,Cr), $Al_{13}Fe_4$, Mg_2Si, Al3Mn_2, and Al_6Mn, with the latter four illustrated in Figure 2-3 [7], [20]. Goswami et al. also found Al_6(Mn-Cr-Fe) and Mg_3(Mn-Cr)$_2Al_{18}$ to be present in the AR state of 5083 alloys [21]. The presence, size,

and location of these precipitates contributes to the corrosion damage and mechanical properties exhibited by 5083 at room and elevated temperatures. The nobility or activity of the phase or precipitate depends upon its chemical composition.

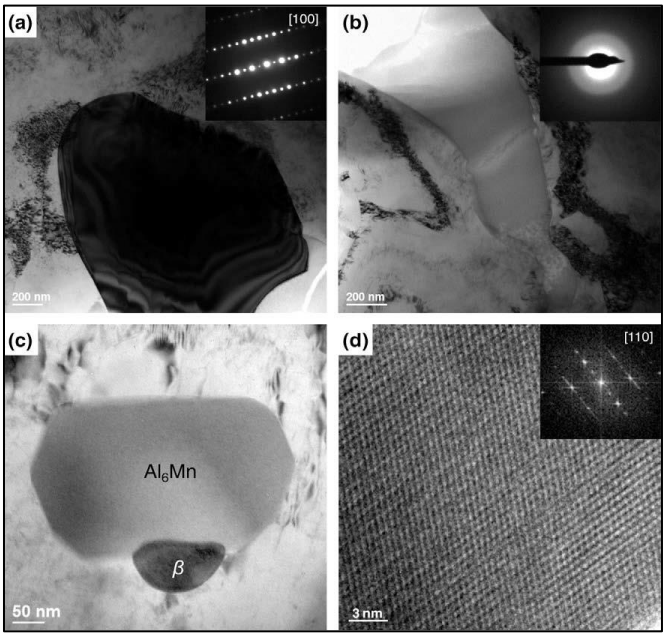

Figure 2-3 Precipitates in AR 5083 Al, a. $Al_{13}Fe_4$, b. Mg_2Si, c. Al_6Mn and Al_3Mg_2, and d. Al_6Mn [20]. [Reproduced with permission]

2.1.3 Grain Structure

To further strengthen the alloy in addition to the contributions of additive elements, deformation from cold-rolling is utilized to strain harden the 5XXX alloy. 5XXX are strain-hardened alloys, so more cold working will increase their strength and hardness values [22]. Figure 2-4 highlights the effects of the rolling process on the granular structure of the metal demonstrating that unworked crystals become compressed and are flattened into elongated ellipsoid shapes.

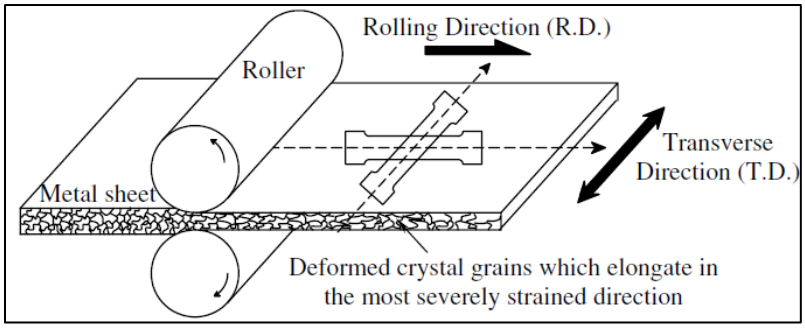

Figure 2-4 Cold working of a metallic alloy [23]. [Reproduced with permission]

Figure 2-5 illustrates the 3-D microstructure of AR 5083-H116 with only the effects of cold-rolling present. Three surface directions—L (longitudinal), S (short transverse), and T (long transverse)—are notable in the figure. These directions are combined to describe three surface orientations; LT (the rolling direction—longitudinal long transverse), LS (the through thickness—longitudinal short transverse), and TS (long transverse short transverse) [3], [24]. Without solution heat treatment and quenching, the alloy will retain this grain structure after the combination of cold working and sensitization processes. Previous studies of sensitization utilized solution heat treatments to remove the effects of cold working prior to the sensitization procedure [3], [5], [8], [20], [25]–[35]. Other studies utilized the 5XXX aluminum alloy in a non-recrystallized or heterogeneous state prior to any sensitization, corrosion, or mechanical property testing [36]–[62].

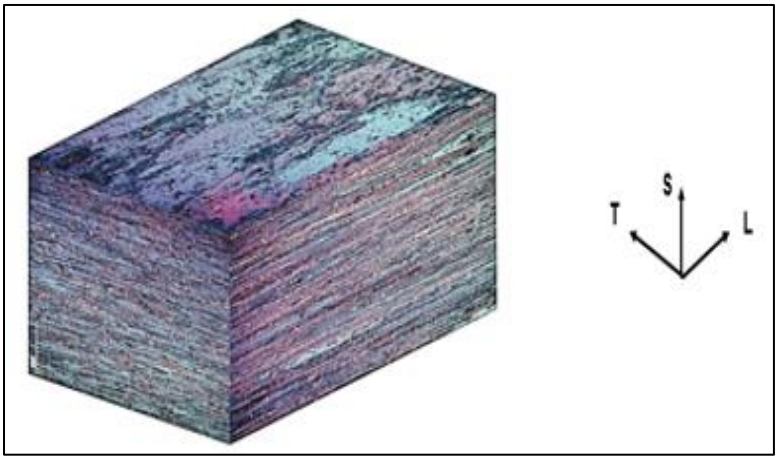

Figure 2-5 AA5083-H116 AR grain structure with emphasis on all three planar surface orientations [24], [63]. [Reproduced with permission]

2.2 Sensitization of 5XXX Alloys

Sensitization temperatures ranging from 40°C to 200°C can create differences in the β phase morphology and precipitation along the GB [3]–[6]. For 5083 alloys, the 4.5 wt% Mg concentration leads to the nucleation and growth of β phase along GB due to the solubility limits of Mg below 200ºC. Phase diagrams can help account for the undissolved β percentage at equilibrium. However, they do not fully account for the sensitization effect, which is a time/temperature dependent diffusion process. The degree of sensitization (DoS) is determined using the approach of ASTM G67: the Nitric Acid Mass-Loss Test (NAMLT) [64].This standard employs a 24 hour soak of the sensitized material in nitric acid; the pre-soak and post-soak weights of the sample allow mass-loss calculations. The mass-loss values are presented with units of

mg/cm², which is a mass-loss per surface area measurement. Figure 2-6 illustrates the mass lost for 5083-H116 and 5083-H131 alloys from Holtz et al., who tested the effects of sensitization levels at 70ºC, 100 ºC and 175ºC on corrosion fatigue of AA5083-H131 [57], from Lim et al., who investigated the effects of sensitization at 80ºC and 100ºC with respect to intergranular corrosion penetration and rates for AA5083-H131 [25], and Tan et al., who investigated the effects of thermomechanical treatment (TMT) and sensitization at 100°C on AA5083-H116 [20]. The data presented in Figure 2-6 were collected on alloys subjected to various solution heat treatments prior to sensitization, indicating the presence of a recrystallized equi-axial grain structure before the NAMLT tests were conducted.

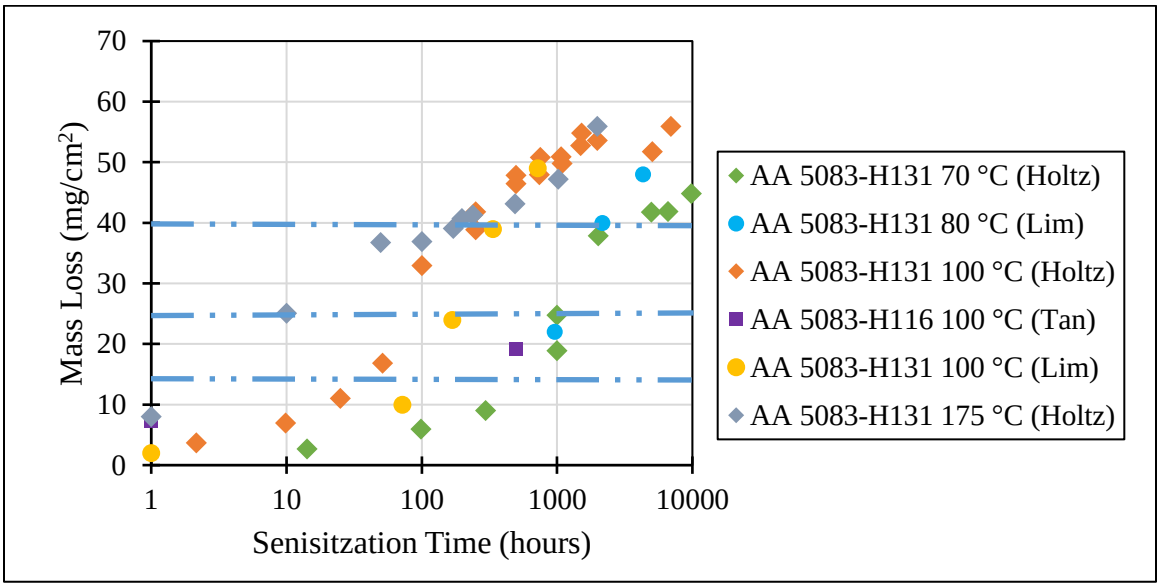

Figure 2-6 NAMLT results for 5083-H131 and 5083-H116 from Holtz et al. [57], Lim et al. [25], and Tan et al. [20].

Prior work suggests different sensitization thresholds, which will directly affect whether a corrosion resistant or corrosion susceptible microstructure will be present in saltwater solutions [25], [28], [49]. Lim et al. reported extensive corrosion damage only above 24 mg/cm² [25]. Davenport et al. found that NAMLT values of 26 mg/cm² or less corresponded to a corrosion resistant microstructure for samples sensitized at 150ºC [28]. Oguocha et al. discovered that for a DoS of 15 mg/cm² or lower, the AA5083-H116 alloy is corrosion resistant, and for a DoS greater than 25 mg/cm², the alloy becomes intergranular corrosion susceptible [49]. Figure 2-7 presents the results from Oguocha et al.'s sensitization of non-homogenized AA5083-H116 at temperatures ranging from 80ºC to 200ºC. Oguocha also noted that mass loss decreased at 200ºC.

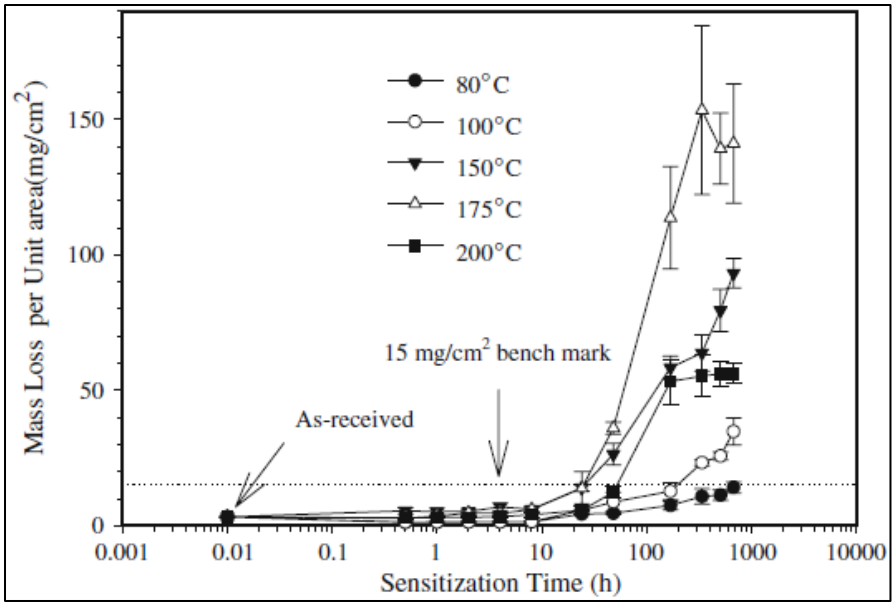

Figure 2-7 NAMLT of AA5083-H116 sensitized at temperatures 80°C, 100°C, 150°C, 175°C, and 200°C [49]. [Reproduced with permission]

Zhang et al. presented a contour map based on various studies of sensitization of 5083 and correlated sensitization time, sensitization temperature, DoS, and β diffusion (kinetics and thermodynamics) [65]. Four distinct regions are illustrated in Figure 2-8 from this set of studies. Region I represents the low-temperature and short-sensitization time in which the equilibrium volume fraction was high, but precipitation was low. Region II represents high-temperature and low sensitization time, suggesting a low equilibrium β volume fraction due to the alloy being near the solvus temperature. Region III represents the IGC susceptible temperatures ranging from 110ºC to 160ºC, where a balance of kinetics and thermodynamics was present [65]. In this temperature range, Zhang noted that a medium but not maximum diffusion rate was present, and a medium, but not minimum equilibrium β phase was present. The last region, Region IV, represents the low-temperature (<50ºC) and long sensitization time, which led to the highest equilibrium β fraction and highest DoS. Based on his contour map, different temperature and time combinations can lead to the "same" DoS. However, this DoS value can be attributed to different equilibrium volume fractions of β and different β phase precipitation morphologies. An example would be sensitizing the alloy at 100°C for 20 days and 150°C for 5 days, both of which lead to a DoS of around 30 mg/cm², but the volume fraction and precipitation size and continuity could be different at each condition.

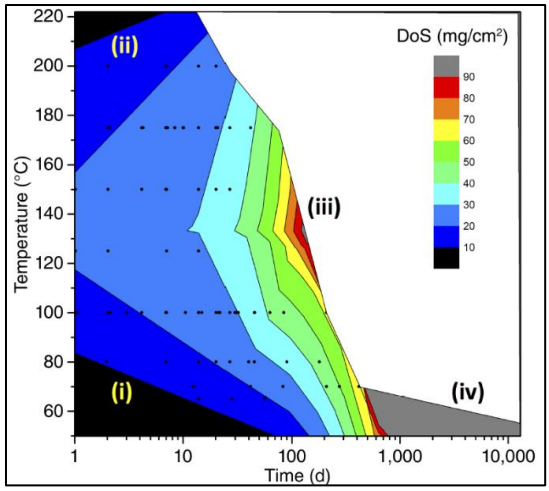

Figure 2-8 Contour map of DoS for sensitization time and temperature [65]. [Reproduced with permission]

2.3 Corrosion

Once 5XXX alloys have been sensitized, corrosion damage is inevitable in certain environments. Corrosion is a destructive electrochemical process in which metal reacts to its environment. Table 2-1 contains an excerpt from the standard electromotive force (EMF) series. Reactions that are more positive on the scale are considered noble, while the more negative reactions are termed active. The severity of the nobleness or activeness depends on the potential reaction. For example, magnesium is more active than aluminum as indicated by the potentials.

Table 2-1 Standard EMF Series [8].

Reaction	V
$2H^+ + 2e^- = H_2$	0.000
$Pb^{2+} + 2e^- = Pb$	-0.126
Sn^{2+} $2e^- = Sn$	-0.138
Ni^{2+} $2e^- = Ni$	-0.250
$Co^{2+} + 2e^- = Co$	-0.277
Cd^{2+} $2e^- = Cd$	-0.403
$2H_2O + 2e^- = H_2 + 2OH^-$ (pH 7)	-0.413
Fe^{2+} $2e^- = Fe$	-0.447
$Cr^{3+} + 3e^- = Cr$	-0.744
$Zn^{2+} + 2e^- = Zn$	-0.762
$2H_2O + 2e^- = H_2 + 2OH^-$ (pH 14)	-0.828
$Al^{3+} + 3e^- = Al$	-1.662
$Mg^{2+} + 2e^- = Mg$	-2.372
$Na^+ + e^- = Na$	-2.71
$K^+ + e^- = K$	-2.931

2.3.1 Classifications

Various types of corrosion can occur in 5XXX aluminum alloys. The types of corrosion damage relevant to this research are atmospheric corrosion, pitting corrosion, intergranular corrosion (IGC) (which includes exfoliation), and environmentally induced cracking (EIC). The following sections briefly describe these types of corrosion damage and their relation to 5XXX series aluminum alloys.

2.3.1.1 Atmospheric

Atmospheric corrosion is the most visible example of uniform surface corrosion damage [8]. Atmospheric corrosion is corrosion damage from air or moisture in the air. Some of the atmospheric parameters that affect the severity of atmospheric corrosion are temperature, moisture, rainfall, solar radiation, and pollutants (such as chlorides) [66]. In ship applications, 5XXX alloys will experience temperature changes, moisture condensation, solar radiation, and chloride contamination at sea. The four types of atmospheric corrosion are rural, urban, industrial, and marine [67]. Marine corrosion is the most common for 5XXX alloys; it can occur from ocean spray, splashing, or seawater immersion of various parts of ships. Chloride ions from sodium chloride tend to be the main problem in marine atmospheres for metals, especially at humidity levels higher than 55% [66]. Figure 2-9 presents a schematic for the cathodic and anodic reactions that occur on a metal due to the presence of a thin film.

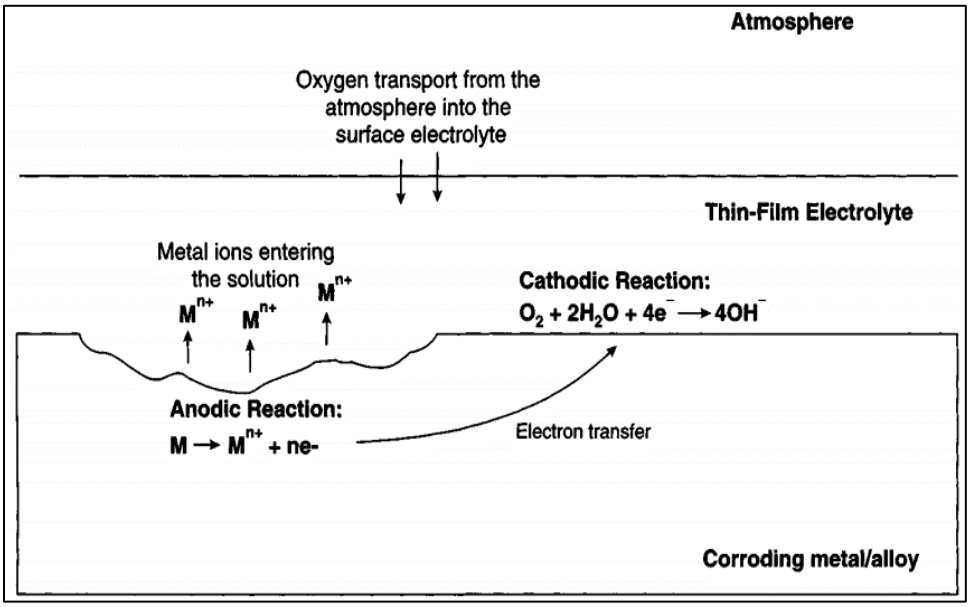

Figure 2-9 Atmospheric corrosion on metal/alloy schematic [67]. [Reproduced with permission]

The cathodic reaction occurs as the oxygen reduction reaction, while the anodic oxidation reaction is the dissolution of the metal [67]. The atmospheric corrosion occurs based on a balance of these two reactions and the thin film presence, with high concentrations of chlorides from seawater, for example. However, it should be noted that the oxygen diffusion into the electrolyte film has a limited current density and can only penetrate into an electrolyte layer thickness of <30 μm [68]. Due to the nature of the oxygen penetration, atmospheric corrosion damage is believed to be controlled by the anodic oxidation reaction. Since most aluminum alloys have a passive film, localized attack is expected. For aluminum and aluminum alloys, atmospheric corrosion begins with a stain from condensation; the 5XXX series is highly susceptible to this contaminant staining due to the presence of a magnesium oxide film [69]. Studies by Patterson and Wilkinson demonstrated that the humidity, temperature, and period of exposure lead to higher corrosion rates for aluminum than immersion of the aluminum in certain electrolytes [70].

2.3.1.2 Pitting

With the presence of precipitants and various phases, localized corrosion damage in the form of pitting is likely. For 5XXX aluminum alloys, differences in the heterogeneous microstructure and the pH of saltwater solutions cause pitting [71]. Different precipitates will affect the oxidation protective layer with a β phase or other anodic phase presences on the surface leading to localized pitting. Figure 2-10 illustrates the pitting damage of a 5083 sample after immersion in synthetic seawater. Thus, a mismatch between the anodic β phase and noble aluminum matrix leads to the anodic and cathodic reactions mentioned previously. Consequently, most studies have focused on β phase corrosion [3], [5], [28], [72].

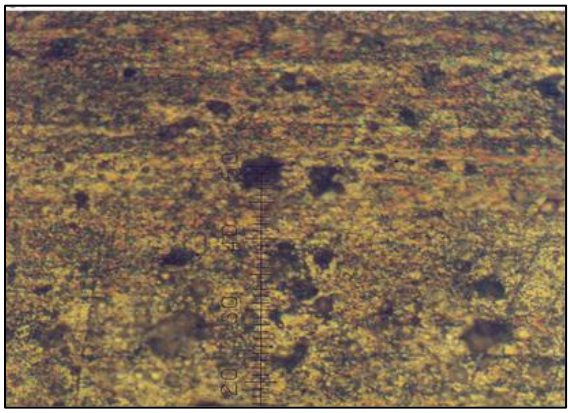

Figure 2-10 Pitting of 5083 alloy after a potentiodynamic scan in a salt water solution at room temperature [73].

To discuss pitting, some specialized terminology is needed and can be obtained from a potentiodynamic (PD) scan of a material (aluminum in this case). Pure aluminum and AA2024 potentiodynamic are illustrated in Figure 2-11. The cathodic region of the pure aluminum is below the teal line and the anodic region is above the teal line. The intersection of these two light blue curves gives the corrosion potential (E_{corr}). The passive region of the pure aluminum ranges from the teal line to the red line. The metastable pitting region of the pure aluminum is the vertical portion of the curve from the red line to the green line [74]. The green line across the pure aluminum curve identifies the breakdown potential (E_{br}) or pitting potential (E_{pitt}). The spreading potential (E_{spr}) is defined as corrosion that spreads across the surface; it is obtained from the intersection of the two dark blue lines for the AA2024-T3 alloy curve [3], [74]. The E_{spr}, E_{pitt}, and E_{br} acronyms can be used interchangeably; depending on the corrosion and material interaction, the E_{spr} is less distinct due to surface heterogeneity.

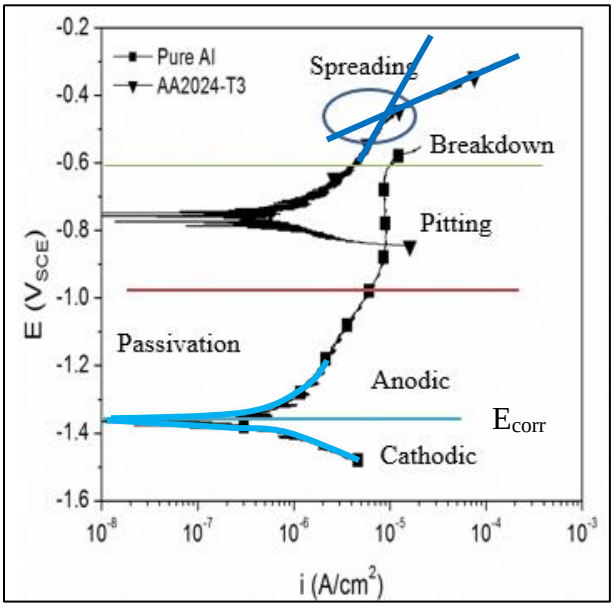

Figure 2-11 Potentiodynamic scan of pure Al and AA2024-T3 [74].

Studies suggest that the spreading potential of AA5083 is -0.73V_{SCE}, while the anodic potential of β can range from 200 to 500 mV less noble than 5083 [3], [45], [57]. Based upon the sensitization time and temperature, the amount of β phase present along GB will contribute to pitting or spreading IGC damage. At lower sensitization levels, pitting is expected. Pitting is still likely to occur at high DoS; however, the active β is along the GB, and the initiation of IGC can occur from spreading damage.

2.3.1.3 IGC and Exfoliation

With 5XXX series aluminum alloys, one of the more well-known types of corrosion damage is IGC. This type of corrosion stems from metallurgical differences in an alloy that lead to preferential corrosion attacks along the GB. For sensitized 5XXX series, this arises from preferential attack of the anodic β phase along GB. Intergranular corrosion damage can be thought of as a linear type corrosion damage, whereas pitting is more of a point defect type of damage (2-D versus 1-D). In non-sensitized materials, the β phase is less likely to be along GB due to the Mg being dissolved in the α aluminum matrix; thus, IGC resistance is seen. The sensitized material reacts differently due to β phase formation along GB, and since the β phase can be continuous, IGC damage can branch across the attacked surface, along with penetration down GB which are parallel or perpendicular to the corroded surface. Lim et al. have studied the corrosion damage penetration depth based on the surface orientations mentioned previously. The LT surface experienced a parallel type of corrosion damage, while TS and LS surface orientations experienced a significantly higher perpendicular IGC damage. Figure 2-12 demonstrates the effects of exposure time in a corrosive solution on the TS surface IGC damage [75].

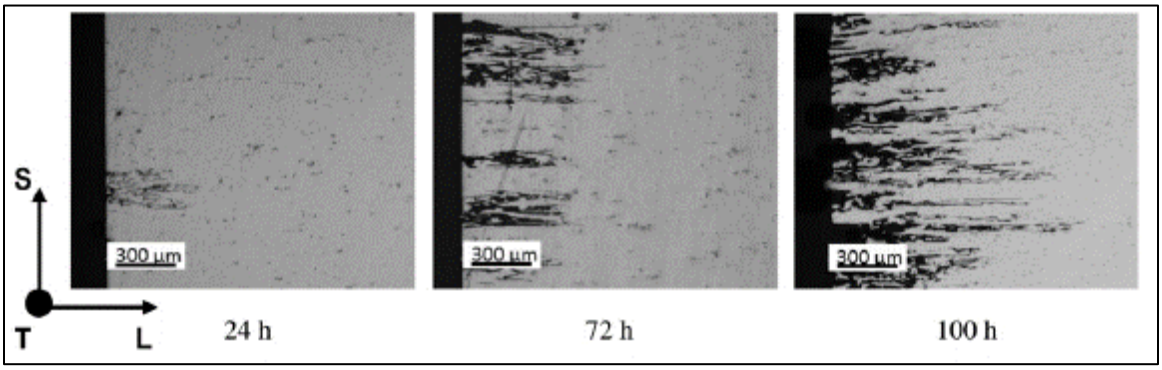

Figure 2-12 TS surface-oriented IGC damage on 5083 for different corrosion times [75]. [Reproduced with permission]

Various studies have tried to identify techniques to negate the IGC damage experienced by 5XXX alloys. Some studies have used a solution heat treatment to create a more equi-axial grain structure allowing the characterization of β phase precipitation and grain sizes during the sensitization process [32], [48], [76]. Thermomechanical treatments have been used post-sensitization to reduce the DoS in hopes of reducing corrosion damage [20]. For non-5XXX alloys, studies have created preferential precipitation of corrosion resistant phases along GB, reducing the effects of IGC damage.

Intergranular corrosion damage can also combine with corrosion byproducts generated from corrosion in aqueous solutions (i.e. seawater) to create exfoliation damage. Grain exfoliation is likely to occur due to the corrosion product buildup on the damage surface, eventually leading to grain pull out when there is more product volume than parent grain [8]. The development of exfoliation damage is surface dependent (like IGC damage). Zhao et al. demonstrated that more exfoliation damage occurred along the L direction on the LT surface orientation for corroded AA 7178 samples than along the T direction [77]. This corroborates Lim's study suggesting again that this grain exfoliation is a result of the surface orientation and β location on grains. Intergranular corrosion damage will be discussed with more relation to 5XXX in Sections 2.4 and 2.5.

2.3.1.4 Environmentally Induced Cracking

Another significant and relevant corrosion damage type is EIC, the combination of tensile stress and corrosion environment [8]. The most prevalent of these EICs is SCC. The three contributing factors toward SCC are a susceptible alloy, critical environment, and tensile stress [8]. For 5XXX series alloys, the components are a highly sensitized exposed surface, an acidic or saltwater solution, and applied tensile stress. Generally, this type of damage is often caused at sea for 5XXX alloys due to cracks forming from the sensitization and the alloy being pulled apart naturally after crack begins. This type of corrosion mechanical damage state is discussed in depth in section 2.6.

2.4 Sensitization-Corrosion Microstructure Relationships

Four areas of interest for sensitization and corrosion damage of 5XXX are β phase and its microstructure, misorientation angle, surface orientation morphology and damage dependence, and the grain size alterations. As mentioned previously, any Al alloy with >3 wt% Mg will undergo the sensitization effect of the β phase preferentially growing on GB. Misorientation angle differences have been proven to lead to dissimilarities in corrosion damage [20], [28]. Another area that requires further study is the relationship of surface orientation to the types of corrosion damage. The last area of discussion is the relationship between 5XXX grain size and corrosion.

2.4.1 β phase (Mg_2Al_3) Sensitization-Corrosion Connection

Many studies have been performed to better characterize the contribution of the anodic β phase to the sensitization-corrosion connection in 5XXX alloys [26], [39], [45], [72], [78], [79]. Bumiller et al. connected the relationship of the β phase continuity and the decrease in breakdown potential

with artificial aging (sensitization) of 5083 aluminum [39]. The E_{br} of AR DoS 6.4 mg/cm² was roughly ~ -0.6 V (Ag/AgCl) while the continuous β phase presence for DoS 68 mg/cm² was more anodic at ~ -0.75 V (Ag/AgCl) [39]. Goswami et al. investigated the continuity of β phase and concluded that β forms continuously for sensitization times > 100 hours at 175ºC, while below this time led to discontinuous β phase and a higher level of applied stress for SCC crack growth rates [78]. Jain et al also performed a study which verified the potential differences between the sensitized 5083-H131 and β phase. Figure 2-13 highlights the effect of DoS increasing and potential changes with the high DoS of 49 mg/cm² having a breakdown potential of -0.68 V_{SCE}, while the β phase (not shown in graph) had a breakdown potential of -0.920 V_{SCE} in a 0.1 M NaCl solution with a pH of 8.3 [72]. Lyndon et al. studied the anodic and cathodic behaviors of bulk Mg_2Al_3 metal via potentiodynamic scans [45]. When varying the pH from 4 to 8, they found that corrosion rates were low, around <5 μA/cm², but if the phase was polarized in this range, then the rates were >100 μA/cm². This study also verified that the β phase was more anodic than the 5083-H131 α matrix, which depended on pH concentration.

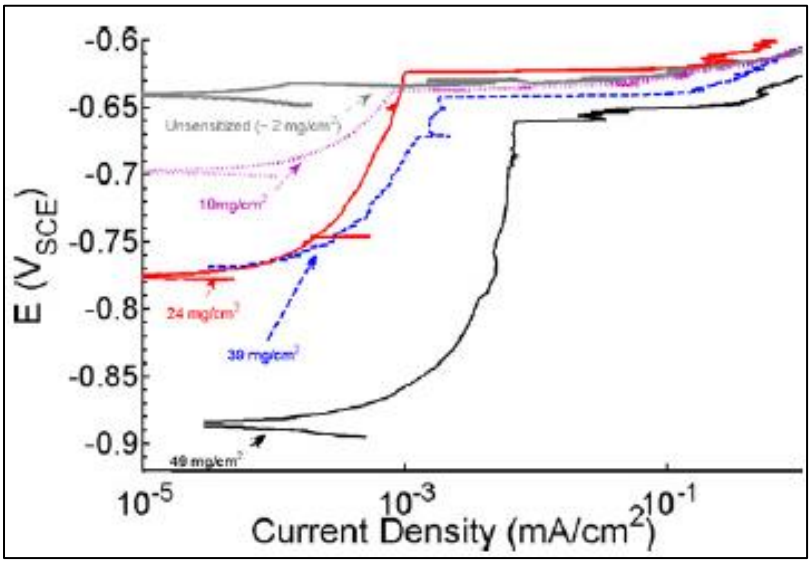

Figure 2-13 Anodic polarization curve of unsensitized and sensitized 5083-H131 in a 0.1 M NaCl solution with a pH 8.3 [72]. [Reproduced with permission]

Gupta et al varied the wt% of Mg in aluminum-magnesium alloys and studied the resulting differences in pitting potential (E_{pit}) and corrosion current (i_{corr}). Any wt% of Mg greater than 3.2% led to the sensitization effect, which caused more anodic potentials compared to the as-quenched and rolled samples [79]. This study concluded that increasing DoS levels correlated with larger

anodic potential differences from the AR state of the alloy. Lim et al. studied AA5083-H131 and related the DoS with the percentage of β phase along GB, along with distinct β phase coverage regions [26]. These regions were high, low, and clean, with high having >70% coverage and low having <70% coverage. The comparison of DoS and the three β phase coverage regimes are illustrated in Figure 2-14. As expected, the AR AA5083-H131 had 100% β free coverage along GB. The high phase coverage on GB increased monotonically with DoS, while the low β phase coverage plateaued at 39 mg/cm². Relationships between these three regions and the DoS demonstrated that with the high β phase coverage, the greatest corrosion damage occurred due to more β phase causing the highest DoS 49 mg/cm² to have a more anodic corrosion potential (E_{corr}) and breakdown potential (E_{br}) [26]. For exposure to NaCl solutions, the amount of high β phase coverage led to the spreading of IGC with the low β phase contributing secondarily to damage.

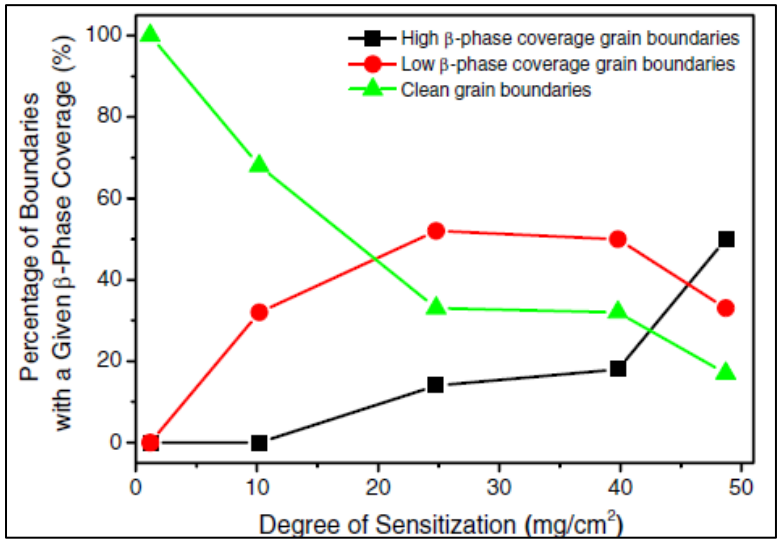

Figure 2-14 β phase coverage relationship with AA5083-H131 DoS [26]. [Reproduced with permission]

2.4.2 Adjacent Grain-Grain and Grain Boundary Plane Misorientation Angles

Another factor impacting the sensitization process is the difference in misorientation angles for different surface orientations [20], [28], [48], [80]–[82]. Davenport et al. investigated the effects of sensitization on AA5182 misorientation angles [28]. Figure 2-15 provides the results of misorientation angles (misorientation of two adjacent grains with the GB planes). The AA5182 samples were sensitized at 150ºC for 10 hours (giving a 40 mg/cm² DoS), and electron backscattered diffraction (EBSD) patterns were used to obtain crystallographic grain orientation

data. It was found that when misorientation angles of the grains to the GB were <20º, that corrosion resistance was present due to lack of β precipitation. At misorientation angles >20º, continuous, discontinuous, and clean GB were present along with corrosion susceptibility [28]. No correlations could be made between the type of precipitation and misorientation angle from that study.

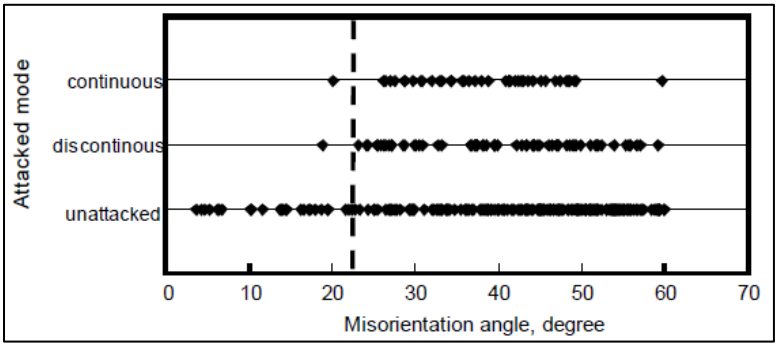

Figure 2-15 GB misorientation angle in AA5182 with DoS of 40 mg/cm² plotted based on corrosion attack type [28]. [Reproduced with permission]

Yan et al. studied effects of grain boundary misorientation angles and the relationship to corrosion resistance (from nitric acid) on an Al-Mg alloy with Al-5.3wt% Mg. In this study, Yan found that having low angle GB (LAGBs) (<15°) led to better immunity to β precipitation and corrosion attack. However, at high-angle GB (HAGBs) (>15°), the alloy was vulnerable to β precipitation and grain boundary acid attack. This study supports Davenport's study and further verifies the influence of misorientation angle, grain plane orientations of adjacent grains, and the presence of coincident site lattice boundaries [48]. Figure 2-16 illustrates this correlation in the form of scanning electron microscope (SEM) images of a sensitized Al-Mg alloy before and after phosphoric acid etching, along with a plot showing results of % LAGBs and % HAGBs. Scotto D'Antuono et al. continued investigating the effects of misorientation angle on β phase grain boundary coverage [80]. This study demonstrated that nucleation beading occurs at angles <3º due to dislocations, but it was limited due to grain boundary energy. For high-angle misorientation angles ranging from 15º to 40º, the precipitates were not impeded by GB and could experience uninhibited growth between grains [80].

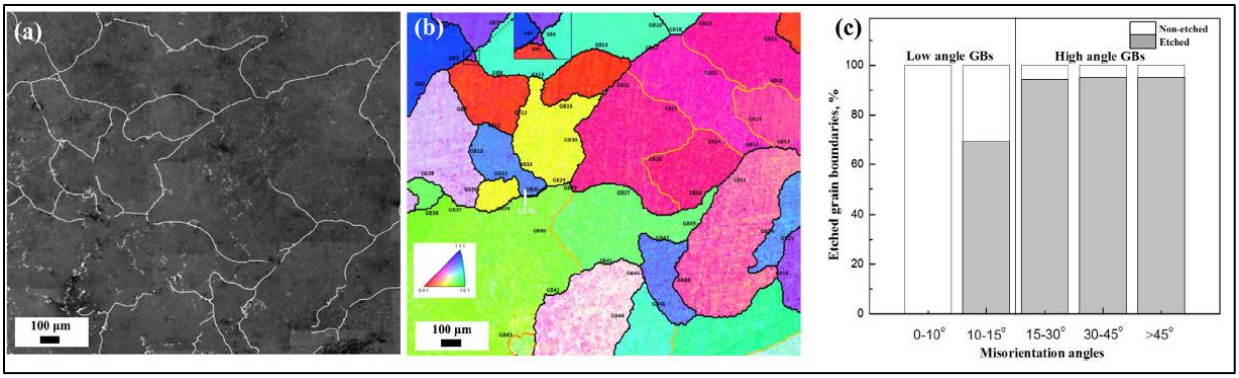

Figure 2-16 (a) A sensitized AR Al-Mg alloy after phosphoric acid etching, (b) EBSD grain orientation map, and (c) graph of misorientation angles after etching [48]. [Reproduced with permission] https://creativecommons.org/licenses/by/4.0/

Tan et al. (2010) investigated the differences in AR and TMT AA5083 alloy [20]. The goal of this study was to prove that TMT of AR AA5083 would reduce the amount of β phase precipitation and, thus, reduce corrosion damage from sensitization. The AR AA5083 had a higher fraction LAGBs, which allows for natural corrosion resistance. The TMT samples were exposed to 500°C for 30 minutes, causing a higher proportion of high misorientation angles (>15º), which was counteracted by a more equi-axial grain structure, which lowered DoS by deterring continuous β morphology along GB due to recrystallization [20].

Zhao et al. best described the grain boundary related β phase coverage through explaining the degrees of freedom of GB for AA 5456 [81]. Three degrees define the grain boundary misorientation angle (three directions in which the grains oriented from each other) and the two remaining degrees are the grain boundary plane orientation. Zhao also found that for AA 5456, that the grain boundary plane orientations near {110} will facilitate β phase precipitation as well as lead to differences in β phase thickness on GB. Zhang et al. compared different processing techniques and their effects on grain orientation, grain size, and grain boundary orientation [82]. Low angles are <5º, medium angles are 5º to 15º, and high angles are >15º. This study demonstrated that cryo-rolling and equal channel angular pressing (ECAP) led to higher fractions of LAGBs and lower fractions of HAGBs. The overall objective was to determine which techniques reduce HAGBs, and which allow for the uninhibited growth of thick β phase along GBs (heavy sensitization).

2.4.3 Surface Orientation Dependent Damage

Various studies have shown the effects of surface orientation with relation to the combined damage state of sensitization and corrosion on 5083 alloys. To recap, the three primary surfaces are LT, LS, and TS; LT is the rolling direction and the LS and TS are the through thickness of plate materials. Zhu investigated the effects of nitric acid attack on sensitized 5083 and 5456 alloys and found that the TS and LS surfaces experienced more detrimental exfoliation damage due to the presence of continuous β phase along the GB [83]. Figure 2-17 illustrates the IGC damage on the LT, TS, and LS surfaces of 5083-H131 with a DoS of ~43 mg/cm². The IGC spreading damage propagates parallel to the exposed LT surface and the attacks perpendicular to the LS and TS surfaces. Note that the corrosion damage is deeper on the LS and TS surfaces.

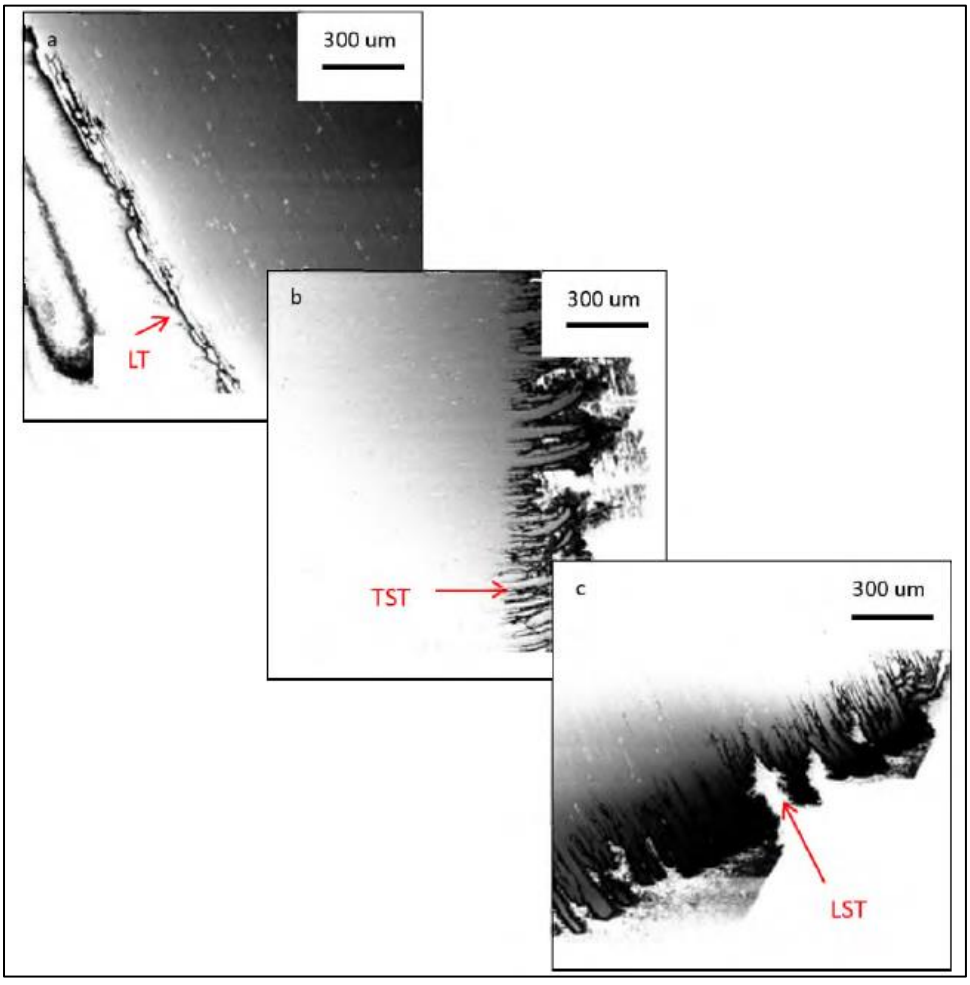

Figure 2-17 Surface orientation corrosion damage on LT, TS, and LS surfaces of sensitized AA5083-H131 [83]. [Reproduced with permission]

Lim et al. have performed three studies related to the surface-oriented IGC damage for sensitized 5083-H131 [3], [25], [26]. Figure 2-13 highlights the same perpendicular L direction IGC damage for the exposed TS surface. Lim also found that the IGC damage was most severe in the L direction, high for T direction, and lowest for S direction. The damage in the L and T directions corresponded to exposed TS and LS surfaces, with the minimum damage of the S direction relating to the exposed LT surface for sensitized 5083-H131. Lim et al. also found that the IGC damage will propagate without a continuous path of β precipitates along GB [3]. Figure 2-18 illustrates the effects of surface orientation and DoS with respect to charge density and damage depth for each of the primary directions L, T, and S for sensitized AA5083-H131. Figure 2-18 (a) indicates the higher anodic charge density along the L direction, which is related to a higher presence of the anodic β phase. The L and T directions had greater damage depths as well due to the higher manifestation of β precipitates on the GB of the through thickness LS and TS surface orientations as illustrated in Figure 2-18 (b).

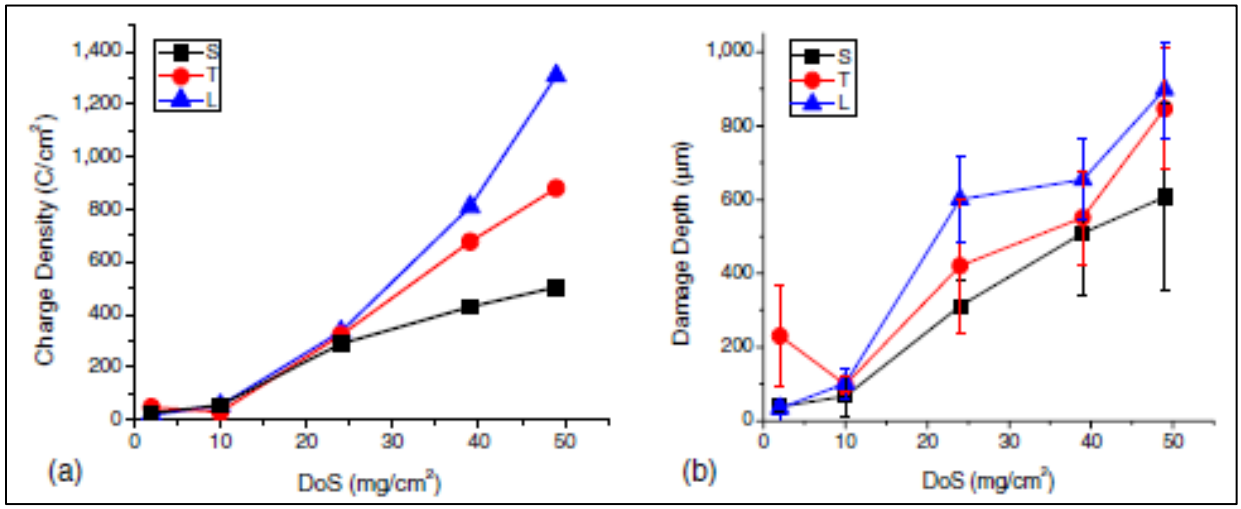

Figure 2-18 100 hour corrosion at -0.73 V_{SCE} in 0.6 M NaCl at pH 8.3 of sensitized AA5083-H131 (a) charge density and (b) damage depth [3], [25]. [Reproduced with permission]

Lim et al. began to create models of IGC damage based on the surface orientation related corrosion damage [75]. Figure 2-19 provides the LS surface (top) and LT surface (bottom) as the IGC propagates over time for 20, 80, and 100 hours for AA5083-H131 at DoS of 49 mg/cm². One correlation for this IGC damage model is that at 100 hours simulated corrosion, simulated damage is slightly worse for the L direction (top row) than the S direction (bottom row), which matches the experimental data [26].

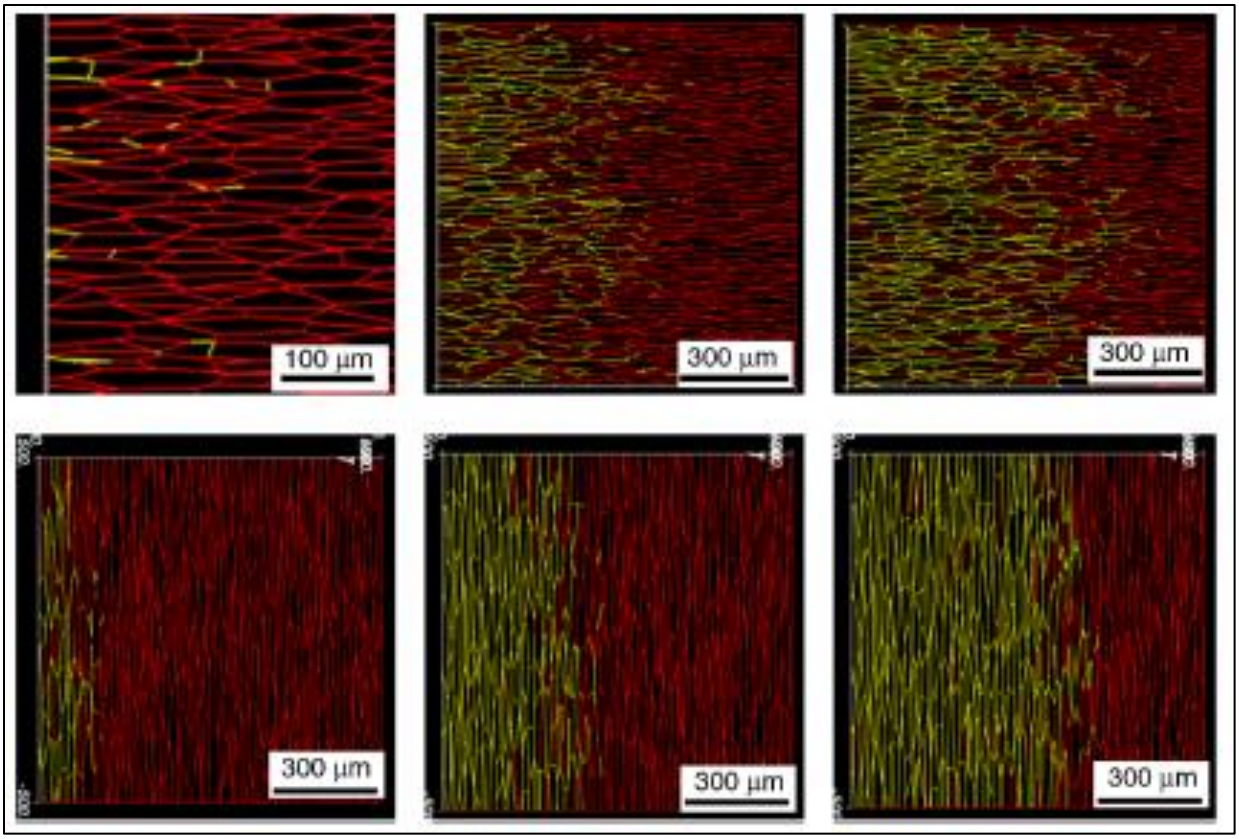

Figure 2-19 Simulation IGC damage of sensitized AA5083-H131 exposed LS (top) and LT (bottom), increasing time left to right [75]. [Reproduced with permission]

Other studies help highlight the reason why the LS or TS surface orientations have a more unique corrosion reaction that initially realized. A study by Mills et al. demonstrated the effects of corrosion damage on the exposed surface orientation of 5083-H116 sensitized at 150°C. However, due to a lack of recrystallization or homogenization prior to sensitization, the presence of cold-rolling was noticeable in the corrosion damage morphology when comparing LT and LS surfaces after exposure to accelerated corrosion environments. The LT surface had uniform exfoliation damage as expected, while the LS surface orientation had a corrosion susceptible-resistant-susceptible (C-SRS) microstructure [84]. Wei et al. specifically studied the LS microstructure of the heterogeneous AA5083 alloy [47]. This study found that after 40 years of natural sensitization and no exposure to a recrystallization or homogenization environment, the same LS (through plate thickness) C-SRS microstructure was also present. Based on Wei's study, it was determined that recrystallization occurred in the susceptible regions, which caused smaller grains and larger grain boundary volume fractions, both of which led to more preferential β precipitation. In the corrosion resistant region of the plate, the grains were coarser, which helped to reduce the number of β

precipitation sites. The corrosion susceptible regions of the plate had a DoS of ~36 mg/cm², while the more corrosion resistant region of the LS C-SRS structure had a DoS of ~28 mg/cm² [47]. Figure 2-20 contains SEM images taken of the C-SRS structure after exposure of the 5083 alloy to nitric acid; the corrosion resistant region is the two middle images and the corrosion susceptible regions are the left and right images.

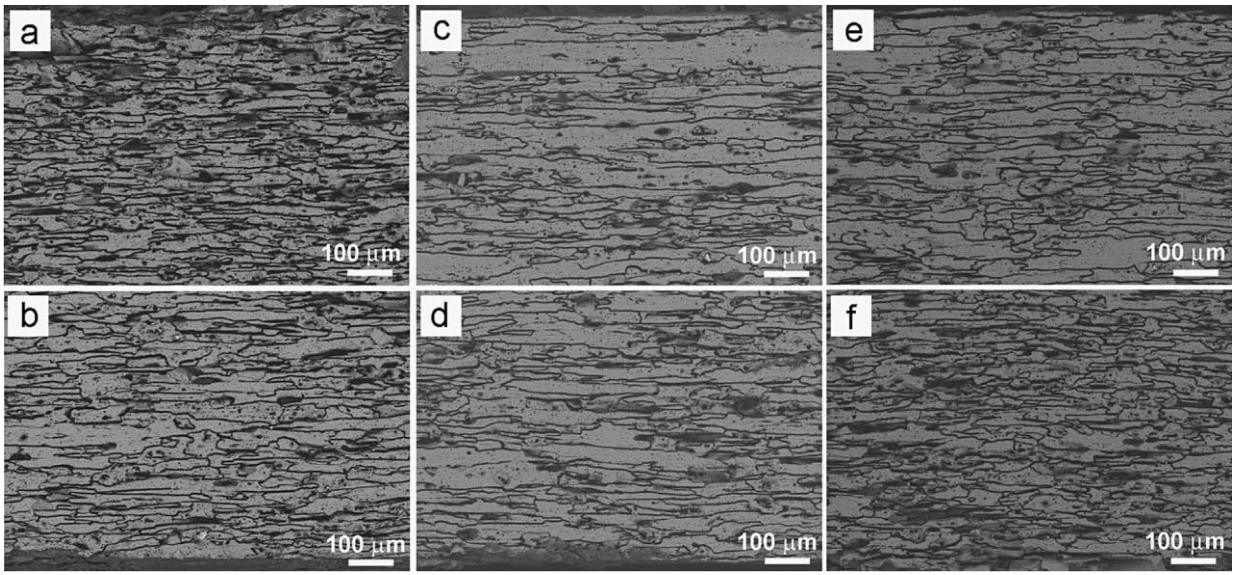

Figure 2-20 SEM images from NAMLT results of naturally sensitized 5083-H116 with (a), (b), (e), and (f) being the corrosion susceptible sections (outside of the C-SRS microstructure) and (c) and (d) being the corrosion resistant section (middle of the C-SRS microstructure) [47]. [Reproduced with permission]

2.4.4 Grain Size

The last remaining contributor to the corrosion damage experienced by sensitized 5083 alloys is a change in grain size. Oguocha et al. investigated the effects of sensitization temperature with the mechanical properties of AA5083-H116 [49]. Figure 2-21 contains images taken in bright field (BF) of 5083-H116 sensitized at 168 hours from the AR state and 100ºC, 150ºC, 175ºC, and 200ºC temperatures. It should be noted that the grain sizes change with sensitization temperature for the same amount of sensitization exposure time. Oguocha et al. also demonstrated that the grain size decreases with an increase in sensitization time for the 175ºC temperature [49].

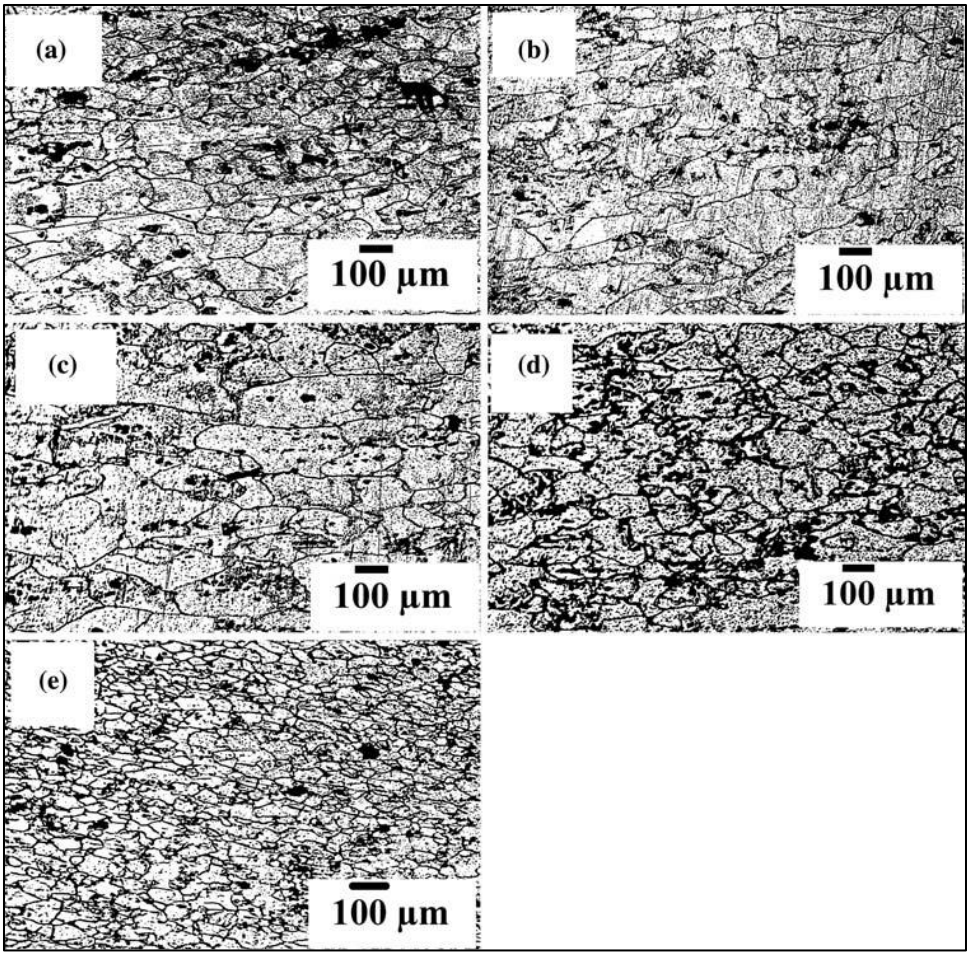

Figure 2-21 AA5083 sensitized for 168 hours at various temperatures including (a) AR, (b) 100ºC, (c) 150ºC, d. 175ºC, and 200ºC [49]. [Reproduced with permission]

Li investigated some mechanical property changes of AR 5083-H116 and sensitized 5456-H116 alloys [59]. Sensitized 5083-H116 was not studied; however, for 5456, AR and sensitized grain sizes were reported. Decreases in grain sizes on all three surfaces (LT, LS, and TS) were observed, with the sensitized grain size on the LS plane and in the L direction being nearly half of the unsensitized 5456-H116 grain size. Aspect ratios decreased for each surface, with the LS surface having the largest aspect ratio drop from 2.7 to 2.1 [59]. Tan et al. showed the effects of TMT on DoS; however, they did not discuss grain size contribution [20]. Zhang et al. performed a study relating effects on changes in grain size with changes in sensitization of AA5083 [82]. For sensitized AA5083, the cryo-rolling process reduced the grain size the most as illustrated in Figure 2-22 (a), due to a reduction in fraction of HAGB. Other mechanical processing techniques such as ECAP and high-pressure torsion increased the DoS from the AR AA5083 state. Due to the rolling

process of AA5083 alloys, some studies use a solution heat treatment to recrystallize the grain structure prior to any sensitization and corrosion experiment [3], [5], [7], [20].

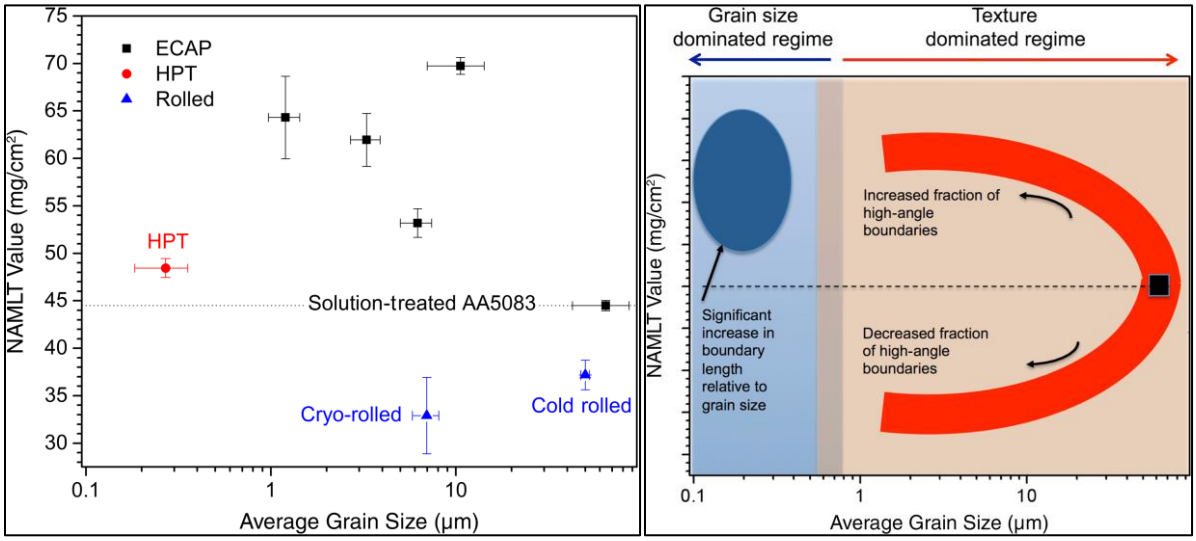

Figure 2-22 (a) Mechanical processing effects on grain sizes and DoS of AA5083 and (b) phenomenological representation of grain size vs. DoS in 5XXX [82]. [Reproduced with permission]

Zhang et al. better described the relationships of the grain size and grain orientations with a phenomenological figure based on experimentally obtained results [82]. These are provided in Figure 2-23 (b), with emphasis on submicron to micron relationships to NAMLT/DoS values. When submicron grain sizes are reached, then the grain size contribution to DoS will surpass the grain to grain orientation angle differences. Further separation between grain size and grain to grain orientation DoS dependence is needed to determine which are the controlling factors for corrosion damage. Moldovan et al. studied AA 5083-H321 to find that annealing the alloy at 250ºC to 260°C for one hour led to a "homogeneous" microstructure. This study also found that slow cooling reduced the amount of discontinuous β phase along GB.

2.5 Mechanical Properties

Along with the effects of sensitization and corrosion damage, the importance of mechanical properties (before and after these damage states) requires investigation. Important properties for sensitization and corrosion damaged materials are hardness (H), yield strength (σ_y), and ultimate tensile strength (σ_u). Creep, fatigue, and fracture properties also require investigation for a full picture of the 5XXX mechanical performance. These mechanical properties are briefly explained

in terms of microstructure-mechanical property relationships, followed by effects of sensitization, corrosion, and the combined sensitization-corrosion damage on 5083.

2.5.1 Annealing Process

Mechanical properties of 5083 alloys are generally related to the grain structure present, which can depend on the level of recovery, recrystallization, or grain growth that occurs from annealing prior to testing or any heat sources prior to or during testing. These three different phenomena are temperature dependent and based on the Al-Mg phase diagram; they change the grain size and precipitate distribution of the alloy. A brief explanation of recovery, recrystallization, and grain growth follows.

The recovery stage entails annealing out point defects, annihilation and dislocation rearrangement into lower-energy configurations, subgrain formation and growth (polygonization), and recrystallization nuclei formation [85]. It is significant that the effects of cold-rolling are still in place after recovery, meaning the elongated granular structure still exists. Recrystallization is the nucleation and growth of new grains due to migrations of HAGB. Distinct primary and secondary types are noticeable for recrystallization. Primary recrystallization is when the strain-free new grains begin to nucleate, while secondary recrystallization begins with the growth of these nuclei [86]. Grain growth is the last step of the annealing process. Smaller grains are consumed due to large grain growth to reduce grain boundary free energy [86]. A schematic for recovery, recrystallization, and grain growth is provided in Figure 2-23.

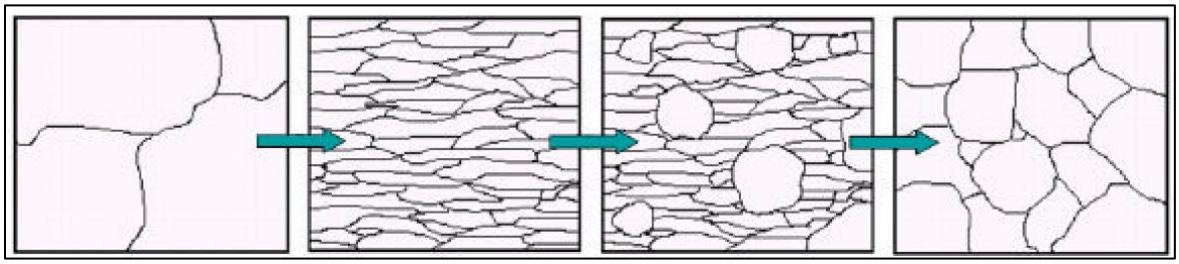

Figure 2-23 Diagram of recovery, first and second recrystallization, and grain growth [86]. [Permission not required]

The sensitization process can lead to recovery and recrystallization in 5083 alloys and, thus, the grain size correlation to mechanical properties is potentially significant [49], [87]. The ductile aluminum stress-strain relationship can give insight to Young's modulus (E), σ_y, σ_u, and fracture strain (ε_f) of the alloy. Figure 2-24 highlights the effects of elevated temperature prior to

mechanical testing on these properties for 5083-H116. Exposures beyond 200ºC led to noticeable drops in σ_y and σ_u and increases in ε_f. These changes in mechanical properties can be attributed to α grain size changes and magnesium depletion from α to form β precipitation. Another study by Chen et al. found similar results for annealing time and temperature degradation of 5083-H116 mechanical properties [34].

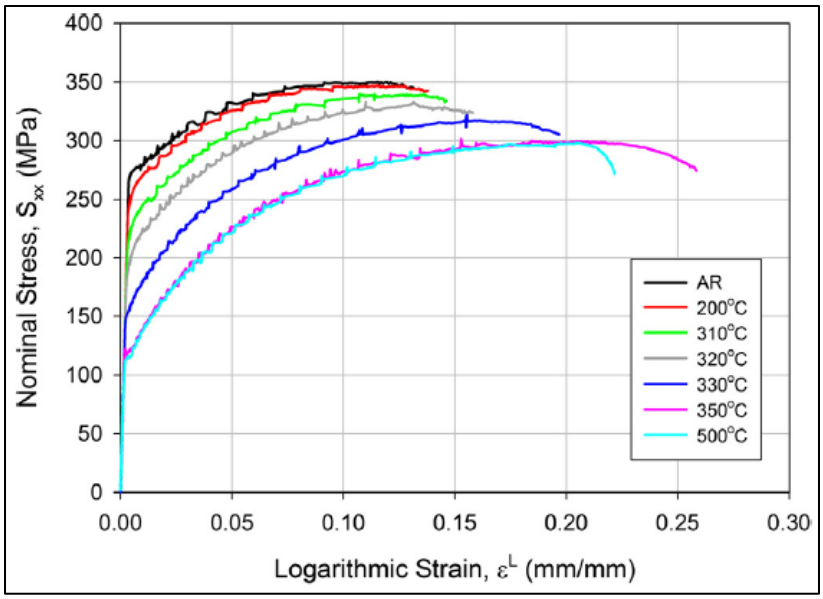

Figure 2-24 Stress-strain curve of AR 5083-H116 with post-fire heating temperatures ranging from 200°C to 500°C [63]. [Reproduced with permission]

2.5.2 Homogenization with DoS and/or Corrosion 5XXX Mechanical Properties

Various studies were performed investigating the interacting effects of recrystallization, sensitization, and corrosion damage on mechanical properties of 5XXX alloys. Davenport et al. performed an IGC and SCC study on sensitized 5182 aluminum [28]. Results showed that the ε_f from slow strain rate testing (SSRT) in air and 3.5% NaCl at pH 3 differed. In air, the sensitized material at 70ºC and 150ºC had a similar ε_f. However, for the 150°C heavily sensitized material (greater than 30 mg/cm²), the ε_f dropped nearly four times in magnitude from 0.45 to 0.1 when tested in a 3.5% NaCl solution with pH 3 [28]. Jones et al. performed another study on the relationship of sensitization level to the effects on crack length (a) for SCC environments [7]. Figure 2-25 summarizes the results of increasing the exposure time of AA5083 at a sensitization temperature of 175ºC. One of the main conclusions from this study is that higher DoS or more β

phase precipitation led to an increase in fatigue crack-growth rates by more than five times after 100 hours of 175ºC sensitization [7].

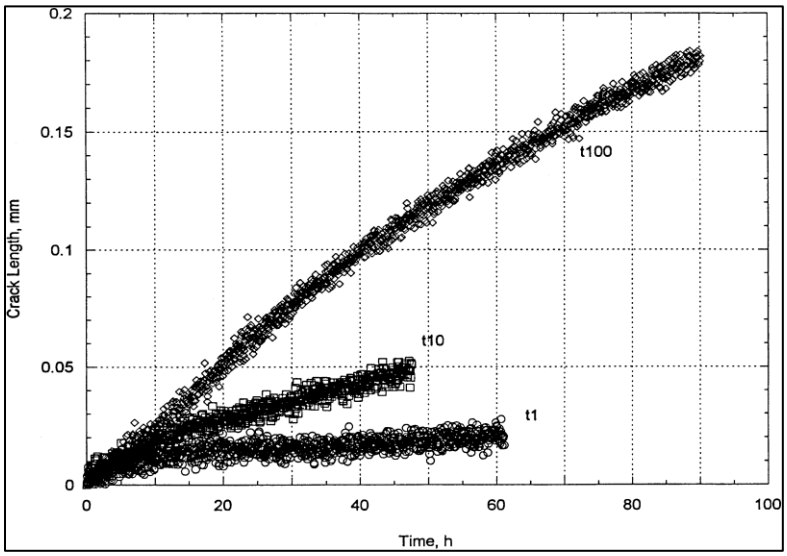

Figure 2-25 Crack growth of AR 5083 sensitized at 175°C for 1, 10, and [7]. [Reproduced with permission]

Kciuk et al. performed a study in which an Al-Mg-Si alloy was quenched at different temperatures for 3 hours and then exposed to 160°C from 3 hours to 24 hours [29]. At 12 hours of exposure to the sensitization temperature of 160°C, the crack resistance was higher than lower sensitization times. However, after an additional 12 hours of exposure, the crack resistance decreased again. Kciuk et al. also investigated the effects of these annealing temperatures on the Al-Mg-Si alloy prior to sensitization and the relationship to tensile strength and hardness. After 12 hours of sensitization at 160°C, the alloy hardened and had higher tensile strength; however, an extra 12 hours at 160°C led to a decrease in hardness and tensile strength close to the as annealed state of the material [33]. Singh et al. investigated the effects of quenching at 510°C for two hours prior to cryo-rolling and annealing the 5083 alloy. The cryo-rolling process improved the alloy's yield strength and ultimate tensile strength and reduced the impact toughness [31].

Zhang et al. investigated reversing the DoS with a reversion heat treatment and related that to the hardness of the AA 5083 that naturally sensitized for 40 years [32]. The field-retrieved material had a lower DoS after reversion temperatures ranging from 150°C to 240°C after four hours of exposure. The reversion temperature of 240°C helped dissolve the magnesium back into the solid

solution α grains and short exposures of one hour at 180°C and 220°C helped maintain the 5083 hardness. Longer reversion times reduced the hardness of the 5083 material.

2.5.3 Non-RX with DoS and/or Corrosion 5XXX Mechanical Properties

Other studies focused on non-RX 5XXX aluminum and its relationship to sensitization with and without corrosion damage and the relationship to mechanical properties. Chang et al. investigated the effects of sensitization, superplastic forming, and annealing on the SCC of 5083 [52]. This study revealed that superplastic forming and sensitization (without annealing) led to a decrease in σ_u, σ_y, and percent elongation. Post annealing of the sensitized material at 345°C for one hour restored the σ_u, σ_y, and elongation properties to close to the AR 5083 [52].

Adigun and Oguocha investigated the hardness, yield strengths, and ultimate tensile strengths of sensitized, non-corroded AA5083-H116 [49], [87]. The grain size decreased with increasing time and increased sensitization temperature. Figure 2-26 contains Adigun and Oguocha's verification of the association between grain size and Vickers Hardness (H_V). The AR AA5083 had the highest hardness of 97 H_V, while the 100°C and 150°C decreased to roughly 90 H_V [49]. The 175°C and 200°C saw more severe changes in hardness with increasing sensitization time. One of the main reasons that the H_V changes are noticeable is due to the change in grain size from sensitization as reported by Oguocha et al. (the grain sizes values were not reported). Oguocha et al. partly attributed the hardness property degradation to a reduction in dislocation density during recrystallization of the AR material [49].

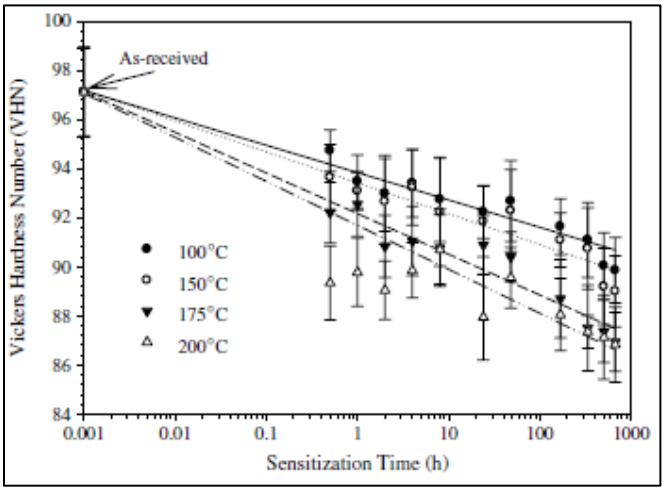

Figure 2-26 The sensitization and hardness relationship of 5083-H116 [49], [87]. [Reproduced with permission]

Oguocha et al. further investigated the relationship between sensitization time with σ_u and σ_y, which is provided in Figure 2-27. As expected, the higher sensitization temperatures of 100°C to 200°C led to a decrease in σ_u and σ_y. For this temperature range, little change in σ_{ts} occurred until >200 hours of sensitization time and then the σ_y dropped by about 10 MPa after the maximum sensitization time. At 150°C sensitization temperature, the σ_u dropped more drastically starting at 200 hours of sensitization time, while σ_y degradation occurred more noticeably after 100 hours. For σ_u, both the 175°C and 200°C sensitized samples decreased after 10 hours, with the 200°C sample dropping the most by 20 MPa after the maximum studied sensitization time. The σ_y for both 175°C and 200°C sensitized 5083-H116 dropped prominently after one hour, with nearly a 50 MPa loss after the maximum time. Oguocha et al. attributed the degradation of σ_u and σ_y of 5083-H116 sensitized at 175°C and 200°C to the recrystallized structure, along with precipitation Mg-rich β phase and the decrease in solute Mg atoms in the solid solution α matrix [49].

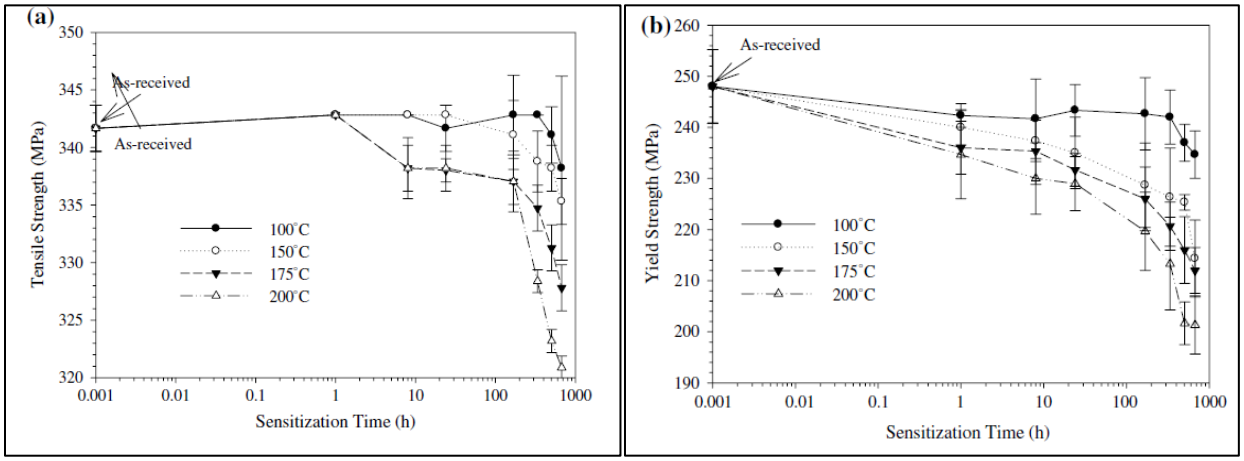

Figure 2-27 Sensitized 5083-H116 (a) ultimate tensile strength and (b) yield strength of 5083-H116 [49], [87]. [Reproduced with permission]

Li et al. investigated the effects of sensitization on non-RX 5456-H116 and the relationship to hardness, fracture toughness (K_{IC}), and fatigue crack-growth rate (da/DN) [59]. The AR 5456 had roughly a Rockwell B hardness (HRB) 15 higher than the sensitized 5456 alloy. It was found that sensitization also reduced the K_{IC} value obtained in fracture toughness testing. The directional dependence on fatigue crack-growth rate was demonstrated, with the longitudinal (rolling) direction causing greater loss in quality of stress intensity factor (ΔK_{th}) than the transverse direction [59]. Kramer, et al. found that sensitized 5454 could be reversed if an exposed to 240°C

to 280°C for 10 minutes and that this reversion temperature treatment did not lower the yield strength of the material [43].

Various studies have been conducted on sensitized and corroded AA5083 alloys. Searles et al. performed Constant-Extension-Rate Testing (CERT) on non-homogenized and sensitized AA5083 in air, humid air, 3.5% NaCl at open circuit potential (OCP), and 3.5% NaCl at -0.980 V_{SCE} (β breakdown potential) [5]. Searles et al. found that up to a sensitization time of 333 hours at 150ºC, the σ_y, σ_u, and ε_f did not change with sensitization for mechanical testing in air. When testing in 3.5% NaCl at OCP, the ε_f values decreased with increasing DoS until a continuous β phase morphology was present on the GB [5]. It was also found that using the breakdown potential of -0.980 VSCE of β in the CERT led to a restoration in the stress-strain data due to polarization, when compared to the AR material.

Pao et al. and Goswami et al. performed SCC studies on the effects of sensitization on crack length [60], [78]. Pao et al. showed that crack-growth rates increased and K_{th} decreased when DoS increased. It was found that a threshold of discontinuous β < 240 hours for 175ºC sensitization and continuous β at >240 hours at 175ºC led to maximum crack-growth rates and a minimum ΔK_{th} [60]. Goswami continued this study and provided more insight with surface dependent damage of the LS surface. 5083 was sensitized for 240 hours at 175ºC and the crack length increased 300% versus the AR 5083 initial crack length (a_i). It was found once again that the crack length increased and a lower ΔK_{th} was present with increasing DoS [78]. Holtz continued the work of Pao and Goswami by adding the effects of sensitization temperatures of 70ºC and 100ºC to in 1% NaCl [57]. The sensitization of 100ºC and 175ºC had similar effects on the ΔK_{th} versus aging time. However, at 70ºC, the ΔK_{th} stabilized at a higher value even after 10000 hours of sensitization exposure. Holtz also found that all sensitization temperatures had the same linear decrease in ΔK_{th} starting at 30 mg/cm² [57]. Holroyd and Seifi studied environmentally EIC. Holroyd found two types of cracking, one in the form of IGC damage with no pre-exposure to saline solution and the second by enhancement of exposure to saline solution. This saline driven cracking required high K values and had greater velocities than the solely sensitized cracking [56]. Seifi performed similar studies, but also performed SSRT studies, which proved that the reduction in mechanical properties was influences by sensitization and the presence of saline solution and humidity [62].

Bovard and Cormack performed similar studies on 5XXX alloys. Bovard found that a DoS greater than 44 mg/cm² will drastically increase the crack length compared to the AR 5XXX alloy. Bovard also found that crack-growth velocity will increase more drastically with the DoS of 44 mg/cm² [50]. Cormack added to the knowledge of crack-growth length of sensitization on 5456 [88]. At a DoS of 30 mg/cm², the crack growth nearly doubled from the as-received crack length after 550 hours of sensitization, with the DoS of >62 mg/cm² nearly tripling the crack length from the AR state. Cormack's comparison of the crack-growth velocity, however, demonstrated that even >30 mg/cm² increased the crack-growth rate of 5456-H116 [88].

3 Research Overview

3.1 Gaps

Various areas of the sensitization and corrosion damage of 5083 alloys have been studied for better understanding of naval vessel ship alloy degradation. The first area requiring further investigation is the accelerated aging of 5083-H116 with regard to sensitization, corrosion, microstructure and mechanical properties. Secondly, the impact of the elongated grain structure on the corrosion of aluminum alloys requires further study. Lastly, techniques for predicting the residual mechanical properties of aluminum alloys after sensitization and corrosion damage have yet to be fully developed.

3.1.1 Accelerated Artificial Aging Temperature Dependence

Some sensitization studies have been performed on recrystallized or solution heat treated 5083 alloys to investigate microstructure alterations, corrosion damage, and residual mechanical properties. Other studies focused on similar properties with relation to non-solution heat treated 5083 alloys. For 5083 alloys, the 4.5 wt% Mg concentration leads to the nucleation and growth of β phase along GB due to the solubility limits of Mg below 200ºC when exposed to sensitization [25]. Previous studies have utilized different sensitization temperatures ranging from 40°C to 200°C demonstrating that a β morphology along the GB depends on the time and temperature of the exposed aluminum and is based upon β diffusion and kinetics [3], [6], [7], [65]. Oguocha et al. studied 5083–H116 with relation to sensitization temperature and uniaxial tensile testing, concluding that α grain sizes decrease with increasing sensitization time at 175°C, which suggests partial recrystallization [49]. Li also confirmed that sensitization leads to a decrease in α grain size for 5456 alloys, regardless of surface orientation with respect to the rolling direction [59].

Despite this progress, there are numerous aspects related to the temperature-time dependent sensitization of 5083 alloys that require further investigation. For sensitization temperatures below 175°C, a systematic study of α grain size changes has not been conducted. This is of practical importance because the US Navy currently uses 150°C for accelerated sensitization and corrosion studies. Previous research by Zhang et al. has shown that the β for materials sensitized at 100°C and 150°C is different, even for an equivalent DoS [65]. It is expected that α grain size changes will be different at the two sensitization temperatures based on Oguocha's research [49]. Also,

since sensitization is a temperature-time dependent process, an investigation on α grain size alteration with respect to long-term exposure at 100°C versus short term exposure at 150°C would be beneficial to better understand and utilize higher temperatures for artificial aging purposes.

To achieve this research objective, several steps were completed. The first step was to sensitize Alcoa 5083-H116 at 100°C and 150°C for up to 1500 hours to generate DoS ranging across the entire sensitization spectrum from being corrosion resistant to highly corrosion susceptible. The next step was to select samples from the two sensitization temperatures at different times, along with samples that have the same DoS. The grain sizes for these samples was analyzed for at least two surface orientations, preferably the LT and LS surfaces, with the goal of identifying partial recrystallization that may have taken place. Room temperature uniaxial tension tests were performed on purely sensitized samples of the same sensitization level with the goal of discerning α and β alteration influences on yield strengths. From mechanical testing of 100ºC material, the expectation is to only see recovery through slight degradation in yield strengths even at the longest sensitization times. For 150ºC sensitized material, larger drops in yield strengths and reduction in grain size indicate the end of the recovery mechanism and onset/extent of partial recrystallization. With data gathered from the mechanical testing and grain size analysis, conclusions can be made with respect to which sensitization temperature and time combinations are more detrimental.

3.1.2 Effect of Textured/Sandwiched Grain Structure

The effects of the rolling process will be present if no solution heat treatment occurs prior to the sensitization of 5083 alloys. With no recrystallization, the rolled surface, also known as the longitudinal transverse (LT) surface orientation, will have a slightly less equiaxed grain structure compared to the elongated surface's longitudinal short transverse and long transverse (LS) and short transverse (TS) surface orientations [3], [25], [63]. Along with differences in granular microstructure dependent on surface orientation, β morphology and distribution along the GB and α grain shape/size will be dependent on the surface orientation [[3], [7], [82], [84]. These factors will all contribute to the extent and depth of the corrosion damage when exposed to accelerated corrosive environments. The LT surface will experience an IGC/exfoliation damage combination sequence, with both damages progressing parallel with the LT surface orientation. The LS and TS surfaces are both through thickness surface orientations of the plate material, which experience an

alternative IGC/exfoliation damage sequence, with the IGC damage progressing perpendicular to the surface orientation [3], [84].

One phenomenon that requires methodical investigation is the presence of a corrosion susceptible-resistant-susceptible (C-SRS) microstructure along the LS and TS surface orientations [47], [84]. One area studied further is the critical DoS in which the C-SRS sandwich structure appears, with an expectation of the C-SRS structure appearing above 25 mg/cm². Another area of examination is the relationship of misorientation angles between grains and how this creates C-SRS structure during etching or corrosion damage. If the misorientation angles are <20º between grains, then the alloy will have corrosion resistance, and if the misorientation angles are >20º, some form of β precipitation (continuous or discontinuous) will contribute to IGC attack on the sandwich structure [28]. The percentage of β phase along the GB of the C-SRS and in transition areas between these regions have yet to be shown [28], [47].

To assist in these goals, three tasks have been completed to further confirm this sandwich structure. The first task was to measure the grain structure of Alcoa 5083-H116 for sensitization levels at both 100ºC and 150ºC, with emphasis on grain size differences on the LS surface orientation, with expected differences between susceptible and resistant regions. The second task was to take selected etched samples and obtain orientation image maps (OIM) from the SEM to measure the misorientation angles of the corrosion susceptible and corrosion resistant regions of the LT microstructure [48]. Prior literature suggests that the difference in misorientation angles of the grains leads to the influx of β along GB, thus, creating this C-SRS damage regime [5], [28], [47], [48], [65].

3.1.3 Methods for Predicting Residual Properties following Sensitization and Corrosion

Various aspects of sensitized 5083 and mechanical properties have been studied by other research groups. Some studies were performed without the presence of corrosion damage. Chang et al. investigated the effects of sensitization, superplastic formation, and annealing on the SCC of 5083 concluding that superplastic formation and sensitization (without annealing) led to a decrease in ultimate tensile strength (σ_U), 0.2% offset yield strength (σ_Y), and percent elongation [19]. Oguocha studied the effects of sensitization temperature with respect to σ_Y, σ_U, and HV and noted that partial recrystallization occurred for 5083 sensitized at 175°C and 200°C; Mg-rich β phase

precipitation and a decrease in solute Mg atoms in solid solution all led to the reduction of yield strength and tensile strengths [14]. Li et al. showed the mechanical properties of naturally sensitized 5083 and 5456 alloys, with fracture toughness (K_{IC}) and hardness decreasing with increasing sensitization levels. The fatigue crack-growth rate was dependent on surface orientation with the LT having greater loss in quality of stress intensity factor (ΔK_{th}) than the transverse direction [15].

Other studies have been performed on 5083 alloys that were sensitized prior to and corroded during mechanical testing. Searles performed CERT in air and in 3.5% NaCl at OCP, finding that σ_Y, σ_U, and failure strain (ε_f) did not change after sensitization up to 333 hours at 150°C and that ε_f decreased in the corrosive solution once continuous β morphology from sensitization was present [5]. Davenport performed slow strain rate (SSRT) of sensitized 5182 aluminum in air and 3.5% NaCl, demonstrating a drop in failure strain by a magnitude of four times of heavily sensitized aluminum at 150°C [18]. Jones found another correlation to the effect of highly sensitized 5083 aluminum at 175ºC for 100 hours, which increased fatigue crack-growth rates by five times [6]. Pao Goswami, and Holtz performed more studies on crack length and crack-growth rates with sensitization levels with continuous β leading to maximum crack-growth rates and minimum ΔK_{th} [20-22]. Bovard and Cormack demonstrated that the crack-growth velocity increased for a corrosion susceptible sensitization level of 33 mg/cm² and heavy sensitization value of 44 mg/cm² [23, 24].

Most of these studies were conducted on sensitized 5083 and are the result of tensile testing, sensitized and corroded samples exposed to CERT or SCC tests, or sensitized and corroded LS crack-growth experiments [6, 14, 20-22]. However, areas such as surface orientation dependent corrosion damage of sensitized AA5083-H116 tensile and creep properties have not previously been studied. Sensitization and corrosion of AA5083-H116 can occur on ships at temperatures ranging from room temperature to temperatures up to 500ºC. After the damage is present, the mechanical properties should be investigated to assess the effectiveness of the weakened alloys. Models for residual mechanical properties of sensitized and corroded aluminum have yet to be reported in the literature.

For this section of research, dog bones were made from sensitized Alcoa 5083-H116 exposed to 100°C and 150°C, along with Novelis 5083-H116 exposed to 100°C. Samples were then exposed

to accelerated corrosion in 3.5% NaCl solution with pH 8.3 for up to 120 hours. Measurements in terms of thickness loss and penetration depth/area were used to more accurately report tensile and creep mechanical properties. Along with the corrosion damage, changes in DoS including α grain size changes and β precipitation (correlated from NAMLT) were used to help correlate degradation in σ_Y, σ_U, and creep properties. Room temperature tensile testing and elevated temperature creep testing were performed on sensitized and corroded Alcoa 5083-H116 dog bones. Novelis 5083-H116 was sensitized in the lab and further exposed on Cowley Beach for up to two years and was mechanically tested after exposures. Upon completion of mechanical testing and microstructure characterization, modeling for sensitization and corrosion combination damages is suggested.

3.2 Objectives

The focus of this research was to investigate the effects of sensitization and corrosion on the mechanical response of AR 5083-H116 aluminum alloy. Before this research, some studies investigated sensitization and corrosion on aluminum alloys that had undergone recrystallization, which creates a more equiaxed grain structure prior to damaged states. This research will explore the role of using AR 5083-H116 aluminum alloy, which is a strain-hardened rolled material with a more textured grain structure. This elongated structure has been shown to have a corrosion susceptible-resistant-susceptible (C-SRS) surface present in the through thickness surface orientation. It is hypothesized that this non-recrystallized initial grain structure will lead to differences in corrosion that will depend on the exposed aluminum surface orientation. In addition, the aluminum alloy may be more affected by the accelerated aging conditions since the material has not undergone recovery and recrystallization prior to sensitization. The impact of sensitization and corrosion on AR materials will be quantified through microstructure evaluation and mechanical property measurements.

The three specific research objectives include:

- Determining the effect of the accelerated aging temperature on the sensitization, corrosion, microstructure, and mechanical properties.
- Exploring the impact of textured grain structure on the corrosion of aluminum alloys.
- Developing a method to predict residual mechanical properties of aluminum alloys following sensitization and corrosion.

4 Experimental Methods

4.1 Overview

Various experiments were required to quantify the relationship among sensitization and corrosion damage and the microstructure and mechanical properties of Alcoa 5083-H116. First, samples were exposed to a sensitization environment at two sensitization temperatures for various times. The microstructures of these samples were investigated via two forms of etching to allow α grain and β precipitate quantification. Along with microstructure characterization, small-scale samples were prepared for accelerated corrosion experiments which consisted of potentiodynamic scans and potentiostatic holds. Sensitized dog bone samples were machined for mechanical property characterization with quasi-static tension and creep testing. Some sensitized dog bone samples were exposed to an accelerated corrosion environment prior to mechanical testing. The details of these experimental procedures are discussed in the following sections of this chapter.

4.2 AA5083-H116 Alloy Sensitization

AA5083 manufactured by Alcoa was procured in the form of plates that were 914 mm (L) X 1200 mm (T) X 6.35 mm (S). In its AR state, the material retained the effects of cold-rolling and the corrosion resistant strain-hardened H116 temper [63], [84], [89]. The chemical composition of the alloy is displayed in Table 4-1.

Table 4-1 Alcoa AA 5083-H116 average chemical composition (wt%).

Alloy	Mg	Mn	Fe	Zn	Si	Cr	Cu	Ti	Al
5083-H116	4.4	0.57	0.24	0.119	0.11	0.09	0.06	0.006	Bal

The AR plates were cut down to smaller plates that were 63.5mm (L) X 78.7 mm (T) X 6.35 mm (S), and they were placed in a TMX T40RS-2.0 environmental chamber at a sensitization temperature of 150ºC and 0% relative humidity (RH). The sensitization times ranged from zero (AR) to 2000 hours. To characterize sensitization effects from two different temperatures, plate sizes of 50.8 mm (L) X 50.8 mm (T) X 6.35 mm (S) were sensitized at 100°C from the AR state to 1543 hours. For microstructure investigation (along with etching), samples at sensitization conditions were created. For the LT surface orientation, samples were 12.7 mm (L) X 12.7 mm (T) X 6.35 mm (S). The LS samples were 12.7 mm (L) X 6.35 mm (T) X 6.35 mm (S) and TS

samples were 6.35 mm (L) X 12.7 mm (T) X 6.35 mm (S). Small-scale corrosion experiments were performed on section sizes of 6.35 mm (L) X 6.35 mm (T) X 6.35 mm (S).

ASTM G-67 NAMLT was used to obtain the DoS of each temperature/time combination present. Previous studies have found alloys with a DoS below 20 mg/cm² are corrosion resistant, while those exhibiting a DoS higher than 20 mg/cm² have some degree of corrosion susceptibility to IGC, SCC, or exfoliation damage [3], [28], [49]. Once NAMLT mass-loss values for different sensitization temperatures and times were calculated, plates for mechanical testing samples were sensitized at desired conditions. Plate sizes for room temperature samples were 203.2 mm (L) X 304.8 mm (T) X 6.35 mm (S). Plate sizes for elevated temperature samples were 228.6 mm (L) X 304.8 mm (T) X 6.35 mm (S). Plate sizes for creep samples were 304.88 mm (L) X 215.9 mm (T) X 6.35 mm (S).

4.3 Microstructure Quantification

4.3.1 Sample Sectioning and Preparation

Microscope samples were cut into the smaller sizes described above. The small samples were cut from the sensitized plates using an Allied TECHCUT Precision Low Speed saw at 200-250 RPMs. Next, Allied EpoxySet resin/hardener was used to mount the samples with either the LT, LS, or TS surface exposed. The liquefied resin/hardener mixture with samples in mounting cups was subjected to a vacuum of 84.7 KPa for 30 minutes to remove any air bubbles and was allowed to cure for another 7.5 hours (8 hours total cure time) in an Allied VACUPREP device. After curing, the mounted samples were ground and polished using an Allied METPREP 3 Grinder/Polisher with PH-3 Power Head. Table 4-2 summarizes the parameters used to give samples a 0.05 μm colloidal silica surface finish (mirror reflection) so there could be few to no scratches. Samples were then rinsed in ethanol to ensure cleanliness and remove surface contamination.

Table 4-2 Small-scale polishing requirements [90].

Consumables	Abrasive Size (P-Grading)	320 grit	600 grit	6 μm	1 μm	0.05 μm
	Abrasive Type	Silicon Carbide		Polycrystalline Diamond		Colloidal Silica
	Carrier	Abrasive Disc		Glycol Suspension		Solution
	Polishing Cloth	-	-	Gold Label	White Label	Chem-Pol

	Coolant	Water	Green Lube	Red Lube	Water Rinse
Settings	Platen Speed/Dir.	300 / Comp	150 / Comp		
	Sample Speed (RPM)	150			
	Force (lbf)	5	4	4	3
	Time (min)	1	3		1

4.3.2 Etching and Microscopy of Sensitized Alcoa 5083-H116 Grain Structures

Prior to microstructure characterization on a Carl Zeiss Axio Vert A.1 optical microscope, samples were etched on LT, LS, and TS surfaces. Magnifications ranged between 50X to 1000X resolution. Emphasis was placed on the LT and LS due to LT being the rolled surface and LS being the through thickness surface of the plate material. Also, the LS and TS surfaces were expected to have similar grain structures from the rolling process [3], [83]. Two etching methods were utilized to characterize the microstructure: Barker's etchant and phosphoric acid etching.

The Barker's etchant method consisted of exposing a polished sample to 2.5% (v/v) HBF_4 at 10 V for 1 to 2 minutes using the Buehler Electromet Etcher. The goal of etching with the Barker's etchant was to highlight the differences in grain orientation (and reveal GB in more sensitized materials). Grains of different orientations appear as blue, purple, and pink when exposed to polarized light [3], [84]. The expectations are to:

1. See the effects of cold-rolling when comparing Barker's etched LT, LS, and TS surface orientations and
2. To obtain quantitative measurements of α grain sizes.

Figure 4-1 consists of BF and polarized light images on the same location of one sample. Figure 4-1 (a) reveals a somewhat uniform pitting attack from the Barker's etchant while not highlighting GB. Figure 4-1 (b) helps highlight distinctions between different α grains.

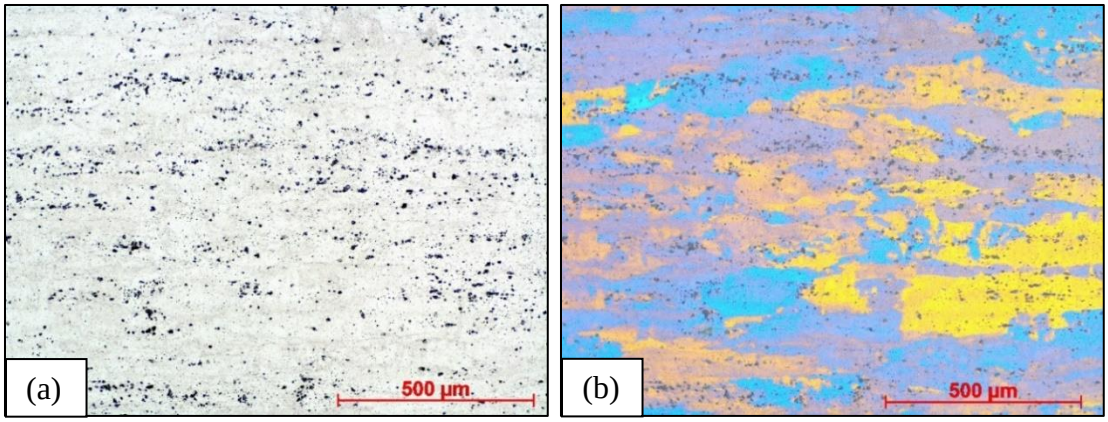

Figure 4-1 Barker's etching of AA5083-H116 at 100X of the corrosion resistant 20 mg/cm² LT surface with (a) BF and (b) polarized light.

After completion of the Barker's etchant studies, as a separate process, selected samples were subjected to phosphoric acid etching, which erodes the anodic β precipitate (Al_3Mg_2) [3]. The phosphoric acid etching consisted of 10% (v/v) H_3PO_4 and a sample exposure time of 1 minute. The eroded β phase is gray and white along GB under polarized light. Samples that were phosphoric acid etched and observed through BF could also be used to trace GB as the eroded β phase was no longer present. Figure 4-2 contains images taken at 1000X magnification on heavily sensitized (DoS = 51 mg/cm²) 5083-H116 in the LT and LS surface orientations. Note the difference in grain structure from the rolling process, with the LT surface grains being approximately equi-axial and the LS surface having elongated grains. Quantification of the α grain size changes based upon sensitization time, temperature, and level can be used to help explain significant differences in corrosion and mechanical properties.

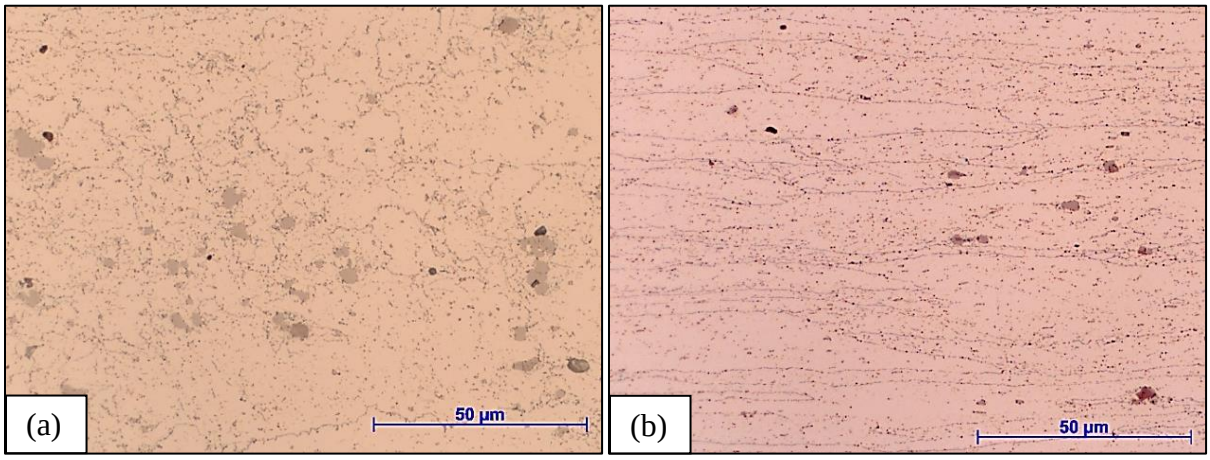

Figure 4-2 Phosphoric etched 150°C sensitized AA5083-H116 at 1000X BF of the corrosion susceptible (a) 51 mg/cm² LT surface and (b) 51 mg/cm² LS surface.

Verification of the β phase presence along the GB was achieved using a Carl Zeiss Axiovert A.1 optical microscope and a LEO (Zeiss) 1150 field-emission SEM at the Nanoscale Characterization and Fabrication Laboratory. Figure 4-3 illustrates α grains (light gray) and β precipitates (dark gray) along the GB.

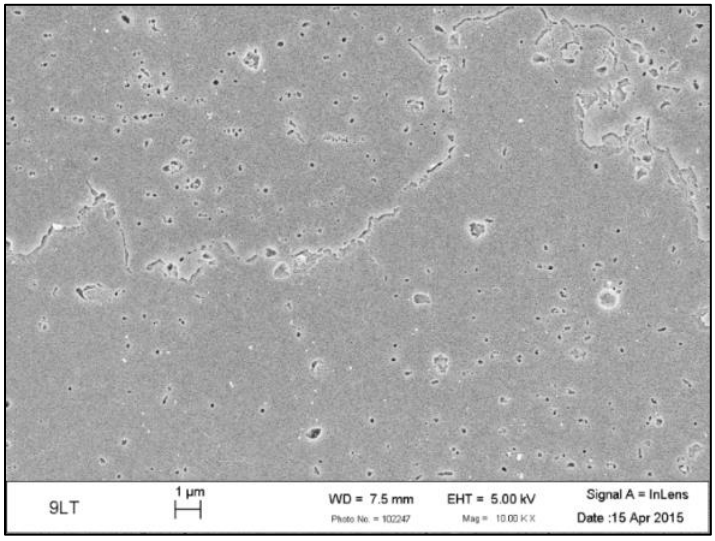

Figure 4-3 SEM verification of β phase along GB, taken at 10000X.

From the BF images taken after etching, α grain sizes can be determined with the use of the Linecut algorithm and ASTM E112-13 [91], [92]. The lineal intercept method is used and requires five images taken across the etched LT or LS sample at any given magnification; however, α grain size estimations can be made from a minimum of three areas of a given specimen. For LT surface orientations, between three to five images were taken at 100X magnification, creating a 1000 µm (L) X 1300 µm (T) viewable surface area. An example of the lineal intercept method is shown for an etched AR sample at 100X magnification in Figure 4-4.

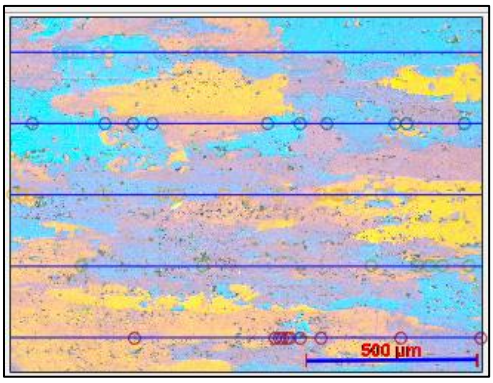

Figure 4-4 Lineal intercept method for LT alpha grain size measurement in the L direction.

Ten lines were applied across the L direction measurements and five lines were applied across the T direction of each image to create the relative accuracy (<10%) required by ASTM E112-13 [91]. For the LS surface orientation, five images were taken at 200X magnification; fifteen lines were used for L direction grain lengths and five lines were used to obtain S direction grain lengths for a relative accuracy (<10%). Also, three sets of measurements were conducted on the LS surface, as well as the top, middle, and bottom of the through thickness or LS surface. The goals were to capture differences in LS surface grain sizes that were present through the plate thickness and to identify the presence of the corrosion susceptible-resistant-susceptible (C-SRS) structure previously reported by Mills et al. and Wei et al. [47], [84]. The average intercept length, $\bar{\ell}_{direction}$, was gained from each set of measurements, so for each surface orientation up to five sets of measurements were taken (3 to 5 images). Equation 4.1 shows the representation of the $\bar{\ell}_{direction}$ per image [91]. The average (between three and five values) of the $\bar{\ell}_{direction}$ measurements are used to quantify the average grain length in different surface directions.

$$\bar{\ell}_{direction} = \frac{\sum \bar{\ell}_i}{n} \qquad 4.1$$

The surface orientation grain length calculations are shown below in equations 4.2 and 4.3 respectively [91].

$$\bar{\ell}_{LT} = \sqrt{(\ell_L \cdot \ell_T)} \qquad 4.2$$

$$\bar{\ell}_{LS} = \sqrt{(\ell_L \cdot \ell_S)} \qquad 4.3$$

Here ℓ_L is the grain length in the L direction, ℓ_T is the grain length in the T direction, and $\bar{\ell}_{LT}$ is the average grain length for the LT surface orientation. The standard deviation, *s*, was obtained for the average of the measurements (n = 3, 4, or 5). With the assumption of a tetrakaidecahedron grain shape, the LT grain diameter, $\bar{D}_{LT}$, and the LS grain diameter, $\bar{D}_{LS}$ are calculated in equations 4.4 and 4.5, shown below [91] .

$$\bar{D}_{LT} = 1.571 \cdot \bar{\ell}_{LT} \qquad 4.4$$

$$\bar{D}_{LS} = 1.571 \cdot \bar{\ell}_{LS} \qquad 4.5$$

4.3.3 Orientation Image Mapping Microscopy

OIM occurred on the LT surface of a heavily sensitized 5083-H116 sample. The sample was polished down to a 0.05 µm colloidal silica surface finish. Afterwards the sample was rinsed in water and the colloidal silica was removed carefully with a wet Q-tip. Next the sample was rinsed in ethanol and dried with compressed air. The Buehler Vibromet 2 Vibratory Polisher was used on the sample with 50%/50% 0.02 µm colloidal silica and distilled water. A sinusoidal amplitude of 40% was selected as the vibration rate, and no weights were added to the sample holder. The sample was vibrated for 1.75 hours and was rinsed in water and then dried with compressed air.

The Helios NanoLab 600 was used to obtain the OIM with the EBSD detector. The sample was mounted with conductive tape, with a piece of tape touching the sample and grounding it. The sample sat at 70° to create Kaguchi bands for measurements. The xT microscope control software was used to control the EDAX TSL EBSD detector. TEAM EDAX software was used to capture the EBSD map. After sufficient vacuum pressure was present, the stage was zeroed. The power of the electron beam was set to a power with 30.0 kV and 0.7 nA current. The dynamic focus was selected, and tilt correction features under Tilt Correction were set to ensure the tilt angle was 70°. Next the sample was moved in view of the detector and then the working distance was set to 13 mm. Settings such as lens alignment and stigmation were accounted for prior to taking images. A magnification of 700X was used to gain OIMs and the EBSD detector was moved closer to the sample.

4.4 Corrosion Characterization Techniques

Two different types of corrosion experiments were performed on the sensitized Alcoa 5083-H116 samples prior to microstructure imaging and mechanical testing. Before any of these tests were conducted, the reference electrodes were tested for stability. OCP was measured prior to any corrosion experiments. Potentiodynamic scans and potentiostatic holds were further used to quantify the effects of accelerated corrosion on the samples.

4.4.1 Reference Electrode Stability

A GAMRY Interface 1000 Potentiostat/Galvanostat was used to perform all corrosion tests in this work. After the device calibration, reference saturated calomel electrode (SCE) testability was verified with two tests: OCP and electrochemical impedance spectroscopy (EIS). The OCP ran for

five minutes and tested the reference SCE vs. the main SCE (main SCE was not used in actual aluminum corrosion experiments) in 150 mL of potassium chloride (KCl), with the goal of having less than 5 mV difference as stated by GAMRY [93]. The working electrode and working sense alligator clips (blue and green) were connected to the reference electrode while the main SCE was connected to the reference alligator clip (white). Once a reference SCE passed the OCP test, it was subjected to an impedance test in 150 mL of 0.6 M NaCl (corrosion test solution) with the reference SCE having the working electrode and working sense alligator clips (green and blue), and the graphite rod counter electrode was connected to the counter electrode and reference electrode alligator clips (red and white). For the impedance test, the reference electrode had to have less than 1 kOhm impedance and a low phase angle [94]. Figure 4-5 a illustrates the corrosion cell used for reference testing versus a main reference electrode, while Figure 4-5 b shows the corrosion cell for testing reference electrode impedance.

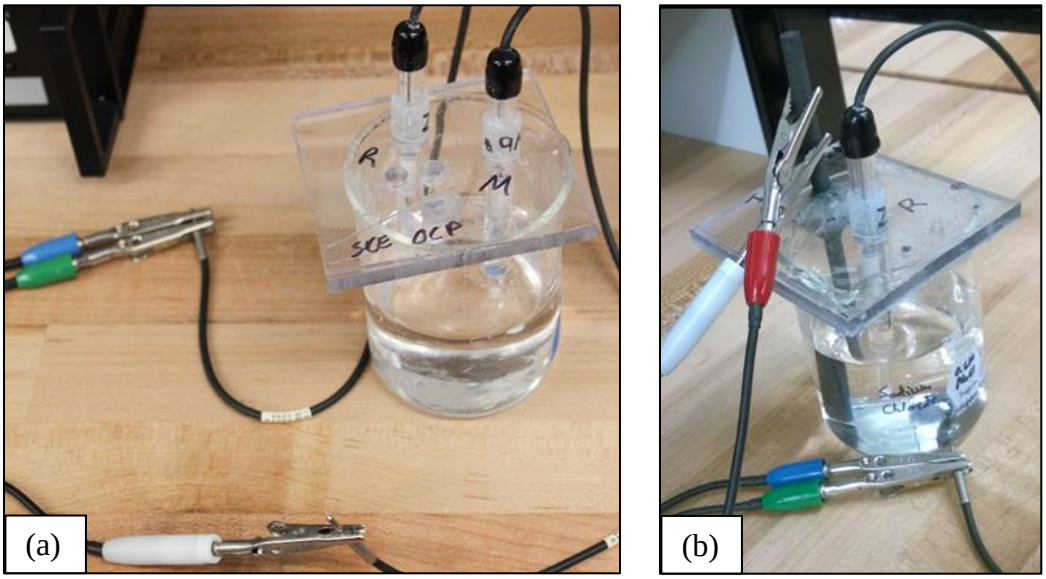

Figure 4-5 Reference electrode testing: (a) OCP and (b) EIS impedance.

4.4.2 Open Circuit Potential

For small-scale testing, a reference SCE was connected to the white reference electrode lead, and a 152 mm long graphite rod of 6.35 mm diameter was connected to the red counter electrode lead as the counter electrode. The sensitized AA5083-H116 sample with an exposed surface area of 40.3 mm² was utilized as the working electrode and was connected to the blue working electrode and green working sense leads. The small-scale samples were mounted in epoxy as discussed

previously, and an insulated 14-gauge copper wire was connected to the aluminum sample. The copper wire was threaded and the epoxy was tapped for 2-56 UNC thread size to ensure there would be no issues in connectivity during testing. Electrical conductivity grease was applied to the threaded portion of the copper wire. The copper wire then was screwed into the epoxy by hand until the wire contacted the sample and hot glue was applied to the copper wire and epoxy interface. The insulation of the copper wire was also slid down to create another barrier under the glue to ensure no corrosion solution leaked into the Al-Cu surface interface, which would have caused a short circuit effect. A CAD schematic of the corrosion cell is provided in Figure 4-6 (a). Figure 4-6 (b) demonstrates the small sample corrosion cells as it appeared during testing. The exposed surface was roughly less than 6.35 mm from the Vycor porous tip of the reference SCE, which was 19.05 mm from the graphite counter electrode rod. The three electrodes were in a line with each other, and the counter electrode was roughly 25.4 mm away from the working electrode exposed surface. Figure 4-6 (c) illustrates the test cell setup for mechanical testing (tension and creep) samples. The small-scale sample corrosion was placed in 150 mL of 0.6 M NaCl at pH of 8.3, with the tensile and creep test samples in 800 mL of equivalent solution composition.

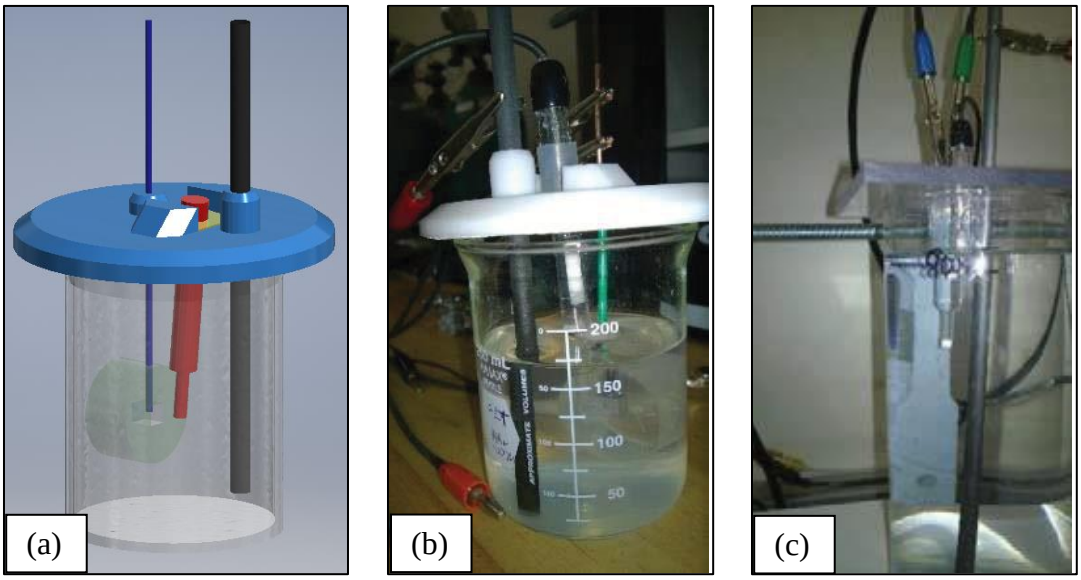

Figure 4-6 (a) Small-scale corrosion cell during testing, (b) small-scale corrosion testing in CAD, and (c) tensile test specimen corrosion cell [84].

4.4.3 Potentiodynamic Scans

As suggested by the literature, potentiodynamic (PD) scans were used to obtain selected electrochemical properties of the sensitized samples at various sensitization levels on the LT

surfaces [3], [45], [65], [72], [74]. Properties of interest gained from PD scans are OCP, pitting potentials (E_{pitt}), breakdown potentials (E_{br}), and/or spreading potentials (E_{spr}). Anodic and cathodic potential regions, along with passivation regions, are often attained from these scans. The same experimental setup shown in Figure 4-6 (b) was used for PD scans; the parameters for the experiments are summarized in Table 4-3.

Table 4-3 Potentiodynamic Scan Test Parameters [84].

PD Scan Parameter	Parameter Value
OCP Time	30 minutes
Scan rate	0.167 mV/second
Starting Voltage	-150 mV_{SCE} from OCP or at OCP
Final Voltage	-600 mV_{SCE}

To determine the spreading potential for use in the AA5083-H116 (sensitized at 100°C or 150°C) corrosion testing, an anodic PD scan was conducted on three samples at each of the DoS levels for microscope and mechanical testing of samples based on studies by Lim et al. and Jain et al. [3], [72]. Figure 4-7 presents the PD scan of the heavily sensitized (DoS = 61 mg/cm²) LT surface and the intersection of two lines method. The E_{br} or E_{spr} was obtained as the intersection of two separate logarithmic fits of the potential versus current density, as illustrated in Figure 4-7. The intersection method was used because a clear distinct rapid change in current density was not obvious [3], [72]. The corresponding spreading potential was determined to be -0.77 V_{SCE} for the material sensitized at 150°C. A similar approach was used to find the spreading potential of -0.755 V_{SCE} for material sensitized at 100°C.

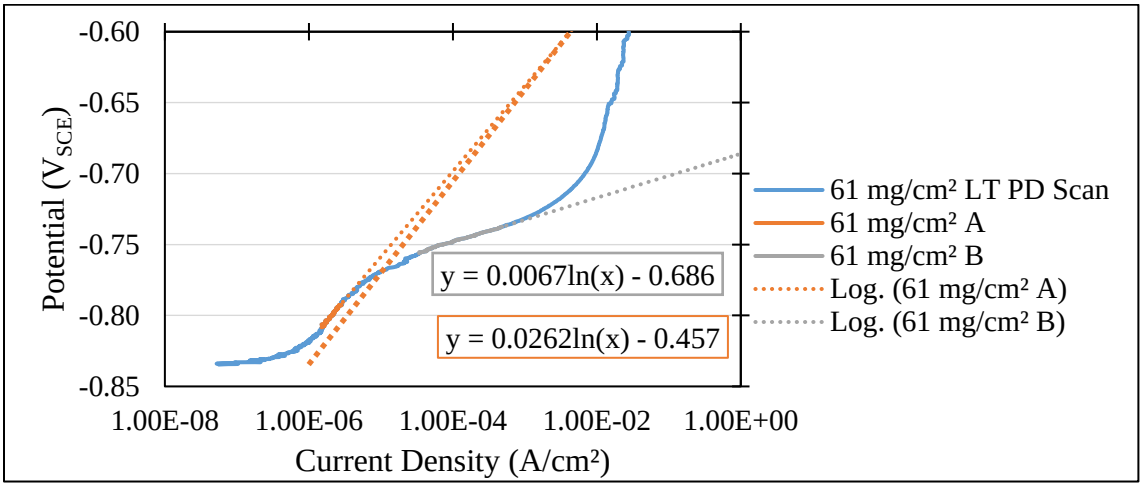

Figure 4-7 Potentiodynamic scan of sensitized AA5083-H116 with DoS of 61 mg/cm² (example of potential verification).

4.4.4 Potentiostatic Holds

After the E_{spr} was obtained from the potentiodynamic scans, potentiostatic (PS) holds were performed on the LT surface orientation of AA5083-H116 sensitized at 150°C. Based upon research by Lim et al., three voltages of -0.77, -0.78, and -0.79 V_{SCE} were used for these tests with samples having a DoS of 70 mg/cm² and a testing time of up to 1.5 hours [3]. This test is represented in Figure 4-8, correlating PS hold voltage and current density. Bright field images taken at 500X magnification are provided in Figure 4-8; they highlight the extent of pitting and IGC damage for each applied voltage. At a potential of -0.77 V_{SCE}, the β phase is attacked along the GB, and pitting is evident across the α surface. At potentials -0.78 and -0.79 V_{SCE}, there is less evidence of the grain boundary β phase attack as well as less pitting. Based on this PS verification and PD scans, a voltage of -0.77 V_{SCE} was used for all accelerated corrosion tests conducted on small-scale samples, tensile, and creep specimens that were sensitized at 150ºC.

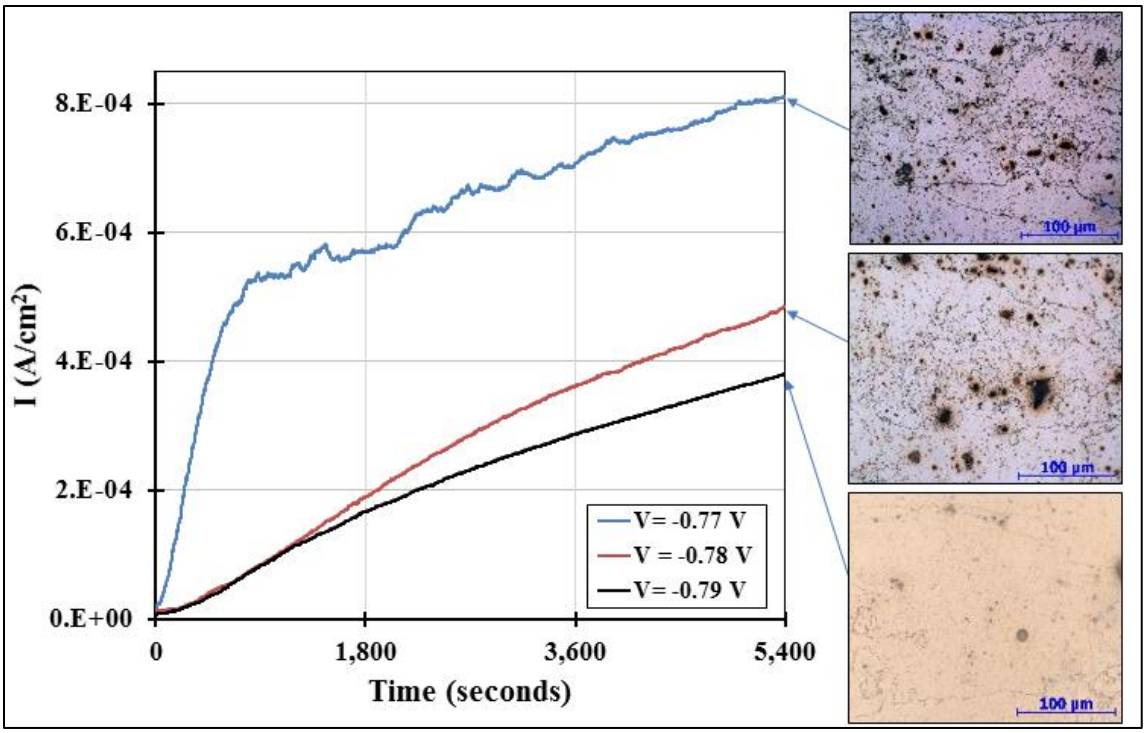

Figure 4-8 Potentiostatic hold voltage verification results for 5,400 seconds or 1.5 hours of accelerated corrosion of the AA5083-H116 LT surface with DoS 70 mg/cm² [95].

4.4.5 Corrosion Damage Quantification

Samples sensitized at 150°C with various DoS were corroded at -0.77 V_{SCE} for 3, 12, and 48 hours on both LT and LS surfaces. Three times were selected to see which, if any, led to significant

thickness loss on both surfaces [3], [84]. The effects of corrosion damage on exposed surface orientations were then characterized. A three electrode corrosion cell consisting of a working, reference, and counter electrode was used on small-scale and mechanical test sample corrosion experiments.

Examples of the damage occurring on the LT and LS surfaces for sensitized Alcoa 5083-H116 150ºC small-scale samples are provided in Figures 4-9 and 4-10, respectively. Figure 4-9 (a) illustrates a cross-section of 53mg/cm² exposed to -0.77 V_{SCE} for 48 hours and two types of corrosion damage. Figure 4-9 (b) presents the different regions of the corrosion damage highlighted with different color tints. The area highlighted in blue represents the surface that was initially exposed to the accelerated corrosive environment. The teal region represents the exfoliated section of the corrosion damage, which can be considered completely exfoliated grains (thickness loss) or the region with whole grains flaking off, and which are parallel to the exposed LT surface. The last region is the IGC damage that propagates from the exposed surface and the exfoliated region, termed the penetration depth. The maximum penetration depth values obtained are in the orange region of each of the analyzed images for the LT surface. For the small-scale corrosion tests, measurements based on five images that were taken across the cross-sectioned exposed surface and averaged together to obtain the penetration depth for each sensitization level.

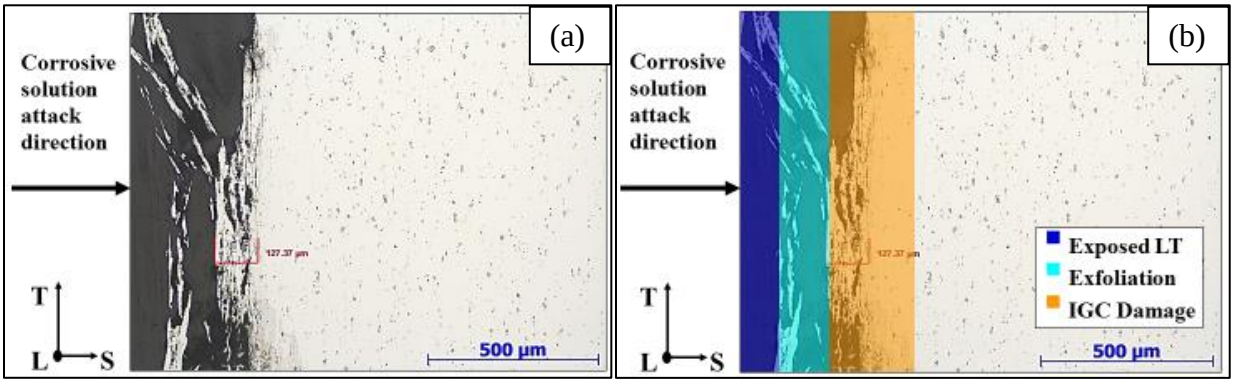

Figure 4-9 LT surface orientation corrosion damage for 51 mg/cm² after 48 hours at -0.77 V_{SCE}. The image was taken at a magnification 200X under bright field (a) without color tints and (b) with color tints highlighting corrosion damage. [96].

The exposed LS surface orientation exhibited different varieties of corrosion damage than that demonstrated by the exposed LT surface. While the LT surface showed a more uniform exfoliation region or LT thickness loss followed by a parallel IGC damage region, the LS surface exhibited

the behavior presented in Figure 4-10, where there is a region that is resistant to corrosion damage. Figure 4-10 (a) contains an exposed LS surface after being exposed to the accelerated corrosion environment while Figure 4-10 (b) presents the different corrosion damages highlighted with different color tints. The blue region once again represents the location and presence of the corrosive 0.6 M NaCl solution contact to the exposed LS surface. The region in teal demonstrates a less uniform exfoliated section followed by perpendicular fissures in the T direction (the highlighted orange regions); these are the corrosion susceptible regions of the corrosion susceptible-resistant-susceptible (C-SRS) structure. The yellow portion of the cross-section highlights the corrosion resistant region of the C-SRS structure. The larger LS penetration depth damage is as expected based on previous studies [3], [83], [84].

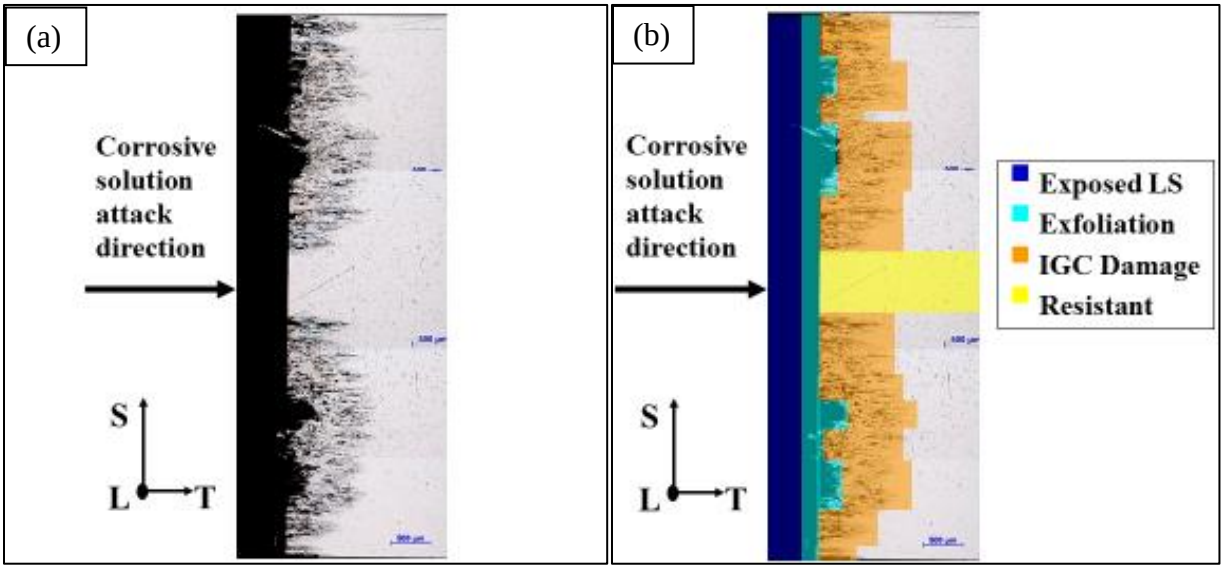

Figure 4-10 LS surface orientation damage for 51 mg/cm² 200X, C-SRS structure present [96].

Based on this study of the corrosion environment with respect to exposed surface orientation, a potentiostatic hold time could be selected for all following corrosion tests performed. Most studies were initially performed on the small-scale microstructure samples sensitized at 150°C, with a voltage of -0.77 V_{SCE}, and with 120 hours selected as the potentiostatic hold time. Samples that were sensitized at 100°C were subjected to a voltage of -0.755 V_{SCE} (upon finding that -0.77 V_{SCE} did not corrode the sample well), and a potentiostatic hold time of 120 hours.

Tensile test specimens were polished method of 320, 600, and 1200 grit abrasive pads. For the LT exposed surface, the Met Prep 3 Grinder/Polisher system was used, while the LS surface was

polished with the same three abrasive types/sizes using a Dynablade (a portable grinding/sanding device). Tension and creep test samples were then coated with RUST-OLUEM Gloss Protective Enamel, with thickness of ~40 µm. The samples were exposed to accelerated corrosion testing on either both LT surfaces (25.4 mm (L) X 12.7 mm (T) per side) or both LS surfaces (25.4 mm (L) X 6.35 mm (S) per side).

The sensitized Alcoa 5083-H116 with DoS of 20 and 51 mg/cm² presented in Figure 4-11 was corroded for 48 hours and 120 hours based upon small-scale corrosion damage results. These samples were subjected to accelerated corrosion at -0.77 V_{SCE} in 0.6 M NaCl 800 mL solution on the LT and LS surfaces, as shown in Figure 4-6 (c). Because the corrosion solution was not agitated, both exfoliation and IGC damage occurred due to a buildup of the corrosion product on the damaged grains; thus, thickness loss occurred. For LT surface-corroded mechanical test specimens, thickness loss was measured after brushing samples off gently to remove any nonstructural exfoliated grains/flakes. Figure 4-11 (a) displays an image of the corroded LT surface after 48 hours of corrosion damage from a -0.77 V_{SCE} PS hold. For sensitization levels 51 mg/cm² or higher, uniform LT exfoliation damage was present at 48 hours, while corrosion resistant samples with DoS <25 mg/cm² did not exhibit exfoliation damage after 120 hours of exposure at -0.77 V_{SCE}. For the LS surfaces, three measurements were conducted per sample to obtain the width changes in the T direction within the C-SRS "sandwich." The LS thicknesses of each zone were also measured. Figure 4-11 (b) highlights two DoS levels of 48 and 120 hour LS surface corrosion damage from -0.77 V_{SCE} PS holds.

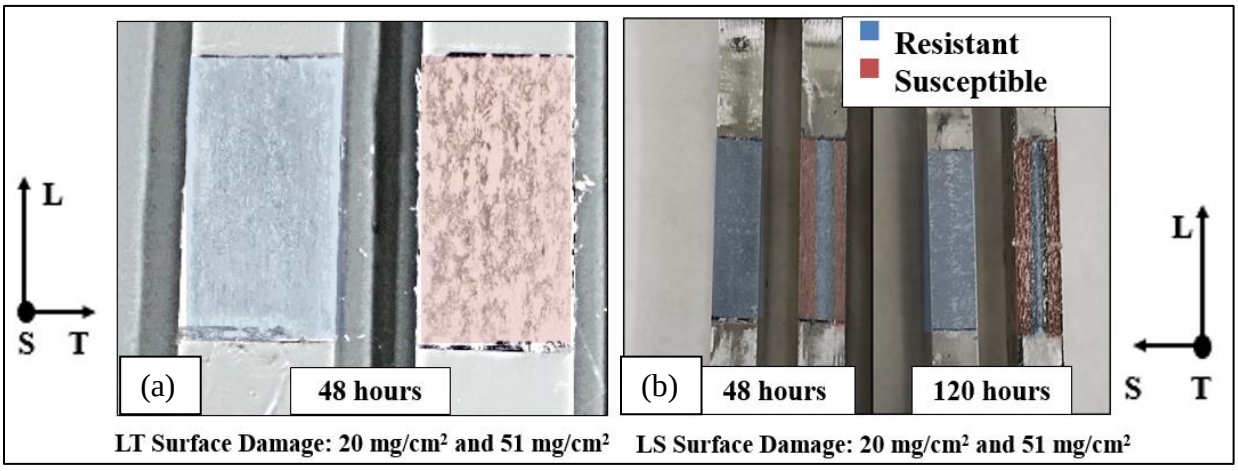

Figure 4-11 (a) LT uniform exfoliation/IGC damage and (b) LS C-SRS corrosion damage of dog bones exposed to an accelerated corrosion environment [96].

4.5 Mechanical Testing

4.5.1 Materials and Geometry

The AA5083-H116 dog bone specimens used for tension testing were of 169 mm (L) X 19 mm (T) X 6.35 (S) mm, with the center of the sample having 12.7 mm (T) width. Creep testing required samples to have an overall specimen length of 228.6 mm (designed for clevis grips) or 215.6 mm (designed for normal grips) in accordance with ASTM E8/E8M-11 [97]. These samples had a gauge length of 50.8 mm and width of 12.7 mm for both types of samples [98]. The plate thickness of the AR and sensitized tension and creep specimens was ~6.35 mm, while corrosion damage led to various thicknesses based on sensitization levels.

4.5.2 Cross-Sectional Area Measurements

Prior to mechanical testing, two types of measurements were conducted on dog bone samples to help determine the cross-sectional area. Samples that were AR or solely sensitized (no corrosion damage present) were measured with digital calipers. This set of cross-sectional area measurements was referred to as original section area (OSA) [84]. Samples that were exposed to the corrosion environment were measured prior to and after corrosion testing. The measurements beforehand were made using the OSA method, while the corrosion damage was characterized with digital calipers to obtain the exfoliation thickness loss damage and then subsequent measurements using a Carl Zeiss Axiovert A1. This is defined as the Post-Corrosion Section Area (PCSA) method [84]. For LT thickness loss, one caliper measurement was made per sample, while multiple were made across the LS C-SRS surface to ensure accurate measurements. The LT penetration depth was measured for different sensitization levels by cross-sectioning the corroded region. These cross-section samples were polished down to a 0.05 μm colloidal silica surface finish and the IGC damage (penetration depth damage) was measured at 200X magnification [98]. For this, 25 images were taken on each exposed LT cross-section and an average value was obtained from these images. Figure 4-12 provides an example of the measurements performed on the LT corroded surface for penetration depth measurements.

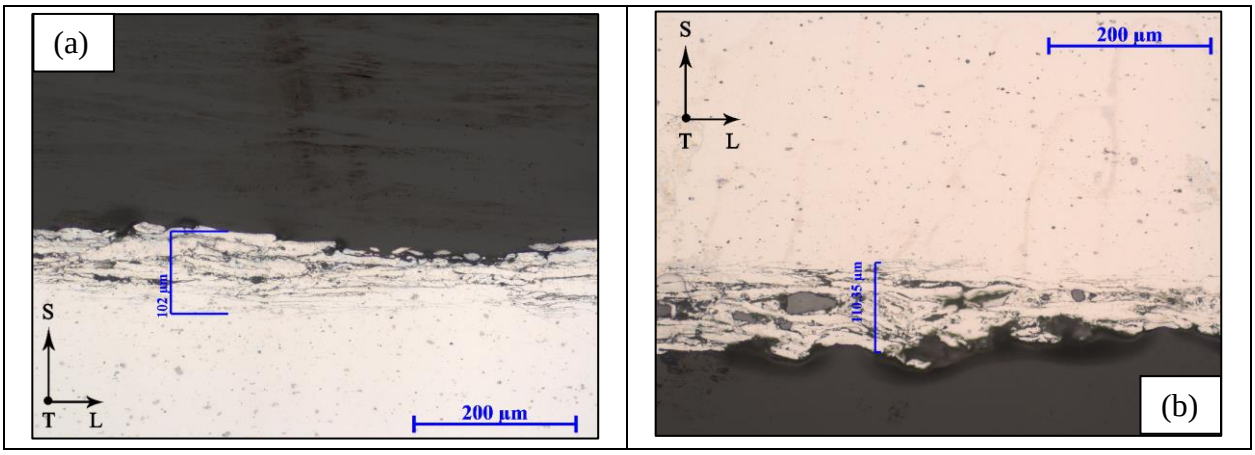

Figure 4-12 Bright field images of cross-section of corroded 51 mg/cm² LT surfaces at 200X magnification, (a) side 1 and (b) side 2 of Alcoa 5083-H116 sensitized at 150°C for 200 hours [98].

4.5.3 Tension Testing Method

For tension testing of any sensitized or sensitized and corroded 5083-H116, an INSTRON 5984 load frame was used. A strain rate of 5 mm/min was used for all testing in accordance with ASTM E8/E8M-11, which requires that a test take less than 10 minutes to break a dog bone [84], [99]. The extensometer used during these tests had 25.4 mm gauge length, with the expectation that samples would break in the 25.4 mm corroded LT or LS damage regions. MATLAB codes were utilized to help interpret stress-strain curves after testing completion to obtain 0.2% offset yield strength (MPa), ultimate tensile strength (MPa), percent reduction in area, and Young's modulus (GPa) [100]. Figure 4-13 presents a sample with the 25.4 mm extensometer in the grips of the Instron prior to tensile testing.

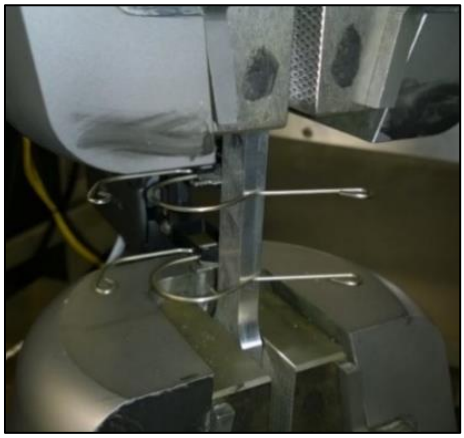

Figure 4-13 Room temperature tensile test dog bone with extensometer prior to testing in the grips of an INSTRON 5984.

Results for elastic moduli, 0.2% offset yield strength, ultimate tensile strength, and percent of area reduction are provided in the results section. For the LT surface, there is only a change in the thickness of the dog bone after corrosion damage. For each of these properties, an assumption of OSA and PCSA was made to account for the thickness loss that occurred during LT corrosion experiments. For the LS surface, the OSA is compared to the PCSA of the C-SRS structure.

4.5.4 Creep Testing Method

4.5.4.1 Elevated Temperature and Stresses

Elevated temperatures during creep testing were introduced into the samples using an Ameritherm 5060LI Induction heater with a heating rate of 50ºC/min. Samples equilibrated at the desired testing temperature for 10 minutes prior to each creep test. A Micro-Epsilon optical infrared pyrometer and Watlow PID controller provided temperature feedback for the induction heating process on the LT surface with only black paint. A FLIR SC655 thermal camera measured the heat during the heating ramp and maximum temperature (simulated fire temperature) during every creep test, with a 25.4 mm inspection line placed across the middle of each dog bone. This ensured that the heating was uniform across the gauge length. Further details on the heating method and FLIR camera measurements are provided by Summers et al. [63].

For the creep tests, six different sensitization levels were utilized, some with and some without corrosion damage. Table 4-4 summarizes the tests performed to identify the effects of sensitization and corrosion damage on the creep properties of 5083-H116. The baseline for these temperature-stress combinations ranging from 200°C to 400°C are based upon previous studies by Allen and Summers et al. [100], [101]. At 200°C, 120 MPa represents 40% yield strength stress, for 300°C, 35 MPa is 40% and 50 MPa is 90%, and for 400°C 13 MPa is 40% and 18 MPa is 90% of AR 5083-H116. No corrosion occurred on samples in the AR (3 mg/cm²) condition and with low DoS (20 mg/cm²) prior to creep testing. Corrosion occurred on some samples with DoS in the IGC susceptible range of 51-66 mg/cm² prior to creep testing. The AR data for 200°C and 400°C testing were obtained from Allen and Summers et al. due to lack of material availability [100], [101]. For samples in which corrosion damage had occurred, the PCSA was used to determine the appropriate loads for the creep tests. Creep testing was conducted in accordance to ASTM E139-11 [97]. Primary, secondary, and tertiary creep data were extracted from the testing results, in addition to the measured creep rupture time (t_r) and creep rupture strain (ε_r).

Table 4-4 Creep experiment matrix for AR, sensitized, and sensitized and corroded AA5083-H116. Three replicate tests were conducted for all cases except those denoted by *, in which case two replicates were conducted [98].

Sensitization (mg/cm²)	Corrosion (Yes/No)	Creep Temp (°C)	Creep Stresses (MPa)
3	No	200	120
	No	300	35, 50
	No	400	13
20	No	200	120
	No	300	35, 50
	No	400	13
51	No	300	35, 50
	Yes	300	35, 50
	Yes	400	13
61	No	300	35*, 50*
	Yes	300	50
66	No	400	13, 18
	Yes	300	50

4.5.5 DIC Speckling Method

Temperature and strain measurements on AR, solely sensitized, and sensitized then corroded samples required that the samples be painted before creep testing. RUST-OLEUM Specialty High Heat black enamel spray paint with a thickness of ~20 µm and known emissivity was used to coat the entirety of both LT surfaces. One LT surface on each sample was speckled with a similar RUST-OLEUM Specialty High Heat white enamel spray paint for strain measurements from the Digital Image Correlation (DIC) system using the process described by Cholewa et al. [102]. Figure 4-14 (a) displays the exposed LT surface pre-corrosion testing and Figure 4-14 (b) provides the post-corrosion damage. Figure 4-14 (c) and Figure 4-14 (d) present the DIC speckling technique on non-corroded and corroded LT surfaces.

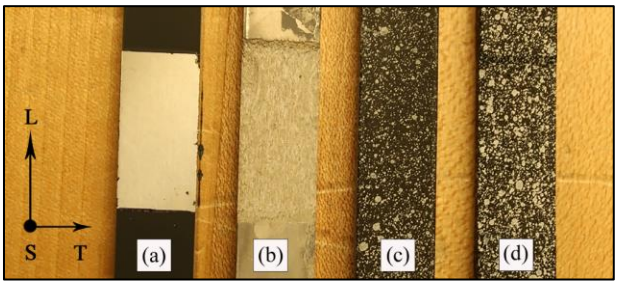

Figure 4-14. (a) exposed LT surface prior to corrosion testing, (b) LT surface post-corrosion, (c) speckled non-corroded sample, and (d) sensitized and LT corroded sample with DIC speckling [98].

4.5.6 DIC System and Infrared Measurements

Along the with elevated temperature measurements from the FLIR cameras, an MTS 880 Load Frame with an MTS Micro Profiler was used to perform creep testing. During each test, a DIC system from Correlated Solutions along with VIC Snap and VIC3D software were used to make strain measurements. The optical hardware consisted of two Allied Vision Technologies Prosilica GX 1600 CCD cameras along with 100 mm Tokina f/8.0 lenses. The cameras were placed approximately 1.73 m from the sample and mounted vertically 0.31 m apart on an aluminum beam. A 12 mm X 4 mm calibration grid allowed for calibration and comparison of the sample against the speckle pattern with 30 pre-creep test images allowed for speckling validity. Each test had the desired subset size of 31 and noise level of 5.5 for data analysis. Image acquisitions began once the creep load was applied, and they were taken at a frame rate of one image per second. Figure 4-15 illustrates a speckled creep dog bone prior to creep testing through the DIC system during a speckle pattern check. The blue line with arrows represents the direction of the applied loads. If the projection error calculated by the DIC software was 0.01 or higher, the samples were either re-speckled, or a different subset and noise level combination were used to reduce noisy data. Further details regarding this measurement process are available in Summers et al. [63].

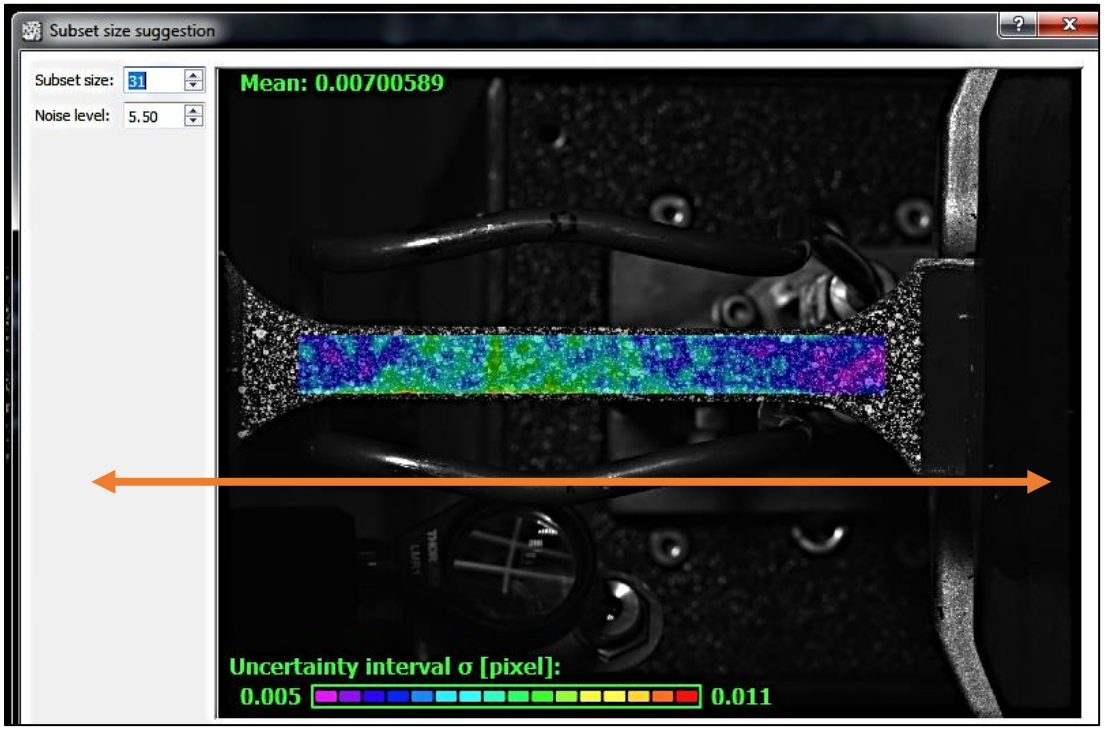

Figure 4-15 Speckle check prior to creep testing.

After testing, a 25.4 mm virtual extensometer was placed on the region of interest as shown in Figure 4-16 (a). Since most of the creep samples were previously corroded, the location of the extensometer was easily found by inspecting the z-axis differences, with the non-corroded portion of the sample being closer, and the 25.4 mm corroded region being further out of plane. Strain measurements were taken until the creep rupture or breaking of the creep sample. Figure 4-16 (b) shows an example of a creep sample post rupture.

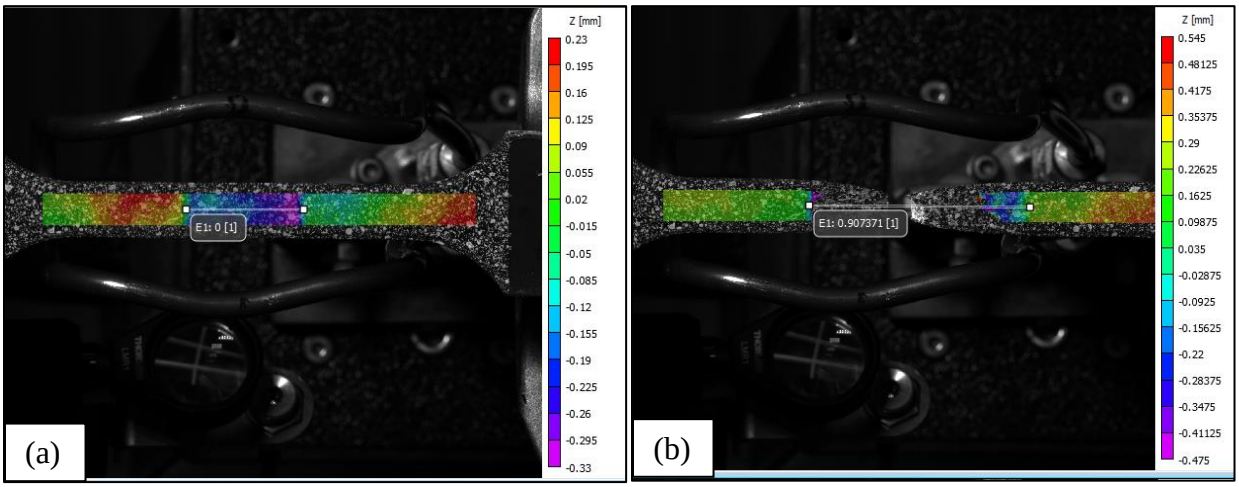

Figure 4-16 DoS 49 mg/cm² corroded LT(a) creep test start & (b) creep rupture.

4.6 Tertiary Creep Modeling Based on Sensitization and Corrosion Damage

Secondary creep (ε_{II}), and tertiary creep (ε_{III}) were observed during tests conducted on the 5083-H116 samples. During creep testing of sensitized and sensitized and corroded 5083-H116, primary creep was insignificant. This is consistent with results from Allen and Summers, et al., who found that primary creep (ε_I) was negligible at temperatures above 250°C [100], [101]. To predict the creep response of structures made from this alloy, a general constitutive model was desirable. Because primary creep was insignificant for temperatures of interest, a model that describes secondary ($\dot{\varepsilon}_{II}$) and tertiary creep ($\dot{\varepsilon}_{III}$) rates was appropriate. The modified Kachanov-Rabotnov model is one such model; it was utilized for different creep conditions including the AR and sensitized 5083-H116 and sensitized and corroded 5083-H116 based on the creep study outcomes [100], [103], [104].

To successfully model the experimental data, the creep rupture time, creep rupture strain, and secondary/steady-state creep rate were required for the various states of the 5083-H116 alloy. Summers, et al. [101] used the modified Kachanov-Rabotnov equation for AR 5083-H116. The

Larson-Miller parameter (LMP) is also used to help predict the material lifetime if time and temperature data are available. Equation 4.6 relates the secondary creep rate ($\dot{\varepsilon}_{II}$) and LMP values.

$$\varepsilon = \dot{\varepsilon}_{II} 10^{(\frac{LMP}{T} - C)} \lambda \left[1 - \left(1 - \frac{t}{10^{(\frac{LMP}{T} - C)}} \right)^{1/\lambda} \right] \qquad 4.6$$

Key equations that make up this modified Kachanov-Rabotnov equation are listed below as equations 4.7-4.12. Experimental creep rupture times (t_r) were obtained per creep condition of temperature (T), stress (σ), and aluminum material constant (C) of ~ 19 log(hours) to obtain the *LMP* based on equation 4.7 [100], [105]. Non-linear least squares regression was used to generate fits for the *LMP* of the sensitized and sensitized and corroded states of 5083-H116. Equation 4.8 contains the *LMP*, with *D* (K), *E* (-), *F* (1/MPa^m), *G* (K), and *n* (-) as fitting parameters.

$$LMP = T(logt_r + C) \qquad 4.7$$

$$LMP = Dsinh(E + F\sigma^n) + G \qquad 4.8$$

Equation 4.9 relates the secondary creep rate ($\dot{\varepsilon}_{II}$) and stress (σ) to various parameters: *A* (s^{-1}), *n*, *m* (-), and ω is the damage progress parameter. *A* is calculated as the y-intercept of the creep strain (y) and creep time (x) data, while *n* is calculated from the slope. Both values become secondary creep constants, while *m* turns into a tertiary constant.

$$\dot{\varepsilon}_{II} = \frac{A\sigma^n}{(1-\omega)^m} \qquad 4.9$$

The damage parameter ω was generated with respect to time *t* using a form of separation of variables in equation 4.10 [101]. *B* (1/MPa), *v* (-), and η (-) become tertiary fitting constants as well.

$$\omega = 1 - [1 - (1 + \eta)B\sigma^v t]^{\frac{1}{\eta+1}} \qquad 4.10$$

Equation 4.11 relates *t* and the t_r as an explicit form for the damage parameter ω [101].

$$\omega = 1 - \left(1 - \frac{t}{t_r}\right)^{\frac{1}{\eta+1}} \qquad 4.11$$

The last fitting parameter λ was obtained from an explicit form relating the instantaneous creep strain to $\dot{\varepsilon}_{II}$ which is explained by Summers et al. [101]. Equation 4.12 shows the final iteration of this explicit form, which relates the fitting parameter λ to $\dot{\varepsilon}_{II}$, ε_r, and t_r. After following the course of equations 4.7-4.12, a set of secondary and tertiary fitting parameters can be generated in terms of A, n, B, η, ν, and λ for the AR and sensitization states and the sensitized and corroded states of 5083-H1116.

$$\lambda = \frac{\varepsilon_r}{\dot{\varepsilon}_{II} t_r} \qquad 4.12$$

5 Sensitization Effects on Alcoa 5083-H116 Surface Orientation Microstructure and Corrosion Resistance

5.1 Sensitization Effects at Different Temperatures

Samples of Alcoa AA 5083-H116 were exposed to a sensitization environment in a TMX environmental chamber at temperatures of 100°C and 150°C. The first goal was to understand the DoS of the AR plate material based upon exposure time and sensitization temperature. Prior to sensitization, the samples were only exposed to the cold-rolling process by Alcoa and not exposed to any solution heat treatments or quenching processes. Figure 5-1 summarizes the sensitization levels at various times for both temperatures, along with which sensitization levels were selected for microstructure and mechanical testing. Samples with a DoS below 15 mg/cm² are corrosion resistant; those with a DoS from 15-25 mg/cm² can experience possible pitting; while those with DoS >25 mg/cm² can experience IGC, and those with DoS > 40 mg/cm² can experience SCC [3], [28], [64]. As expected, the Alcoa 5083-H116 sensitized at 150°C reached the DoS corresponding to the three different corrosion regimes much faster than the Alcoa 5083-H116 sensitized at 100°C.

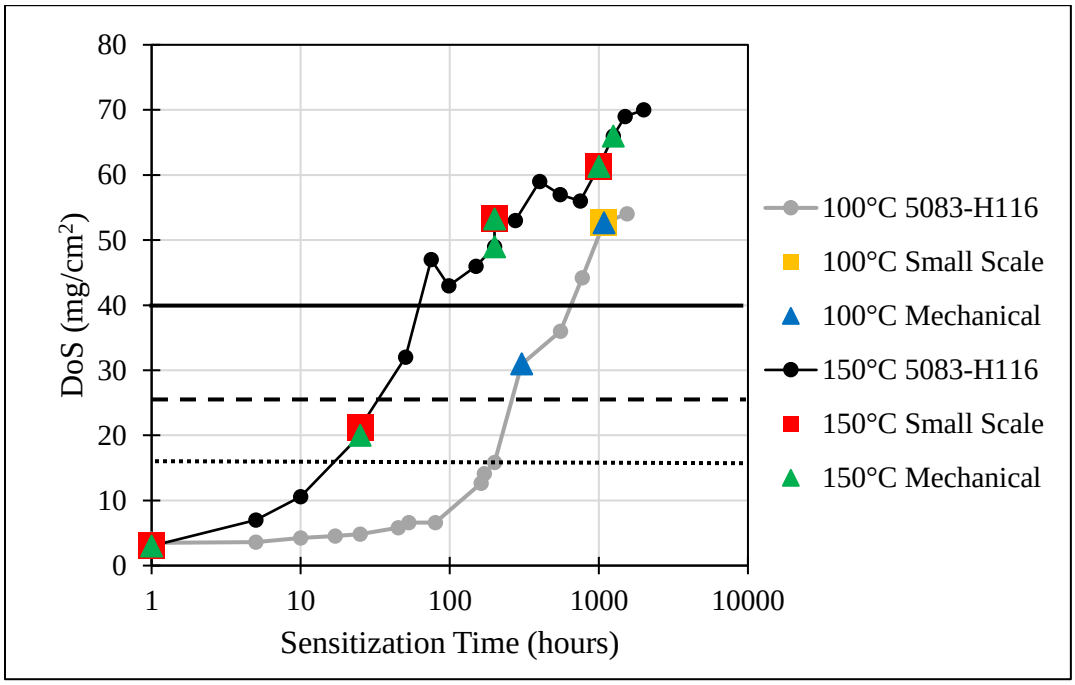

Figure 5-1 DoS for Alcoa 5083-H116 sensitized at 100°C and 150°C.

5.2 Microstructure Investigation

5.2.1 Alpha Grain Size Quantification

Without prior recrystallization, the textured/sandwiched grain structure was present prior to and during sensitization at 100ºC and 150ºC. Figure 5-2 illustrates the LT and LS surfaces of 5083-H116 at three sensitization levels, with 3 mg/cm² being AR material and 51 mg/cm² being heavily sensitized corrosion susceptible material from the sensitization temperature of 150°C. As noted by the top three images of Figure 5-2 and by Table 5-1, the LT surface had a more equi-axial α grain shape, which decreased with increasing sensitization time. (Some recrystallization occurred.) It is also noticeable after phosphoric etching that more β phase (whitish/gray) was present with higher sensitization levels along GB, which is to be expected from the literature. For the LS surface, an elongated grain structure was still present in the heavily sensitized 51 mg/cm², and the presence of β along the GB was more prominent than on the LT surface at the same sensitization levels. This phenomenon was first noticeable after the use of Barker's etchant and phosphoric acid on sensitized LS surface orientations.

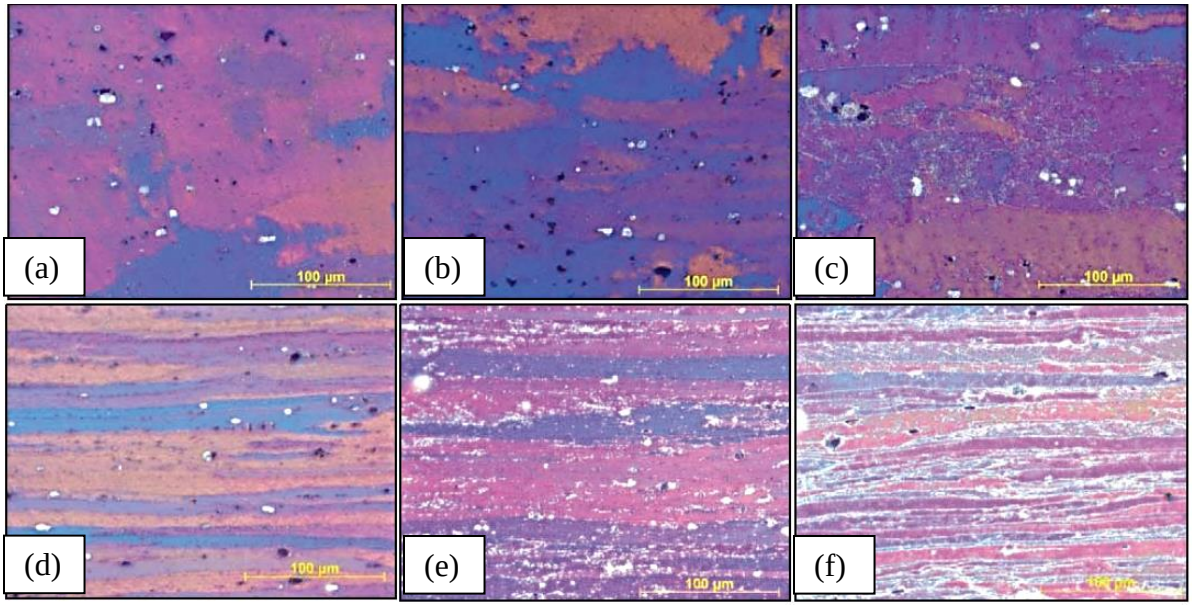

Figure 5-2 Barker's etched and phosphoric acid etched LT surface orientations (top) and LS surface orientations (bottom) with increasing DoS for (a) and (d) 3 mg/cm², (b) and (e) 20 mg/cm², and (c) and (f) 51 mg/cm² sensitized at 150°C [84].

After etching, grain size analysis was performed on various DoS samples for sensitization temperatures of 100°C and 150°C representative of samples exposed to corrosion and mechanical

tests. Grain lengths in each of the two primary directions (L and T) are provided for each DoS in Table 5-1. The average grain size length for the LT surface, $\bar{\ell}_{LT}$, was calculated based on Equation 4.2. A spatial representation of the grain length in the form of diameter, $\bar{D}_{LT}$, was obtained from Equation 4.4, for the tetrakaidecahedron shape model [60]. There was noticeable change in the L and T direction grain lengths for all samples exposed to a sensitization temperature of 150°C. As suggested by Oguocha and Adigun, long-term exposure led to a decrease in grain size [27, 53]. The AR state of the material had $\bar{D}_{LT}$ of 89 µm, while the sensitization temperature at both 100°C and 150°C recrystallized the material. For 150°C, there was a 38% decrease in $\bar{D}_{LT}$ of the 3 mg/cm² to 61 mg/cm² DoS from 89.2 µm to 55.5 µm respectively. The anisotropic index (AI) decreasing is another indication that recrystallization occurred in material sensitized at 150°C. However, when investigating the α grain size alterations from sensitization at 100°C, it was noticeable that only a smaller decrease of 25% from 89.2 µm to 66.8 µm occurred for DoS 53 mg/cm² after 1,084 hours of exposure. The anisotropic index only decreased by 0.1 also. The differences in the rates of recrystallization (time it takes it get the same percent decrease) is temperature dependent and suggests that β phase morphology is different.

Table 5-1 Alcoa 5083-H116 sensitization and LT surface α grain sizes with uncertainties.

DoS (mg/cm²)	DoS Temp (ºC)	DoS Time (hours)	ℓ_L (µm)	ℓ_T (µm)	$\bar{\ell}_{LT}$ (µm)	$\bar{D}_{LT}$ (µm)	AI
3	-	-	80.7±1.5	40.0±0.6	56.8±1.3	89.2±2.1	2.0
20	150	25	58.0±1.9	30.4±0.9	42.0±1.9	66.0±3.0	1.9
51	150	200	52.7±1.3	29.5±1.5	39.4±2.2	61.9±3.5	1.8
61	150	1,000	47.9±1.4	26.1±0.9	35.3±1.6	55.5±2.5	1.8
31	100	304	61.1±1.4	32.3±1.1	44.4±1.8	69.8±2.8	1.9
53	100	1,084	58.8±3.9	30.7±1.3	42.5±3.3	66.8±5.2	1.9

Grain size analysis was performed on the LS surface orientations of the same two DoS levels sensitized at 150°C provided in Table 5-2. For the LS surface, it was notable that a sandwich layer was seen from corrosion testing on the LS surface, and etching showed three distinct bands. Thus, for the LS surface orientation, images were taken in the corrosion resistant-susceptible-resistant sandwich structure, with the expectation that the two R locations (top and bottom) would have different α grain sizes from the S region (middle). To distinguish the regions, *A* represents the top band, *B* represents the middle band, and *C* represents the bottom band. Calculations in Table 5-2 were based upon Equation 4.3 and Equation 4.5.

Table 5-2 Alcoa 5083-H116 150ºC sensitization and LS surface α grain sizes with uncertainties.

DoS (mg/cm²)	ℓ_L (μm)	ℓ_S (μm)	$\bar{\ell}_{LS}$ (μm)	$\overline{D}_{LS}$ (μm)	AI
3 *A*	85.3±1.4	18.0±0.9	39.2±2.0	61.6±3.1	4.7
3 *B*	89.0±3.2	16.9±0.3	38.0±1.6	59.7±2.4	5.3
3 *C*	67.8±2.7	15.5±0.7	32.4±2.0	51.0±3.2	4.4
Average	80.7±4.4	16.8±1.2	36.8±3.2	57.8±5.1	4.8
20 *A*	72.9±3.6	13.7±0.6	31.5±2.1	49.6±3.4	5.3
20 *B*	72.3±3.7	12.8±0.5	30.4±1.9	47.7±3.0	5.6
20 *C*	82.9±3.8	13.6±0.3	33.5±1.7	52.6±2.7	6.1
Average	76.0±6.4	13.3±0.9	31.8±3.4	50.0±5.3	5.7
51 *A*	80.6±3.8	15.9±0.8	39.4±2.5	61.9±3.9	5.1
51 *B*	81.9±2.9	15.3±0.7	35.4±2.1	55.6±3.2	5.4
51 *C*	79.0±1.6	15.0±0.6	34.6±1.5	54.1±2.4	5.3
Average	80.5±5.1	15.4±1.2	35.2±3.6	55.3±5.6	5.2

For the LS surface orientation, the AR and sensitized states had different α grain size measurements. For all 150°C DoS levels, there were no significant differences in $\bar{\ell}_{\mathrm{LS}}$ values and $\overline{D}_{LS}$ values. Anisotropic indices for the AR and corrosion resistant DoS 20 mg/cm² were similar for the middle band. When comparing both DoS tested versus the AR state, there was no relative difference in the microstructure in terms of $\overline{D}_{LS}$ values when taking uncertainty into consideration. One theory as to why these values remain similar to the AR state is that just the β phase morphology is changing throughout the LS surface, meaning that the visible bands present are the Al_2Mg_3 precipitation.

5.2.2 Orientation Image Mapping Results

The highly sensitized and IGC susceptible 66 mg/cm² LT surface orientation was analyzed on the Helios NanoLab 600 to obtain an OIM. The OIM image is shown on the left side of Figure 5-3, with the right side showing the polar mapping of the grains. The direction A1 is the T direction, while A2 is the L direction on the LT surface OIM. Similar to other studies of sensitized 5083-H116, Figure 5-3 helped verify the theory that the misorientation angles between α grains leads to the regions that where the alloy is corrosion resistant or corrosion susceptible [28], [80], [106]. When the misorientation angles are <15°, the alloy is corrosion resistant, due to the β phase nucleating to the locations with misorientation angles >15°. The distinct color differences in the image are different α grains present on the LT surface orientation. When compared to Figure 5-2, the β phase appeared between the distinct color changes when the misorientation angle allowed for the β phase to precipitate easily.

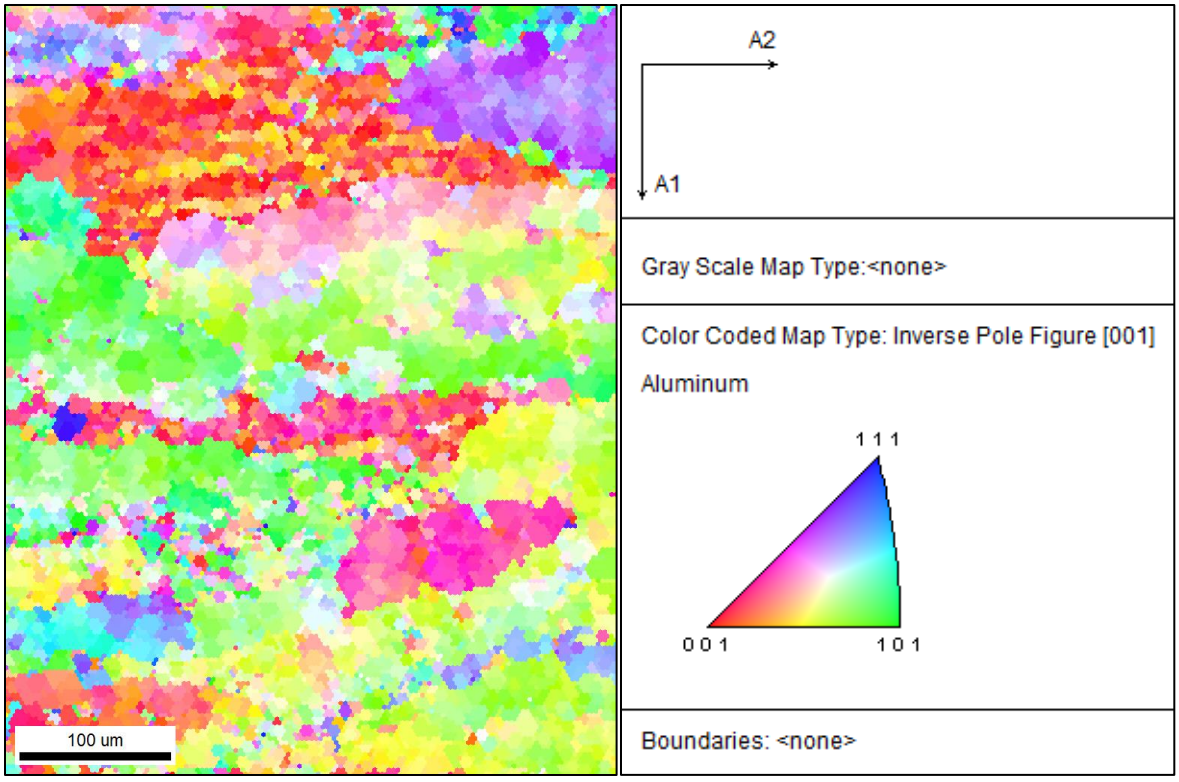

Figure 5-3 OIM of IGC susceptible 66 mg/cm² LT surface orientation, with inverse pole figure. [Personal communication with Manuel Umanzor].

5.3 Corrosion Potential Verification

5.3.1 Potentiodynamic Scans

Along with microstructure analysis and mechanical testing, the sensitized 5083-H116 was exposed to an accelerated corrosion environment. Potentiodynamic scans were performed on sensitized AA5083-H116 to determine various electrochemical properties, specifically spreading potential (E_{spr}) and OCP. Table 5-3 summarizes the results of three PD scans for all Alcoa 5083-H116 sensitized at 150°C. As reported by other studies, the OCP became more active with increasing DoS due to the higher concentrations of Mg as β precipitates along GB versus being dissolved in the α matrix [45], [72]. The spreading potential of -0.77 V_{SCE} was used for all corrosion experiments of AA5083-H116 sensitized at 150°C. For the sensitization at 100°C, the 53 mg/cm² OCP was similar to the 150°C 51 mg/cm² OCP once repeats were taken into account. However, the DoS 53 mg/cm² had a statistically different spreading potential of -0.755 V_{SCE}. The difference in spreading potentials suggests a difference in β phase distribution (continuity and discontinuity), as well as the size of the β phase along GB.

Table 5-3 Potentiodynamic scan data for AA5083-H116 in the AR condition, along with sensitization at 100°C and 150°C.

DoS Temp (°C)	DoS (mg/cm²)	OCP (V_{SCE})	σ_{OCP} (+/-)	E_{spr} (V_{SCE})	σ_{Espr} (+/-)
NA	3	-0.786	0.0238	-0.750	0.0178
150	20	-0.786	0.00416	-0.759	0.00160
150	51	-0.791	0.00544	-0.772	0.00723
150	61	-0.837	0.00691	-0.766	0.00166
150	66	-0.846	0.00497	-0.770	0.00268
100	53	-0.817	0.0120	-0.755	0.00187

5.3.2 Potentiostatic Holds

Once the breakdown or spreading potential was obtained, samples sensitized at 150°C and 100°C were exposed to the accelerated corrosion environment at various lengths of time for small-scale and mechanical dog bone samples. Different surface orientations were exposed to the corrosion environment also. Based on potentiostatic holds, a mass-loss rate could be obtained based on the maximum current density for each corrosion condition based on ASTM G102-89. Equation 5-1 shows the mass-loss rate (MR) with respect to mass-loss rate constant (K_2), current density (i_{corr}), and equivalent weight (EW). For AA 5083 the EW is given as 9.09, and K_2 is given as 0.8953 g/Ad [ASTM 102].

$$MR = K_2 i_{corr} EW \qquad 5.1$$

The results indicate that for tension samples, the corrosion current densities and MRs varied based on DoS and sensitization temperature. For 150°C sensitization, the IGC resistant 20 mg/cm² had the lowest CD and MR values, while IGC susceptible DoS >51 mg/cm² had CD and MR that were statistically higher than the corrosion resistant DoS. The 100°C DoS 53 mg/cm² had a higher corrosion CD and MR than the 150°C sensitized DoS 20 mg/cm² but a lower CD and MR than the 150°C sensitized and IGC susceptible DoS 51 mg/cm² and 61-66 mg/cm².

Table 5-4 Potentiostatic hold data for AA5083-H116 tension samples sensitized at 100°C and 150°C, then corroded on the LT surface for 120 hours at -0.77 V_{SCE}.

DoS Temp (°C)	DoS (mg/cm²)	Current Density (A/m²)	Mass Loss Rate (g/m²d)
150	20	$3.61\text{x}10^{-9} \pm 2.32\text{x}10^{-9}$	$2.93\text{x}10^{-8}$
150	51	$4.32\text{x}10^{-7} \pm 1.21\text{x}10^{-7}$	$3.52\text{x}10^{-6}$
150	61-66	$7.39\text{x}10^{-7} \pm 2.26\text{x}10^{-7}$	$6.02\text{x}10^{-6}$
100	53	$8.33\text{x}10^{-8} \pm 1.32\text{x}10^{-8}$	$7.79\text{x}10^{-8}$

5.4 Corrosion Damage Measurements

5.4.1 Small-Scale Exfoliation Thickness Loss and IGC Penetration Depths

Two sets of exfoliation thickness measurements are detailed in this section. One set is related to the corrosion damage seen in small-scale corrosion samples previously alluded to in Chapter 4.4. The second set of corrosion thickness measurements is discussed for the corrosion of the tension and creep dog bone samples.

Small-scale accelerated corrosion tests were performed on samples with DoS values of 20, 51, and 61 mg/cm² on the LT and LS surface orientations at -0.77 V_{SCE} in a 0.6 M NaCl solution from 3 to 120 hours. Figure 5-4 summarizes the thickness loss from exfoliation damage of the sensitized material for the two surface orientations. As expected, the corrosion resistant 20 mg/cm² had negligible thickness loss on both surface orientations, with the LS thickness loss higher than LT thickness loss. For the highly sensitized samples (DoS equal to 51 and 61 mg/cm²), a more noticeable increase in thickness loss occurred with increasing corrosion time. Once again, the LS surface had greater thickness loss than the LT surface due to the LT thickness loss being from an exposed surface parallel IGC damage, with LS having perpendicular IGC damage. The thickness loss at 120 hours with DoS of 61 mg/cm² LS surface orientation was the greatest.

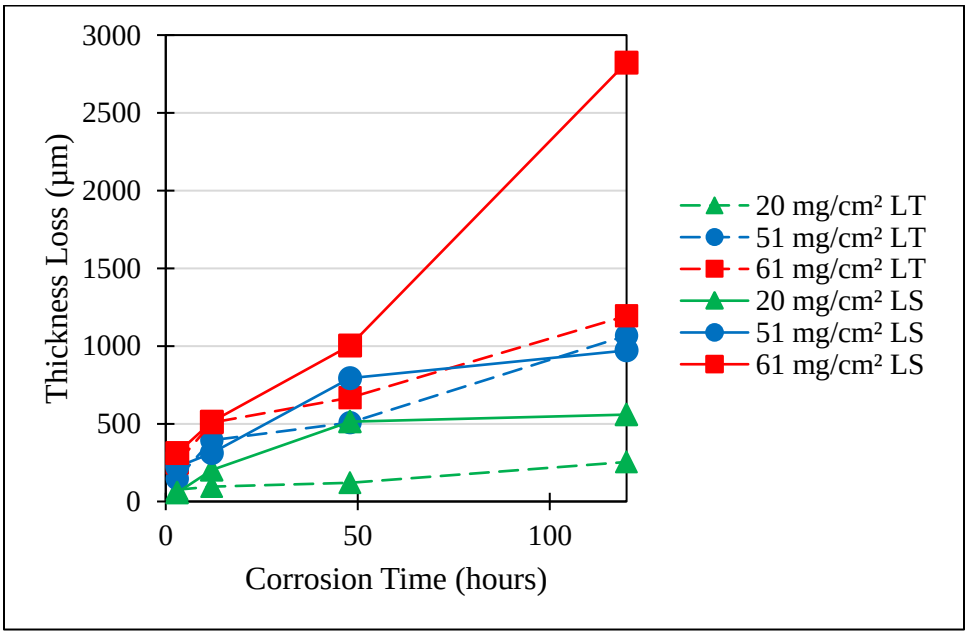

Figure 5-4 Exfoliation thickness losses for sensitized Alcoa 5083-H116 LT and LS surface orientations [84]. [Reproduced with permission]

The second portion of corrosion damage investigation was to consider the corrosion damage beyond the shear thickness loss exfoliated grains, referred to as the corrosion penetration damage or maximum corrosion damage. Figure 5-5 contains the data gathered from the same DoS, surface orientations, and corrosion times shown in Figure 5-4. As expected from the thickness loss data, the maximum penetration depth was greater with the LS surface orientation corrosion damage. After 48 hours of corrosion damage, the LT surfaces had low penetration depth beyond the exfoliated region with a maximum of 184 µm for the highest DoS of 61 mg/cm². The LS surfaces had at least three times greater penetration depth at 48 hours than the LT damaged surface orientations. Both the heavily sensitized LS surfaces had greater than 1000 µm of maximum IGC penetration depth corrosion damage after 120 hours of accelerated corrosion.

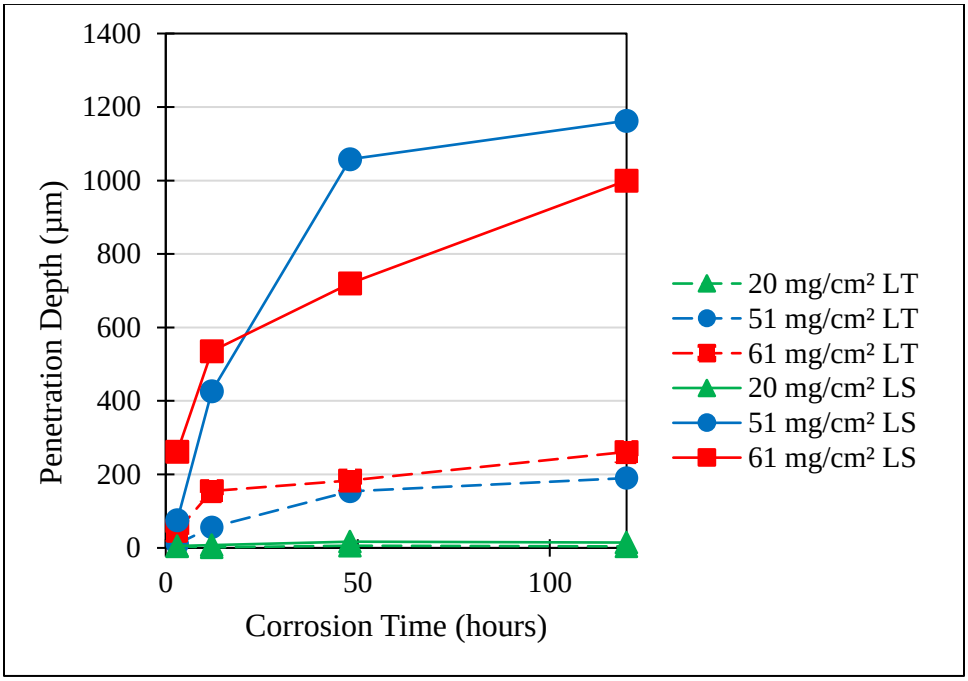

Figure 5-5 Maximum IGC penetration depth for sensitized Alcoa 5083-H116 LT and LS surface orientations [84].

Figure 5-6 presents the relationship of the LT thickness loss for the corroded tension and creep samples sensitized at 100°C and 150°C. Based upon the PD scan data shown previously and the data in Figure 5-4, it is clear that -0.77 V_{SCE} was the correct E_{spr} for the Alcoa 5083-H116 sensitized at 150°C. The LT thickness loss of material sensitized at 150°C increased with increasing DoS that was IGC susceptible, with DoS 51 mg/cm² having nearly one-tenth section area lost with corrosion exposure at 120 hours. The remaining Alcoa 5083-H116 sensitized at 100°C was

corroded at -0.755 V_{SCE} based upon the PD scans; however the thickness loss on samples was minimal compared to the samples sensitized at 150°C.

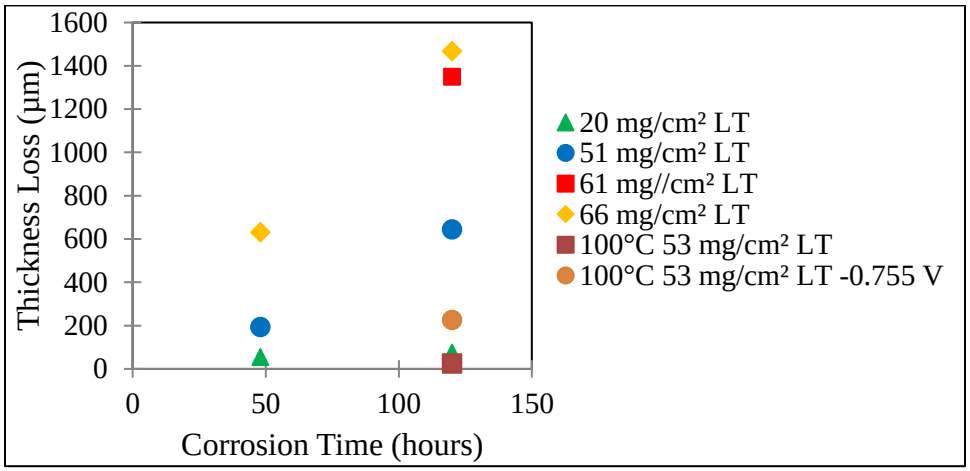

Figure 5-6 Alcoa 5083-H116 sensitized at 100°C and 150°C, exposed on the LT surfaces to the accelerated corrosion environment of -0.77 V_{SCE} in 800 mL of 0.6 M NaCl solution with pH 8.3.

Four sensitization levels are presented in Figure 5-6, with 20 mg/cm² being corrosion resistant and the remaining 51 mg/cm², 61 mg/cm², and 66 mg/cm² being corrosion susceptible for the 150°C sensitization temperature. Like the small-scale samples of Figure 5-4, minimal corrosion damage occurred for a DoS of 20 mg/cm² at 48 and 120 hours. There were increases in LT exfoliation thickness loss for the samples at the remaining three DoS values at resulting from sensitization at 150°C. As expected with a higher sensitization temperature, the LT surfaces of the 150°C material corroded magnitudes more than the 100°C material. Even after using the correct E_{br}, samples sensitized at 100°C and corroded for 120 hours behaved similarly to those sensitized at 150°C and corroded for 48 hours. Samples sensitized at 100°C experienced pitting at -0.77 V_{SCE}, while the samples experienced LT pitting and uniform LT exfoliation thickness when corroded at -0.755 V_{SCE}.

5.4.2 Corrosion Susceptible-Resistant-Susceptible Region Measurements

Samples sensitized at 100°C and 150°C were corroded for room temperature tension testing. Figure 5-7 illustrates the width of the corrosion resistant region of the C-SRS LS structure after being exposed to the accelerated corrosion environment, while Figure 5-8 presents the corrosion susceptible region. Like the LT surface, the LS surface of the Alcoa 5083-H116 sensitized at 150°C with a DoS 20 mg/cm² was corrosion resistant through the entire plate thickness (~6.3 mm or

6300µm). However, samples with a DoS of 51 mg/cm² for the same sensitization temperature of 150°C experienced substantial corrosion susceptibility, losing nearly 2/3 of the LS thickness after 48 hours of exposure, with nearly 1/5 of the LS thickness being corrosion resistant after 120 hours. The material sensitized at 100°C behaved similarly at 120 hours as the material sensitized 150°C. This data, along with Figure 5-5 suggests that the LS has similar β precipitation along the GB for both sensitization temperatures, but exposed B precipitation for the cold-rolled LT surface experienced pitting, non-uniform exfoliation, and uniform exfoliation.

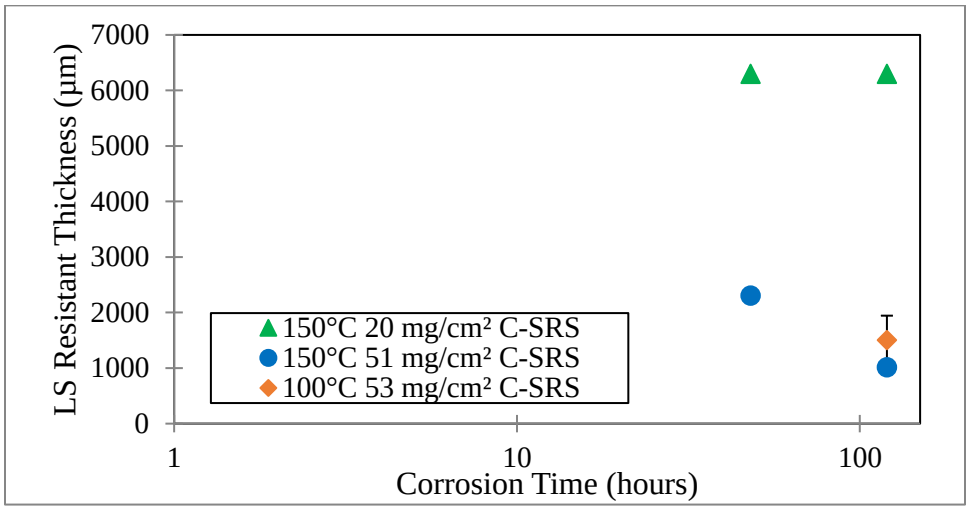

Figure 5-7 Alcoa 5083-H116 sensitized at 100°C and 150°C, exposed on the LS surface to the accelerated corrosion environment. The corrosion resistant thickness of the C-SRS structure values is shown versus corrosion time.

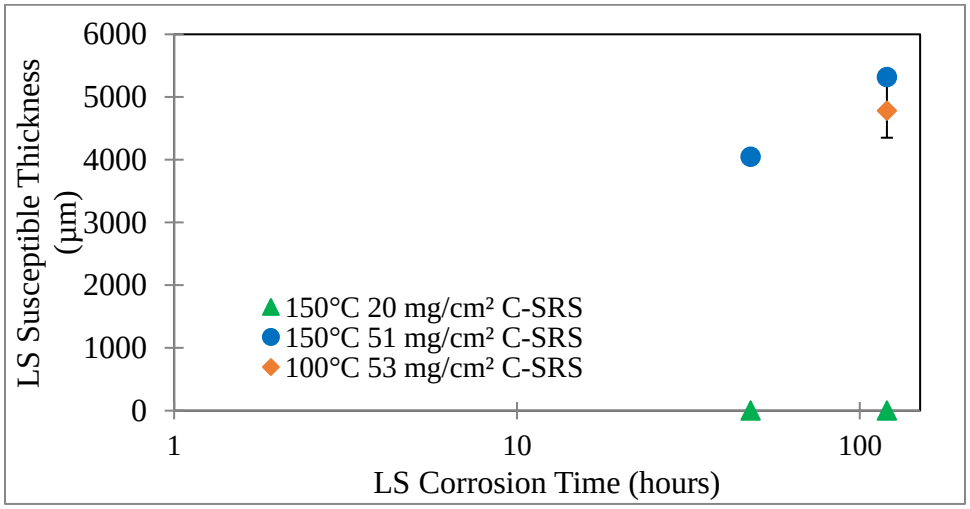

Figure 5-8 Alcoa 5083-H116 sensitized at 100°C and 150°C, exposed on the LS surface to the accelerated corrosion environment. The corrosion susceptible thickness of the C-SRS structure values is shown versus corrosion time.

5.5 Conclusions

Alcoa 5083-H116 was sensitized at 100°C for up to 1,500 hours and at 150°C for 2,000 hours to obtain DoS that were corrosion resistant and corrosion susceptible. The influence of sensitization on the surface orientation microstructure changes was investigated via etching. Along with microstructure analysis, subsequent corrosion tests were conducted on small-scale and tension dog bones samples with emphasis on LT and LS surface orientation corrosion damage. New conclusions resulting from this research are as follows:

- The impact of sensitization on Alcoa 5083-H116 microstructure, specifically α grain size was quantified via etching. Observations on the LT surface indicated that sensitization at 100°C and 150°C caused recrystallization of the Alcoa 5083-H116. The AR 5083-H116 (with DoS 3 mg/cm²) had a LT surface α grain size of 89 µm. After 304 hours of sensitization at 100°C and 25 hours at 150°C, α grain sizes significantly decreased to 69 µm and 66 µm, respectively. A DoS of 61 mg/cm² from 150°C sensitization for 1000 hours corresponded to the smallest grain size of 55 µm.

- Post-etching measurements on the LS surface indicated that no significant changes in α grain size occurred. However, bands were visible to the naked eye both before and after etching. This observation is somewhat consistent with that seen by Wei et al. who found that 5083 samples exhibited differences in grain sizes through the thickness of the plate, with the outside being corrosion susceptible and recrystallized, while the middle was corrosion resistant and non-recrystallized [47].

- The influence of sensitization on surface orientation dependent corrosion damage was quantified in terms of exfoliation thickness loss and IGC penetration depth for cold-rolled and sensitized Alcoa 5083-H116. This study characterized the damage in terms of exfoliation damage and penetration damage for the LT and LS surfaces of small-scale and mechanical test dog bones. The LT surface exhibited a parallel exfoliation thickness loss and subsequent parallel IGC damage. The LS surface corrosion damage had a perpendicular thickness loss and subsequent perpendicular IGC damage.

- At a corrosion susceptible DoS (>51 mg/cm²) resulting from a sensitization temperature 150°C, the extent of LS surface corrosion damage was greater than LT surface corrosion

damage. After 120 hours of accelerated corrosion exposure, the LT exfoliation thickness loss was significant for DoS >51 mg/cm² for samples sensitized at 150°C. However, when IGC susceptible samples with a DoS 53 mg/cm² resulting from 100°C sensitization were exposed to the corrosion environment, pitting occurred at -0.77 V_{SCE}. At -0.755 V_{SCE}, an exfoliation LT thickness loss was present, but was much smaller than the LT thickness loss at the same DoS resulting from the 150°C sensitization. This result indicates that DoS alone is not sufficient to describe susceptibility to corrosion damage.

6 Room Temperature Mechanical Properties of Sensitized and Corroded 5083-H116

6.1 Sensitization and Sensitization Temperature Effect on Tensile Properties

Few studies have examined the effects of sensitization and sensitization temperature on subsequent room temperature mechanical properties. (Some results are available [43], [49], [87].) To provide additional data, samples were sensitized at various times at 100°C and 150°C as summarized in Figure 5-1. Sensitized dog bones were tested at a constant displacement rate of 5 mm/minute with a 25.4 mm gauge length extensometer in an Instron 5984, illustrated in Figure 4-12. The expectation based on the previous studies was that AA5083-H116 sensitized at 150°C would, at certain exposure times, experience recovery and some recrystallization of α grains, while material sensitized at 100°C would experience only recovery even at the longest exposure times. Any significance should be attributed to the change in β precipitation along the GB, since recovery was expected to occur in the samples sensitized at 304 and 1084 hours. The other expectation from previous studies was that at certain exposure times, AA5083-H116 sensitized at 150°C would experience both recovery and partial recrystallization of α grains. If recrystallization occurred, then the mechanical property degradation can be attributed to both α grain recrystallization, along with β precipitation. Figure 6-1, 6-2, and 6-3 show the mechanical property results of solely sensitized Alcoa 5083-H116 at 100°C and 150°C.

Figure 6-1 through Figure 6-3 show the results of solely sensitized Alcoa 5083-H116 at 100°C and 150°C in terms of 0.2% offset yield strength (MPa), ultimate tensile strength (MPa), elastic modulus (GPa), and % reduction in area (%), respectively. Based upon Figure 6-1, it can be gathered that the sensitization process at 100°C lowered the 0.2% yield strength from the AR 5083-H116 state by from 276 MPa to 259 MPa and 256 MPa (304 hours and 1084 hours in the sensitization chamber). The degradation from this sensitization temperature was expected to be solely due to β phase precipitation; however, a reduction in α grain size occurred in 5083-H116 sensitized at 100°C. For the higher sensitization temperature of 150°C, Alcoa 5083-H116 demonstrated a larger drop in yield strength even at the corrosion resistant DoS of 20 mg/cm² (25 hours of sensitization exposure). This can be correlated to the possible α grain size changes from partial recrystallization presented in Table 5-1, since the corrosion resistant DoS has discontinuous β along GB. The corrosion susceptible DoS of 51 mg/cm² and > 61 mg/cm² sensitized at 150°C

saw a further decrease in yield strength due to the recrystallization from the sensitization temperature along continuous or corrosion susceptible β phase precipitation along GB. Also, the higher 150°C sensitization temperature caused larger drops in yield strength than the 100°C sensitization process.

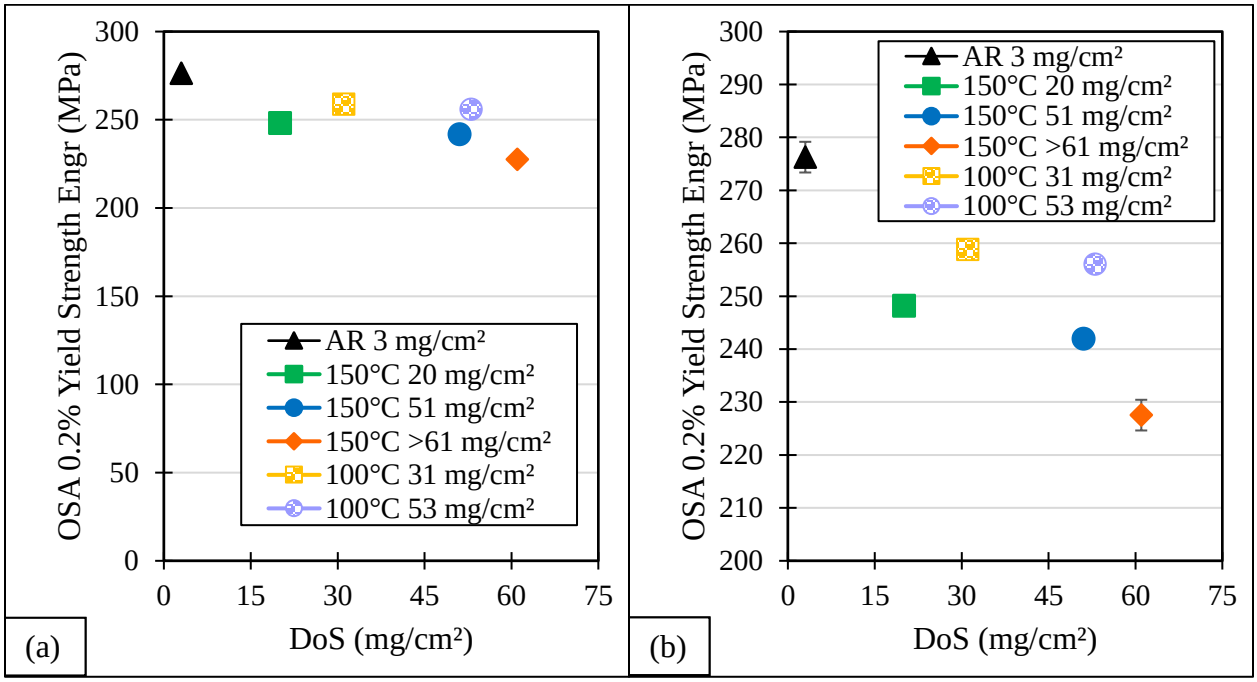

Figure 6-1 The OSA 0.2% offset yield strength for AA5083-H116 sensitized at 100°C and 150°C for different amounts of time, (a) showing the full scale and (b) showing an enlarged version to present standard deviation values. Standard deviation for all data shown was less than ±2 MPa in most cases and was ±2.9 MPa for DoS 3 mg/cm² and the highest DoS >61 mg/cm².

The OSA ultimate tensile strength (UTS) is shown in Figure 6-2 for the sensitized states of Alcoa 5083-H116. Unlike the 0.2% yield strength degradation due to recovery, partial recrystallization, and/or β precipitation, the UTS is not controlled by the same mechanisms. The 100°C sensitization exposure caused the UTS to increase slightly even at the most extreme sensitization exposure time of 1,084 hours or DoS 53 mg/cm² to 360 MPa from the AR state UTS 355 MPa. However, at the 150°C the corrosion resistant DoS 20 mg/cm² and corrosion susceptible 51 mg/cm², both have smaller grain sizes than the AR 3 mg/cm² state, along with larger amounts of β precipitation. At the harshest sensitization environment of 150°C and 1,000 hours, DoS >61 mg/cm² had a distinct lower UTS than the AR and other 150°C sensitized states at UTS 342 MPa. This signifies the σ grain size reduction due to partial recrystallization eventually outweighed the effects β phase dissolution into the GB in this condition.

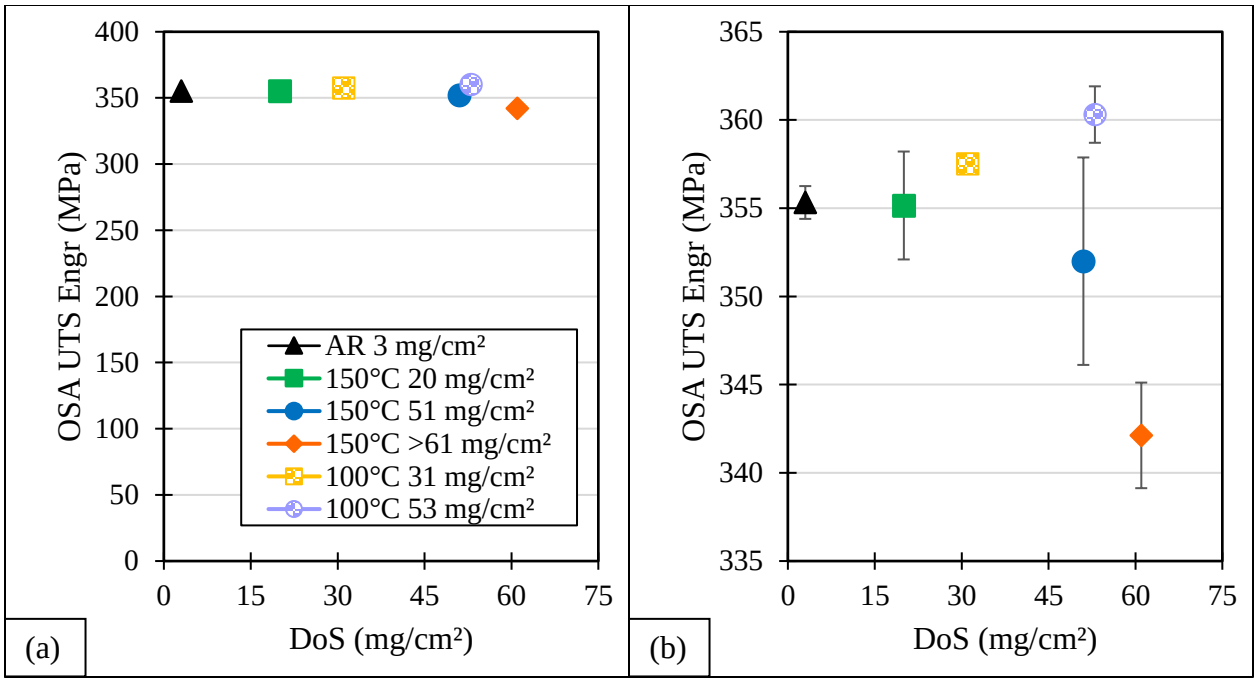

Figure 6-2 The OSA UTSs are presented for AA5083-H116 sensitized at 100°C and 150°C for different amounts of time, (a) showing the full scale and (b) showing a zoomed in version to display standard deviation values. All standard deviations are presented, with the 100°C 31 mg/cm² having $\sigma = \pm 0.4$ MPa.

Figure 6-3 contains the results of the OSA elastic moduli and percent reduction in area for all sensitized states of 5083-H116 mechanically tested at room temperature tension conditions. The AR 5083-H116 state had an elastic modulus of 74 GPa. At 100°C, the elastic modulus dropped with increasing sensitization time. However, accounting for standard deviation in the data, the AR and 31 mg/cm² are the same in terms of E, while 53 mg/cm² was significantly lower at 63 GPa. For percent area reduction, the AR and sensitized 5083-H116 at 100°C were significantly different, with AR being at 15.39 %RA, and 100°C DoS 31 mg/cm² and 53 mg/cm² being at 14.12 %RA and 14.49 %RA respectively. The AR and heavily sensitized DoS of 51 mg/cm² and >61 mg/cm² sensitized at 150°C reacted the same in terms of elastic moduli, while the elastic modulus was lower for the IGC resistant DoS 20 mg/cm². The percent area reduction for the higher sensitization temperature of 150°C at IGC susceptible DoS >61 mg/cm² was greater than that for the AR state of the material.

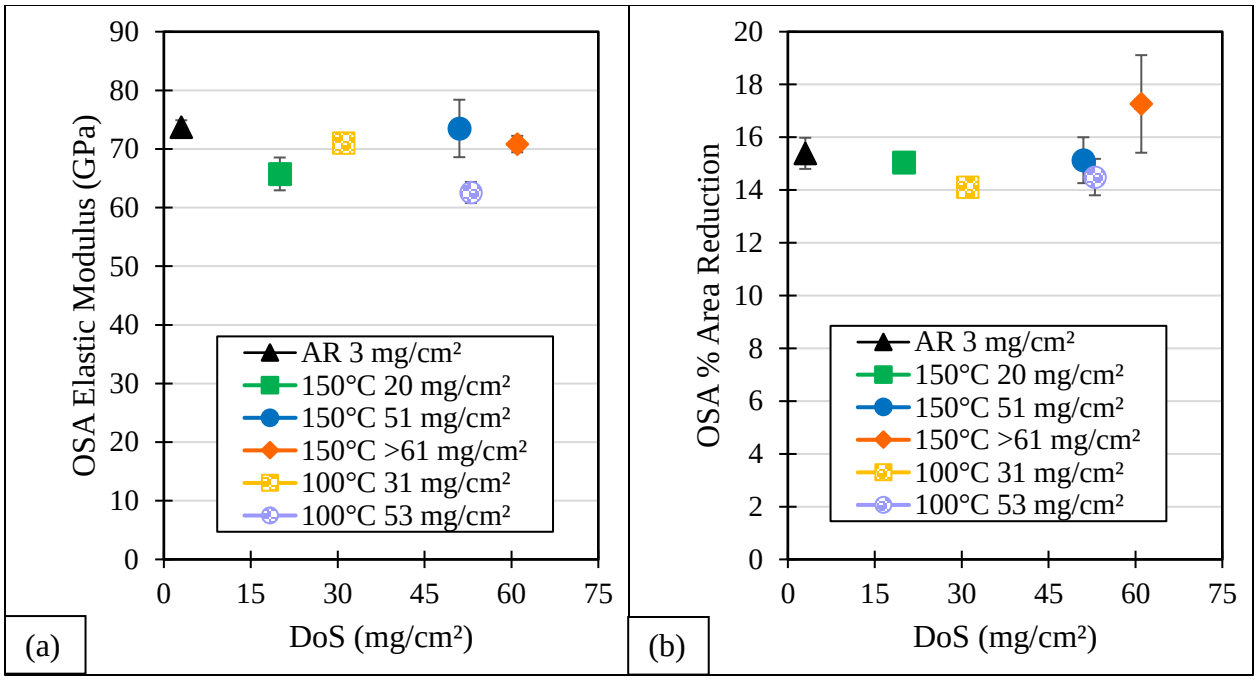

Figure 6-3 The OSA elasticity measurements for AA5083-H116 sensitized at 100°C and 150°C for different amounts of time, (a) Young's modulus, E and (b) percent area reduction.

6.2 OSA vs. PCSA properties

6.2.1 Exfoliation Thickness Loss

Upon completing the accelerated corrosion testing of the LT or LS surfaces, sensitized Alcoa 5083-H116 dog bone samples were cleaned with water and ethanol to prevent subsequent corrosion damage. Samples were then brushed off to remove any loose or exfoliated grains. Digital calipers were then used to measure the post-corrosion LT thickness loss or post-corrosion LS C-SRS, which was, in turn, used to help calculate the PCSA. This data is explained through Figure 5-5 and Figure 5-6, respectively.

6.2.2 Penetration Damage Quantified

Along with these caliper measurements, samples were cross-sectioned to obtain relative penetration depths for the corroded LT and LS surface orientations for different conditions (based upon sample availability). These results are characterized and quantified in Figure 5-7 and Figure 5-8. Some of the PCSA values contain the PD measurements when extra samples for cross-sectioning were available; in other cases assumptions were made based on the DoS values closest to available measurements.

6.3 Sensitization and Corrosion Effect on Tensile Properties

Similar to the OSA graphs of purely sensitized Alcoa 5083-H116 presented in Figure 6-1, Figure 6-2, and Figure 6-3, the OSA mechanical properties of sensitized and corroded samples are presented in the following figures. Figure 6-4 provides the OSA 0.2% offset yield strength (engineering) values for AR, sensitized, and corrosion damaged 5083-H116. For material sensitized at 150°C, the corrosion resistant DoS 20 mg/cm² remains roughly at the same 0.2% offset yield strength value even after 120 hours of LT or LS corrosion damage. Under the OSA assumption, the 0.2% offset yield strength drops for corrosion susceptible sensitization levels of 51 mg/cm² and >61 mg/cm², with the LS corrosion damage causing more degradation than the LT corrosion damage. When material sensitized at 100°C was corroded, a drop in 0.2% offset yield strength was barely discernible at -0.77 V_{SCE} at the IGC susceptible DoS 51 mg/cm². When there was a different potential of -0.755 V_{SCE}, more corrosion damage took place on the LT and LS surfaces, and slight drops in 0.2% offset yield strength were noticeable and significantly different with statistical analysis. Appendix B contains the OSA and PCSA mechanical properties, with standard deviations for the remaining figures displayed in Chapter 6 for data analysis purposes. Table B-1 contains the OSA 0.2% offset yield strength average among replicates and standard deviation values for all test conditions.

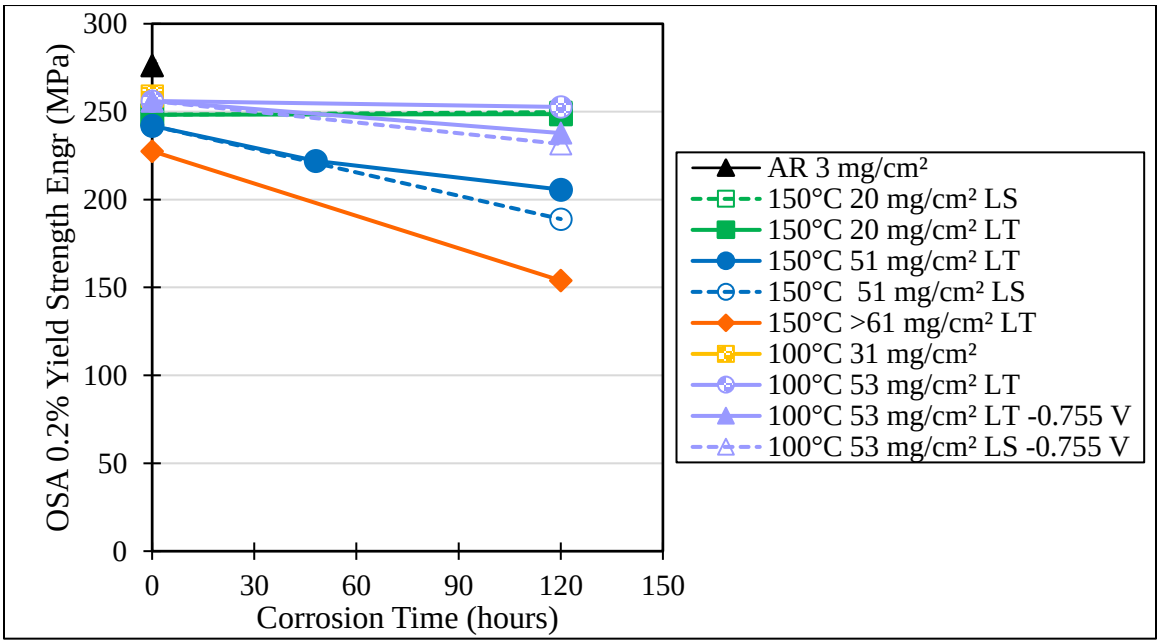

Figure 6-4 The OSA 0.2% offset yield strengths for AA5083-H116 sensitized at 100°C and 150°C and corroded for up to 120 hours.

Figure 6-5 shows the UTS (engineering) values for AR, sensitized, and corrosion damaged 5083-H116. The difference in the UTS and 0.2% offset yield strength changes are noticeable, with only corrosion damage lowering the UTS values from the AR and solely sensitized state of the material. The corrosion resistant DoS of 20 mg/cm² from the 150°C sensitization exposure maintained its UTS properties after 120 hours of LT or LS corrosion damage. For the corrosion susceptible DoS 51 mg/cm² and > 61 mg/cm² sensitized at 150°C, under the OSA assumption, the UTS drops with the presence of LT surface corrosion damage, while the LS surface corrosion damage was more detrimental in degrading the UTS at 51 mg/cm². When material sensitized at 100°C was corroded, a drop in UTS was not present for the -0.77 V_{SCE} corrosion condition. When there was a different potential of -0.755 V_{SCE}, more corrosion damage took place on the LT and LS surfaces and slight drops in UTS were noticeable, with the LS surface damage causing more UTS degradation yet again. Table B-2 contains the OSA ultimate tensile strength average among replicates and standard deviation values for all test conditions.

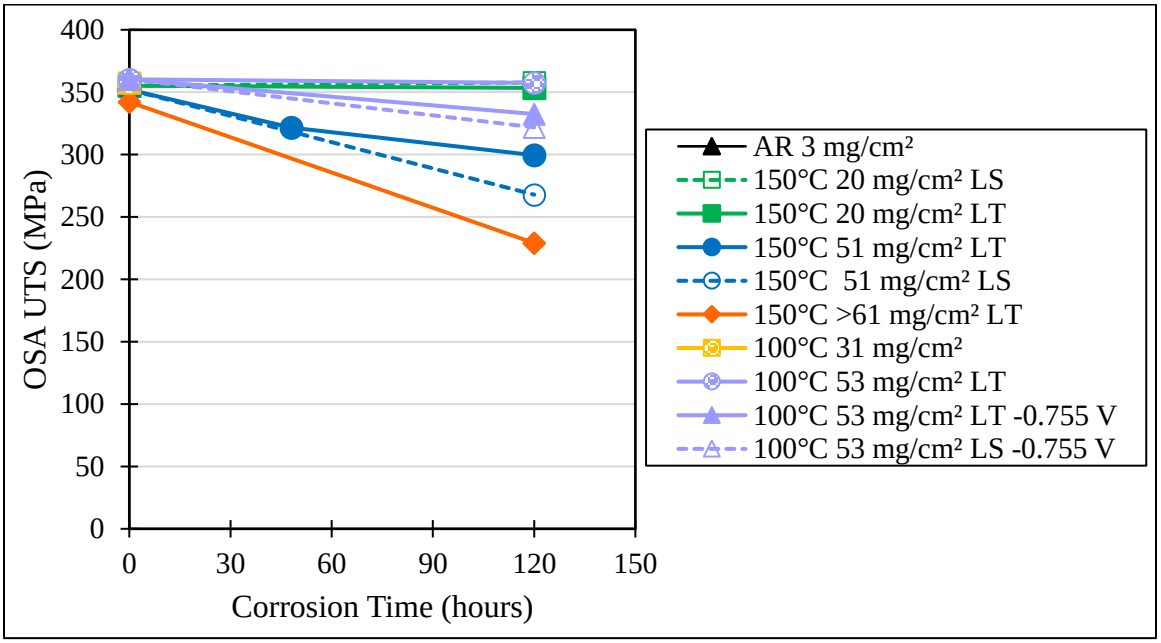

Figure 6-5 The OSA UTSs for AA5083-H116 sensitized at 100°C and 150°C and corroded for up to 120 hours.

Figure 6-6 (a) presents the elastic moduli, and Figure 6-6 (b) provides the percent reduction area properties under the OSA assumption for the various states of the 5083-H116 alloy, while Table B-3 and Table B-4 contain mean and standard deviation values for each condition. For material sensitized at 150°C, the corrosion resistant DoS 20 mg/cm² maintained its elastic moduli for LT

corrosion damage and slightly increased with LS corrosion damage. For the LT corrosion damage of DoS 51 mg/cm², the elastic modulus dropped slightly, while the LS corrosion damage of DoS 51 mg/cm² caused a drop in E by >20 GPa. The highest DoS >61 mg/cm² with LT corrosion damage also had a drop in E by >20 GPa; however, only two samples were available for testing at this condition. When material was sensitized at 100°C, DoS 53 mg/cm² elastic moduli values for both LT corrosion damage exposures remained constant. However, for the LS corrosion damage of the same DoS, the elastic modulus decreased.

Under the OSA assumption, the material sensitized at 150°C reacted differently across the board in terms of percent area reduction (%RA). The corrosion resistant DoS 20 mg/cm² had roughly the same %RA for the LS corrosion damage, while the LT corrosion damage caused a larger %RA. For LS corrosion damage of 51 mg/cm², the percent area reduction decreased (this does not include IGC penetration depth damage), while the LT corrosion caused an increase in %RA. A DoS of >61mg/cm² caused a large %RA degradation also. When the material was sensitized at 100°C, both LT corrosion damage exposures caused the %RA to stay the same. However, the LS corrosion damage (which does not include IGC penetration depth damage) had a lower %RA.

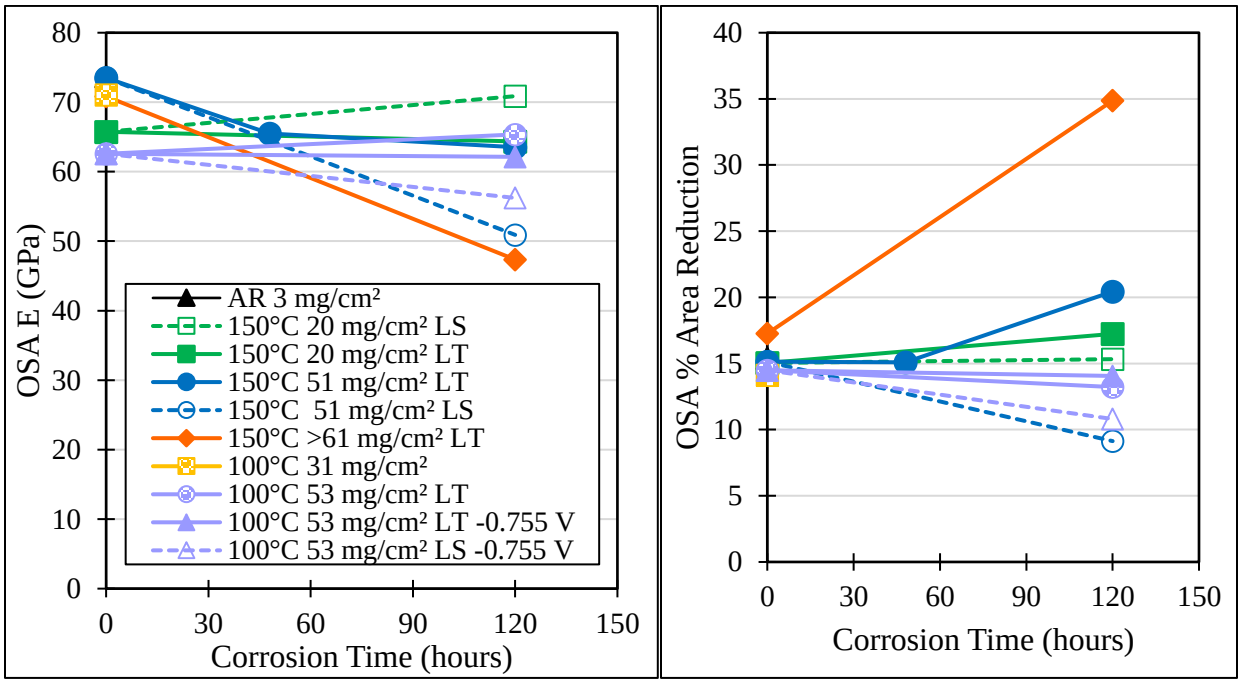

Figure 6-6 The OSA elasticity measurements for AA5083-H116 sensitized at 100°C and 150°C and corroded for up to 120 hours, (a) Young's Modulus, E and (b) % area reduction.

While the OSA assumption is useful in characterizing the effects of corrosion damage on sensitized Alcoa 5083-H116, it does not fully capture the corrosion damage present prior to tension testing. Figure 6-7 displays the PCSA 0.2% offset yield strength mechanical properties of the two sensitization exposures, along with corrosion damage present on corrosion susceptible DoS. Table B-5 helps provide better insight so the amount of 0.2% yield strength degradation. The AR material had a YS of roughly 276 MPa, while increasing DoS led to a degradation in YS at both sensitization temperatures. For the 100°C sensitization exposure, the LT corrosion at -0.77 V_{SCE} caused minimal degradation to 0.2% offset yield strength; however, corrosion at -0.755 V_{SCE} caused a degradation of ~5 MPa for both LT and LS corrosion. The 0.2% offset yield strength slightly increased for 20 mg/cm² from the 150°C sensitization with LT or LS surface corrosion. At DoS 51 mg/cm², the LT had >5 MPa drop in YS after 120 hours of corrosion exposure, while the LS surface corrosion caused a decrease of ~35 MPa. The corrosion susceptible DoS >61 mg/cm² dropped nearly 30 MPa and had the lowest YS of all sensitization and corrosion scenarios. Table B-5 shows these 0.2% offset yield strength results along with their standard deviation values for each test condition.

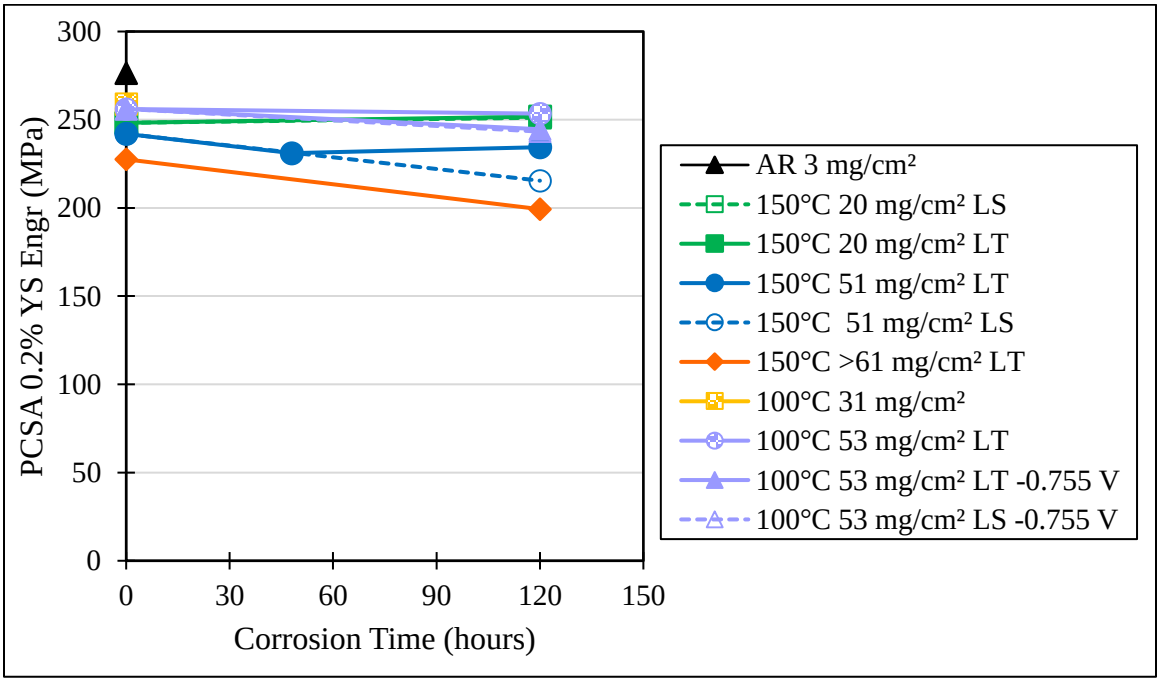

Figure 6-7 The PCSA 0.2% offset yield strengths for AA5083-H116 sensitized at 100°C and 150°C and corroded for up to 120 hours.

Slightly different trends were noticeable in Figure 6-8 for the PCSA UTS of the tested Alcoa 5083-H116. As presented in Figure 6-2, the UTS of solely sensitized material barely changes from the

AR state of Alcoa 5083-H116. For the 100°C sensitization exposure, the LT corrosion at -0.77 V_{SCE} caused minimal degradation to UTS; however, corrosion at -0.755 V_{SCE} caused a degradation of ~18 MPa for both LT and LS corrosion. The UTS slightly increased for 20 mg/cm² from the 150°C sensitization with LT or LS surface corrosion. At DoS 51 mg/cm², the LT had ~10 MPa drop in UTS after 120 hours of corrosion exposure, while the LS surface corrosion caused a decrease of ~47 MPa. The corrosion susceptible DoS >61 mg/cm² dropped ~45 MPa in PCSA UTS. Table B-6 shows these UTS results along with their standard deviation values for each test condition.

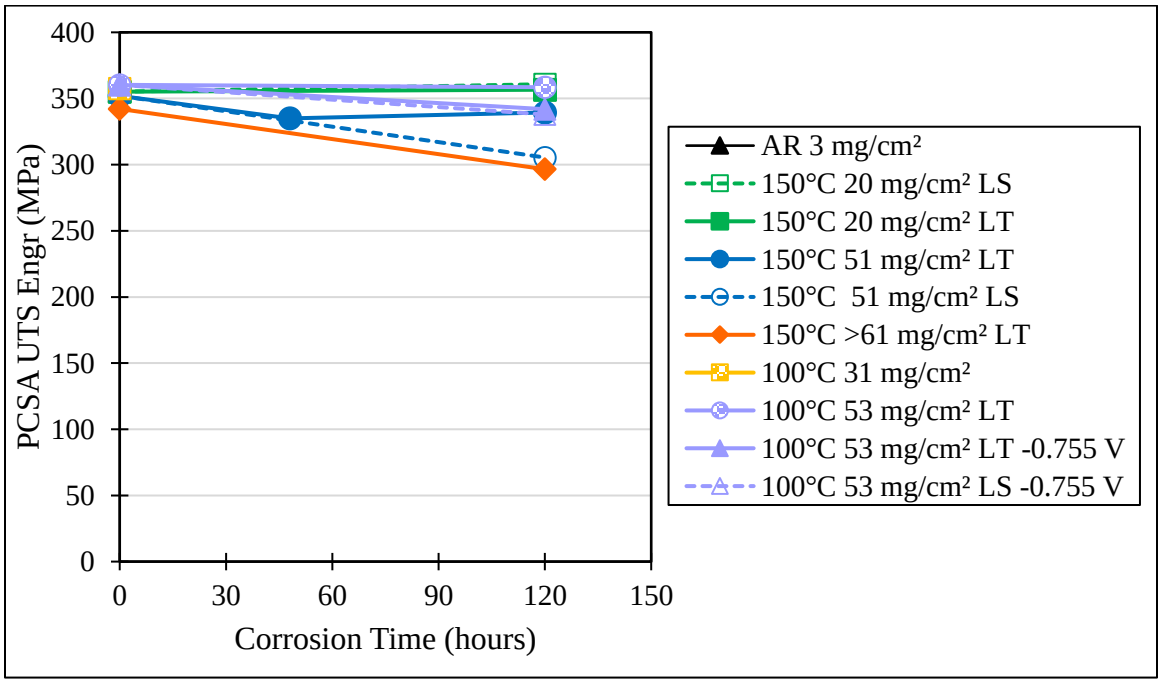

Figure 6-8 The PCSA UTSs for AA5083-H116 sensitized at 100°C and 150°C and corroded for up to 120 hours.

Figure 6-9 demonstrates the elastic moduli of the sensitized and corroded Alcoa 5083-H116 under the PCSA assumption. When material was sensitized at 100°C, DoS 53 mg/cm² PCSA elastic moduli values for both LT corrosion damage exposures increased slightly. However, for the LS corrosion damage of the same DoS, the elastic modulus decreased slightly. Once accounting for standard deviation, the elastic moduli were the same after corrosion damage was present. For material sensitized at 150°C, the corrosion resistant DoS maintained its PCSA elastic moduli for LT corrosion damage and increased with LS corrosion damage. For the LT corrosion damage of DoS 51 mg/cm², the elastic modulus dropped slightly after 120 hours of corrosion, while the LS

corrosion damage caused a drop in E by ~15 GPa. The highest DoS >61 mg² with LT corrosion damage also had a drop in E by ~10 GPa. Table B-7 shows these elastic moduli results along with their standard deviation values for each test condition.

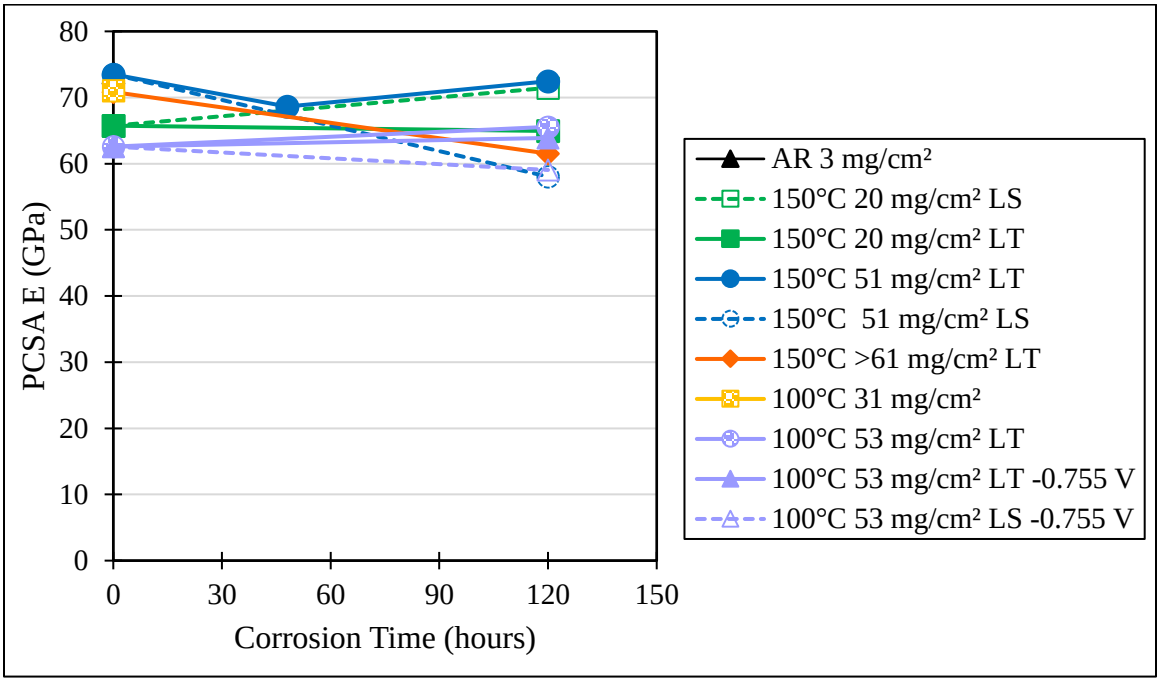

Figure 6-9 The PCSA Young's Modulus for AA5083-H116 sensitized at 100°C and 150°C and corroded for up to 120 hours.

Under the PCSA assumption, the material sensitized at 150°C reacted differently based on sensitization level and corrosion damage in terms of percent area reduction as shown in Figure 6-10. For material sensitized at 150°C, the corrosion resistant DoS 20 mg/cm² had roughly the same PCSA % area reduction for the LS corrosion damage, while the LT corrosion damage caused a larger percent area reduction. For LS corrosion damage of 51 mg/cm², the PCSA %RA decreased (this does not include IGC penetration depth damage), while the LT corrosion caused a decrease in PCSA %RA also. A DoS of >61 mg/cm² caused a large PCSA %RA degradation also. When the material was sensitized at 100°C, both LT corrosion damage exposures caused the PCSA %RA to decrease slightly. However, the LS corrosion damage (which does not include IGC penetration depth damage) had a higher degradation in PCSA %RA. Table B-8 shows these %RA results along with their standard deviation values for each test condition.

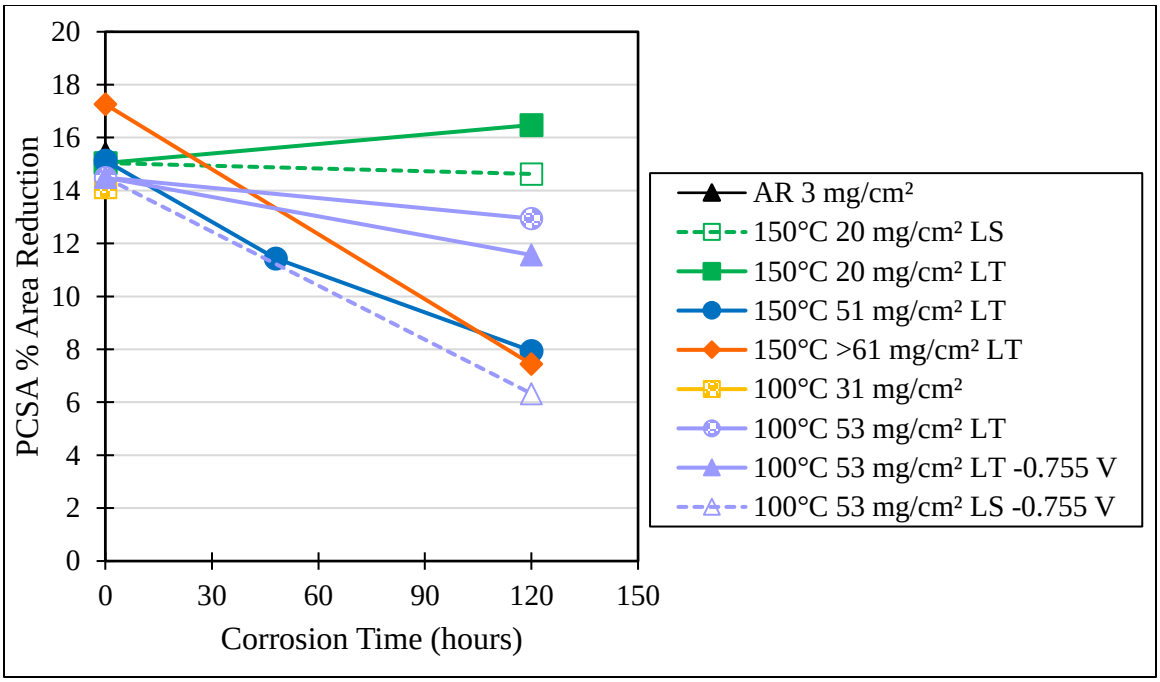

Figure 6-10 The PCSA percent area reduction for AA5083-H116 sensitized at 100°C and 150°C and corroded for up to 120 hours.

6.4 Conclusions

Alcoa 5083-H116 was sensitized at two temperatures and exposed to accelerated corrosion environment. After the corrosion exposure, corrosion damage was quantified as thickness loss and penetration depth for each corroded surface (LT or LS). Room temperature tension tests were then performed on both sensitized and sensitized and corroded 5083-H116. Results were quantified in terms of 0.2% offset YS, UTS, elastic moduli, and percent area reduction. New conclusions gathered form this research are as follows:

- The influence of sensitization on YS and UTS for Alcoa 5083-H116 was quantified. Significant differences were seen in the YS of AR Alcoa 5083-H116 and sensitized Alcoa 5083-H116 for all sensitization combinations. With increasing sensitization time and temperature of 100°C and 150°C, the YS was reduced. However, the UTS of material sensitized at 100°C increased slightly from the AR state, while the UTS from the sensitization temperature at 150°C decreased at the longest sensitization time.

- The use of PCSA instead of OSA better quantified the influence of corrosion damage on these room temperature tension properties. The OSA assumption meant no corrosion damage was considered for the cross-section area during mechanical testing. However, the PCSA has an assumption of exfoliation thickness loss and penetration depth from corrosion damage, which more accurately depicted the mechanical response of the material.

- For IGC susceptible material sensitized at 150°C, LT and LS corrosion damage both reduced the YS and UTS greater than just sensitization, with the LS corrosion damage being more detrimental. There was no discernible difference on YS and UTS for IGC materials sensitized at 100°C.

7 Elevated Temperature Creep Properties of Sensitized and Corroded 5083-H116

This chapter was adapted from

The Influence of Sensitization and Corrosion Creep of 5083-H116

R.J. Mills, B.Y. Lattimer, S.W. Case, and A.P. Mouritz,

Corrosion. Science. Vol. 143, October, pp. 1–9, 2018.

7.1 Creep Response of Sensitized and Corrosion AA5083-H116

7.1.1 200°C Creep

Creep tests were conducted at 200°C with an applied stress of 120 MPa; the creep strain results are presented in Figure 7-1. Three repeats were performed for the AR state (DoS = 3 mg/cm²) and low sensitization state (DoS = 20 mg/cm²). The measured average rupture times were ~5465 s for the AR state versus a longer time of ~ 6,662 s for the low sensitization state. The rupture strains were 0.58 (3 mg/cm²) and 0.54 (20 mg/cm²). The steady-state strain rate, $\dot{\varepsilon}_{II}$, determined for the AR state, was 3.87×10^{-5} s^{-1}, while the low sensitization state was 3.52×10^{-5} s^{-1}. None of these differences were found to be statistically significant at $\alpha = 0.05$.

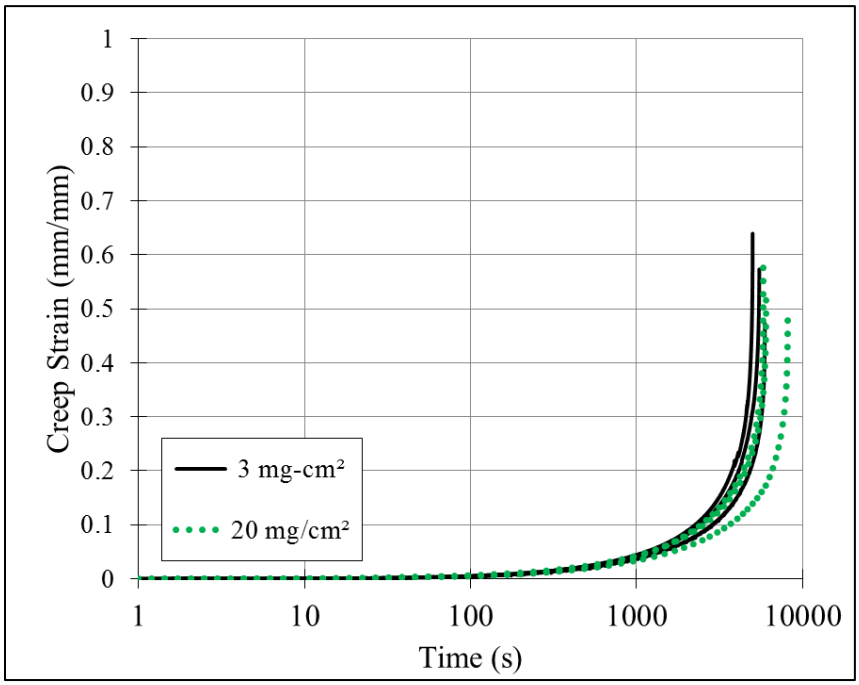

Figure 7-1. Creep at 200°C for AR and corrosion resistant DoS states of 5083-H116 at 120 MPa [98].

7.1.2 300°C Creep

Based on previous studies, 5083-H116 was expected to partially recrystallize after 600 s (10 min) of exposure to 300°C, leading to a more equiaxed grain structure [107]. Figure 7-2 summarizes the response of the AR, sensitized, and sensitized with corrosion damaged 5083-H116 to 300°C at 35 MPa and 50 MPa. For creep at this stress/temperature combination, the corroded material experienced failure at ~2088 s, while the same DoS level without corrosion damage failed at ~6091 s as presented in Figure 7-2 (a). The rupture times of the AR and sensitized states were significantly different, but no trend was found with the sensitization effect increasing or reducing the creep rupture time. For Figure 7-2 (a), both the AR and sensitized material exhibited approximately 3600 s of steady-state creep, followed by the tertiary creep response. Rupture strains reacted similarly as the rupture times for AR and sensitized material versus the corrosion damage of the sensitized material. A test of means for the $\dot{\varepsilon}_{II}$ indicated that all sensitized but not corroded 5083-H116 samples behaved the same. For 35 MPa at 300°C, the rupture time, rupture strain, and the secondary creep rates of the corroded 51 mg/cm² were lower statistically from the AR and sensitized states' performance. The corrosion damage caused an increase in magnitude of ~3.5 for $\dot{\varepsilon}_{II}$, with a value of 1.44×10^{-4} s^{-1} compared to the sensitized state of 4.18×10^{-5} s^{-1}. For any statistical significance, $\alpha = 0.05$ was used for all testing.

Figure 7-2 (b) contains the results of the creep tests at 50 MPa and 300°C. For sensitized material of < 51 mg/cm², the rupture time was ~1,300 s, while the 61 mg/cm² ruptured closed to ~970 s. The standard deviation of the rupture time was higher once again for corrosion susceptible DoS versus the AR and corrosion resistant DoS. The creep rupture strain and secondary creep rates of all sensitized material reacted in similar fashion to the AR 5083-H116 material in this test condition. With the inclusion of corrosion damage on sensitized material, a reduction in creep rupture time and rupture strain was noted, along with an increase in secondary creep rate. The corroded DoS material failed at 650-775 s, which is approximately half of the solely sensitized material (1300 s). The standard deviation of the rupture time of the corroded material was also higher than the AR and IGC resistant DoS states. The creep rupture strain dropped from 0.78 to 0.68 (when comparing the average of AR plus sensitization against sensitization plus corrosion). With the corrosion damage of the sensitized state, the material had a secondary creep rate of ~2.58×10^{-4} s^{-1}, which was ~1.6 times faster than the sensitized material secondary creep rate.

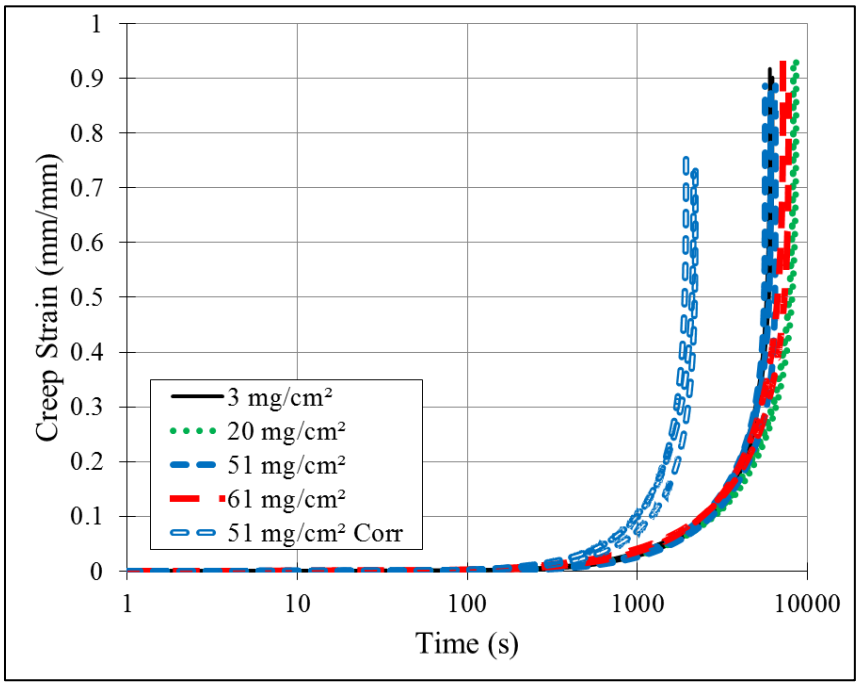

(a)

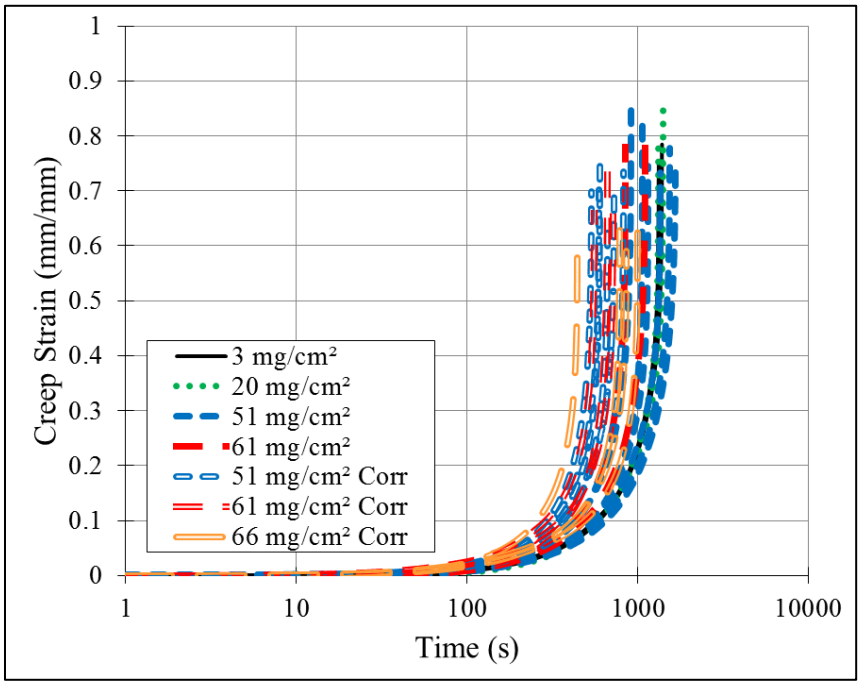

(b)

Figure 7-2 Creep at 300°C for AR, corrosion resistant, corrosion susceptible, and corrosion damaged DoS levels of AA5083-H116 at (a) 35 MPa and (b) 50 MPa [98].

7.1.3 400°C Creep

The highest temperature testing during this creep study was 400°C, with a low stress level of 13 MPa and a high stress level of 18 MPa, which are provided in Figure 7-3 (a) and (b). Based on the studies by Allen [101], Summers, et al. [101], and Chen [107], [108], full recrystallization is expected to occur at 400ºC after ten minutes of elevated temperature exposure. This means that the microstructure is closer to an equiaxed structure for all DoS. In Figure 7-3 (a), the 3 mg/cm^2 and 20 mg/cm^2 material reacted the same with rupture times close to 3000 s, while the corroded DoS of 51 mg/cm^2 and 61 mg/cm^2 failed one-third faster (2131 s and 2033 s) compared to the corrosion resistant DoS samples. At this stress/temperature combination, the standard deviation of rupture time was lower for the sensitized and corroded material when compared to the AR state. In terms of rupture strain, the material reacted similarly. For the secondary creep rate, the AR, corrosion resistant and corrosion damaged states of the material all had similar values close to 9.50×10^{-5} s^{-1} and were statistically the same. In Figure 7-3 (b) the AR and corrosion damaged 61 mg/cm^2 states of the material were creep tested at the same temperature and higher stress. The AR material reacted similar to the corroded 61 mg/cm^2 in terms of creep rupture time, secondary creep rate, and creep rupture strain. The higher DoS also had a higher standard deviation for the rupture time.

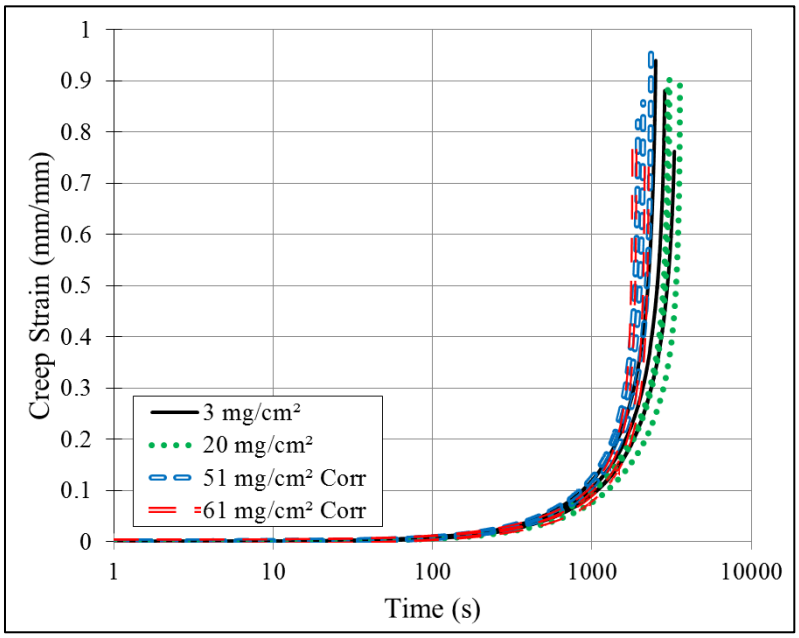

(a)

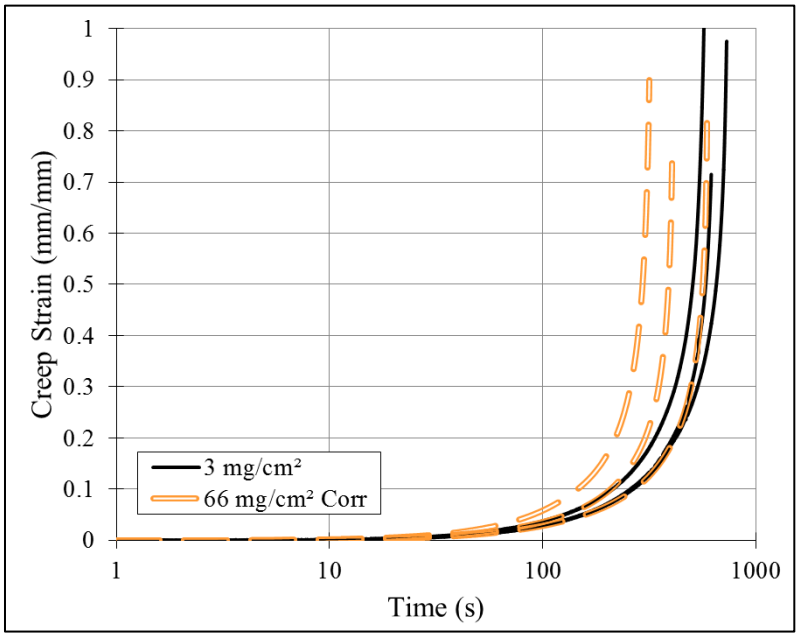

(b)

Figure 7-3 Creep at 400°C for AR, corrosion resistant, and corrosion damaged DoS levels at (a) 13 MPa and (b) 18 MPa [98].

7.2 Evaluation of Creep Experiments with Larson-Miller Parameters

Figure 7-4 illustrates the LMP versus stress for the sensitized and sensitized and corroded states of 5083-H116. The OSA assumption is made in Figure 7-4 (a), suggesting a difference in the behavior of sensitized versus sensitized and corroded 5083-H116. However, if the post-corrosion

(PCSA) assumption is used, the stress values are expressed accurately, and the LMPs seem to be similar in all three states of the alloy; AR, sensitized, and sensitized plus corroded material are illustrated in Figure 7-4 (b).

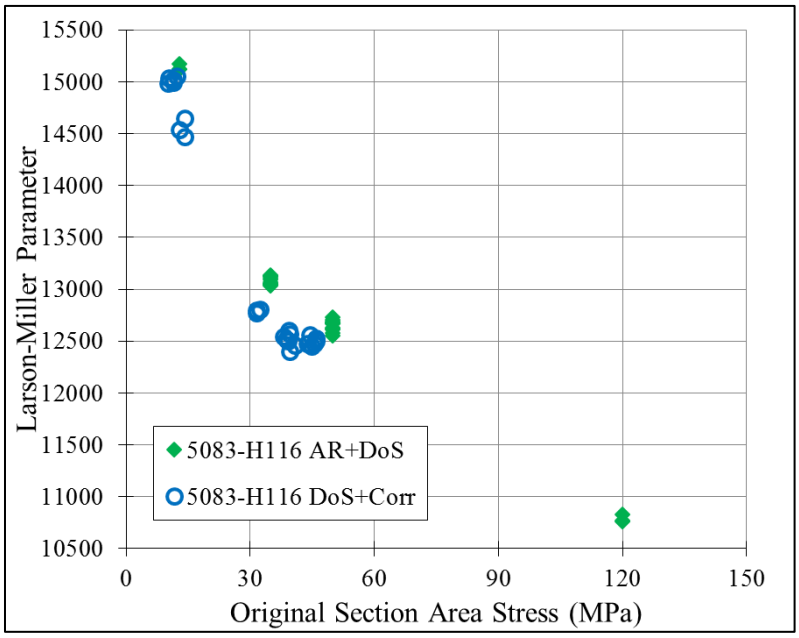

(a)

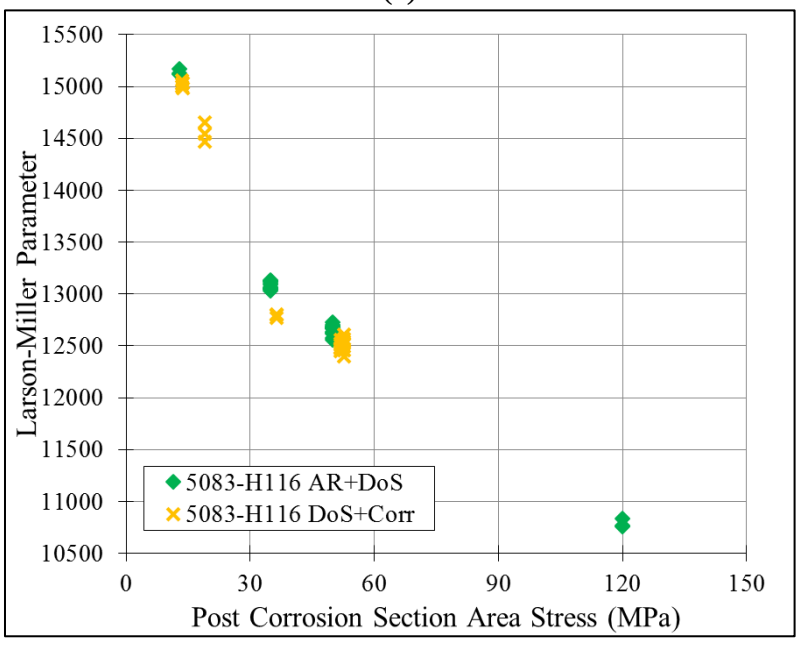

(b)

Figure 7-4 LMP for 150°C sensitized and 150°C sensitized plus corroded 5083-H116 at various creep conditions for (a) OSA Stress and (b) PCSA Stress assumptions [98].

After using the PCSA for the creep data performed in this study, a new set of LMP values were generated along with the addition of data from studies by Allen and Kaufman. Figure 7-5 contains the new LMP_{S+C} fitting curve including data from Kaufman's AR 5083-H321 [105], Allen's AR 5083-H116 [101], and the new AR, sensitized 5083-H116, and sensitized 5083-H116 with LT corrosion damage from equation 4.8. The values of the LMP fitting equation are listed in Table 7-1 for a combination of all four data sets in the data fit in Figure 7-5. The SSE, R^2, and RMSE values can be seen along with the LMP_{S+C} fitting parameters in Table 7-1. *A key finding from this work is that if the corrosion effects on net section stress are accounted for, there is no significant difference in LMP of AR, sensitized, or sensitized and corroded 5083-H116.*

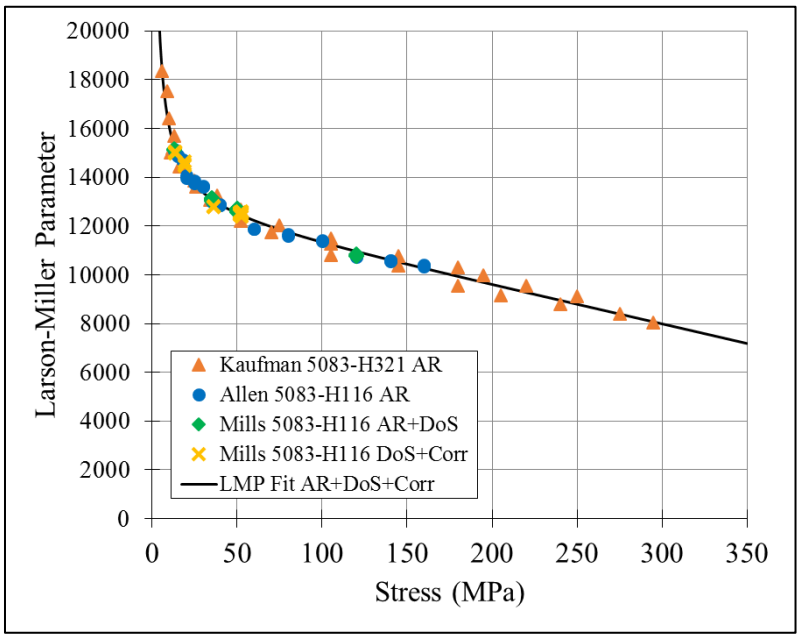

Figure 7-5 LMP_{S+C} Fitting including AR+DoS+Corr states of Alcoa 5083-H116 [98].

Table 7-1 LMP_{S+C} fitting parameters for AR+DoS+Corr states of Alcoa 5083-H116 [98].

Parameter	Value
D (K)	-1715
E (-)	-17.89
F (1/MPa)	14.52
n (-)	0.05225
G (K)	12390
SSE	5.75×10^6
R^2	0.9852
RMSE	220.7

7.2.1 Sensitization Temperature Influence on Creep Response

Most of the creep testing occurred on Alcoa 5083-H116 sensitized at 150°C; however, the effects of sensitization temperature were investigated also. Figure 7-6 contains LMP values of material sensitized at 100°C, with DoS 53 mg/cm², and corroded on the LT surfaces for 120 hours at -0.755 V_{SCE}. This data suggests that material sensitized at 100°C along with LT corrosion damage can be accounted for by the fit data from Table 7-1. This means that the 100°C and 150°C sensitized material react similarly in all creep conditions tested in this study.

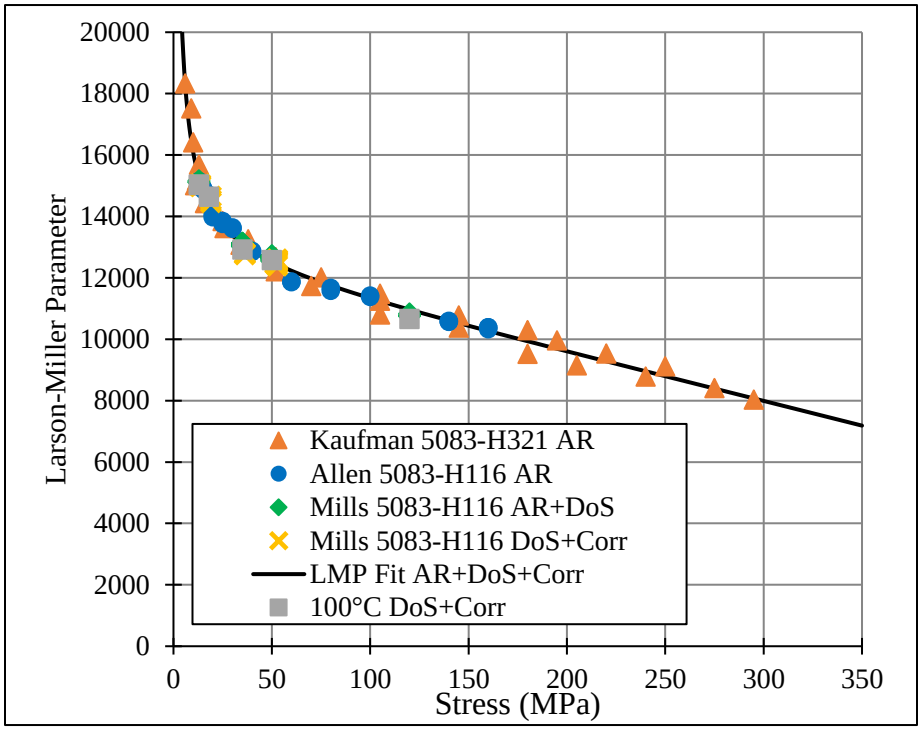

Figure 7-6. LMP_{S+C} Fitting including AR+DoS+Corr 5083-H116 for material sensitized at 100°C and 150°C.

7.3 Modified Kachanov-Rabotnov Creep Model Discussion

7.3.1 Implementation for sensitized at 150°C and corroded material for each testing temperature

Three test conditions were modeled using the Kachanov-Rabotnov tertiary creep model. Figure 7-7 is presented with the K-R model for the 300°C test condition at stress levels for the following samples: AR 3 mg/cm², IGC resistant 20 mg/cm², and heavily sensitized and corrosion susceptible 51 mg/cm² and 61 mg/cm² sensitization levels. Implementing the LMP prediction rupture time, t_{rp}, and predicting an instantaneous strain rate, ε_{0p}, for each creep condition allows Kachanov-

Rabotnov model to be solved. The fit is shown as the dashed lines for the low and high stresses respectively in Figure 7-7. The model fits directly in the middle of the various sensitization levels for both stress levels, which is expected due to the variability in each sensitization level's performance during testing. Table 7-2 contains the predicted rupture time and predicted instantaneous strain rate. As expected, the predicted rupture time was lower for the low stress level ~6900 s, which is nearly 5.5 times longer than the predicted rupture time at the high stress level of ~1200 s. The predicted instantaneous creep rate also differed by a factor of 4.6, with high stress level value being 1.65×10^{-4} s^{-1} and the lower stress level being 3.60×10^{-5} s^{-1}.

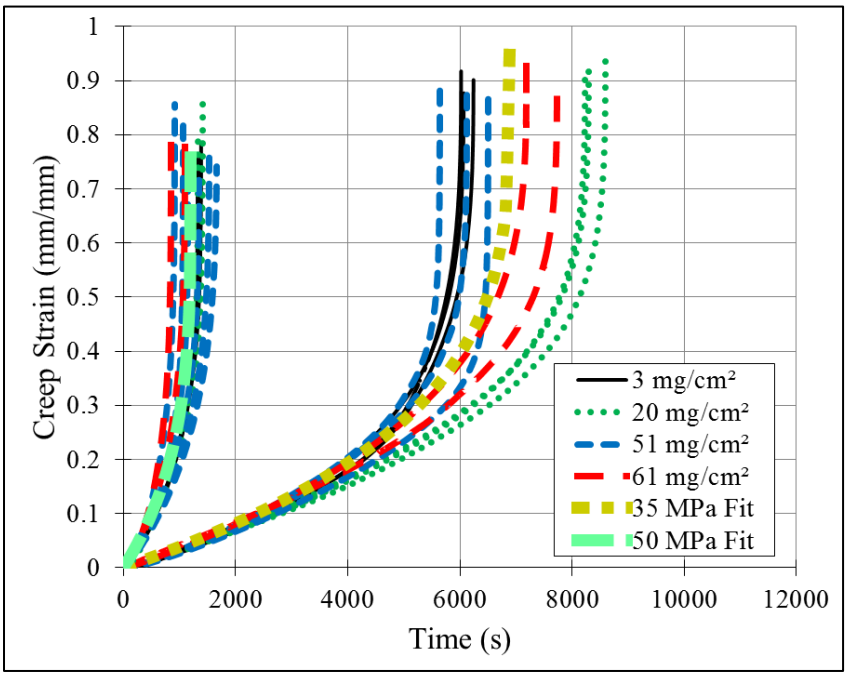

Figure 7-7. Kachanov-Rabotnov fit for 300°C at OSA 35 and 50 MPa of AR and sensitized 5083-H116 with sensitization levels 3-61 mg/cm² [98].

Table 7-2. Predicted rupture times and predicted instantaneous strain rates of various states of 5083-H116 creeped at 300°C and 400°C at low and high stresses [98].

Temperature °C	300	300	400
Damage state	sensitized	corroded	both
Stress levels (MPa)	35, 50	36, 52	13, 19
Low stress t_{rp}	6,892	2,074	2,573
High stress t_{rp}	1,198	675	510
Low stress ε_{0p}	3.60×10^{-5}	8.81×10^{-5}	9.45×10^{-5}
High stress ε_{0p}	1.65×10^{-4}	2.53×10^{-4}	4.62×10^{-4}

Figure 7-8 contains a similar Kachanov-Rabotnov modeling of the various sensitization levels ranging from 51 mg/cm² to 66 mg/cm² that were also corroded along the LT surface prior at the same creep conditions. The model is accurate for the corroded 5083-H116 as well, with a more conservative fit on the higher stress of 50 MPa since more sensitized and corroded material was tested at this condition to see if the different corrosion amounts played a role with increasing sensitization levels. The low stress level had a predicted rupture time of 2074 s, while the high stress level was about three times lower at 675 s. The material subjected to higher stress had an instantaneous strain rate of 2.53×10^{-4} s^{-1}, which was nearly three times steeper than the lower stress-strain rate of 8.74×10^{-5} s^{-1}.

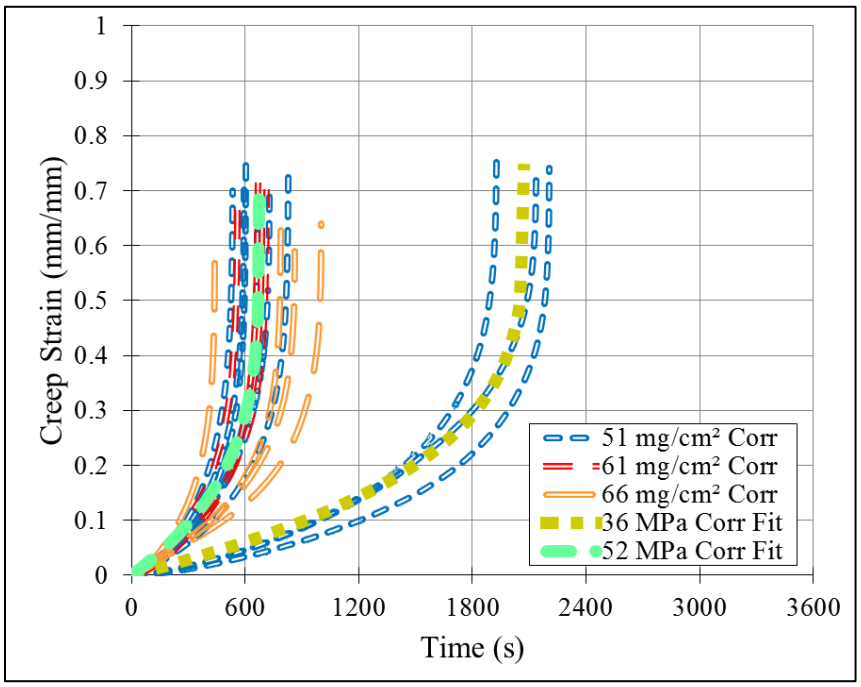

Figure 7-8. Kachanov-Rabotnov fit for 300°C at PCSA 36 and 52 MPa of corroded and sensitized 5083-H116 with sensitization levels 51-66 mg/cm² [98].

Figure 7-9 contains the Kachanov-Rabotnov model at 400°C with 13 MPa and 18 MPa stress levels. The higher stress level had a predicted rupture time of 510 s, which was nearly five times faster than the lower stress predicted time of 2573 s. The predicted strain rate at the high stress level was 4.69×10^{-4} s^{-1}, which was about five times faster than the low stress-strain rate of 9.45×10^{-5} s^{-1}.

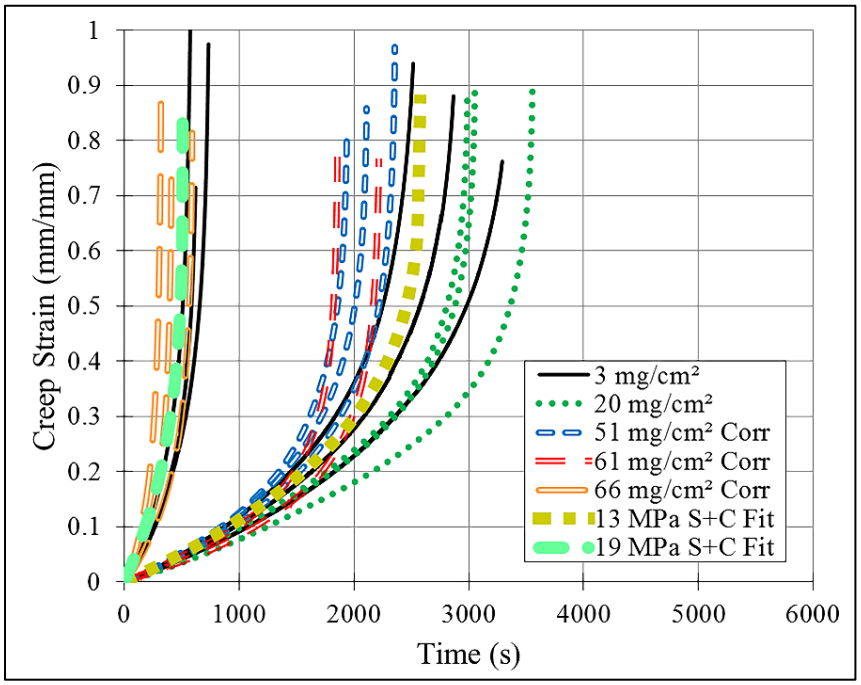

Figure 7-9. Kachanov-Rabotnov fit for 400°C at PCSA 13 and 19 MPa of AR, sensitized, and corroded and sensitized 5083 H116 with corroded sensitization levels >51 mg/cm² [98].

The secondary and tertiary fitting parameters for the updated Kachanov-Rabotnov modeling of AR, sensitized, and corroded 5083-H116 are presented in Table 7-3. When comparing the modeling parameters, the inclusion of corrosion damage at 300°C caused a decrease in all parameters except A and λ. The fitting parameters at 300°C and 400°C vary in values and could not be collapsed into one set of parameters.

Table 7-3 Kachanov-Rabotnov fitting parameters for 5083-H116 data in Figures 7-6, 7-7 and 7-8 [98].

Temperature °C	300	300	400
Damage state	sensitized	corroded	both
Stress levels (MPa)	35, 50	36, 52	13, 19
A	9.43×10^{-12}	2.65×10^{-9}	4.19×10^{-10}
n	4.26	2.90	4.77
B	2.59×10^{11}	1.31×10^{8}	7.33×10^{8}
ν	4.91	3.08	4.86
η	4.76	2.85	5.61
λ	3.84	4.04	3.59

7.4 Creep Testing Conclusions

The effects of sensitization and corrosion on the creep behavior of 5083-H116 have been evaluated for the first time. Samples with varying sensitization levels were generated by exposing AR 5083-H116 to temperatures of 150°C for differing times. Corrosion susceptible sensitized samples were then preferentially corroded on the rolled LT surface for 120 hours at -0.77 V_{SCE} in an artificial saltwater solution. The extent of LT corrosion damage was accounted for in terms of thickness loss, with the assumption that any IGC generated negligible penetration depth. Creep testing was performed at temperatures of 200°C, 300°C, and 400°C. The following conclusions can be made:

- Sensitization damage does not play a significant role in creep performance of 5083-H116.
- Larson-Miller parameters and parameters for the Kachanov-Rabotnov creep model were generated to support modeling of the structural response of 5083-H116 subjected to elevated temperature loading such as during fire. If corrosion effects on net section stress are accounted for, there is no significant difference in the LMP for AR, sensitized, or sensitized and corroded 5083-H116.

8 Cowley Beach Exposure of Lab Sensitized Novelis 5083-H116

8.1 Novelis 5083-H116 Sensitization (Laboratory)

Novelis 5083-H116 was procured and sensitized at 100°C at various times in a fashion similar to that described for Alcoa 5083-H116. The sensitization times chosen for this study related directly to the sensitization times chosen for the 100°C Alcoa 5083-H116 sensitization. Results of the sensitization process are presented below in Figure 8-1. Three distinct states of the Novelis 5083-H116 were available for further testing: AR DoS 4 mg/cm², pitting susceptible DoS 20 mg/cm², and heavily sensitized and IGC susceptible 46 mg/cm². The two sensitization times were 304 hours and 1084 hours respectively.

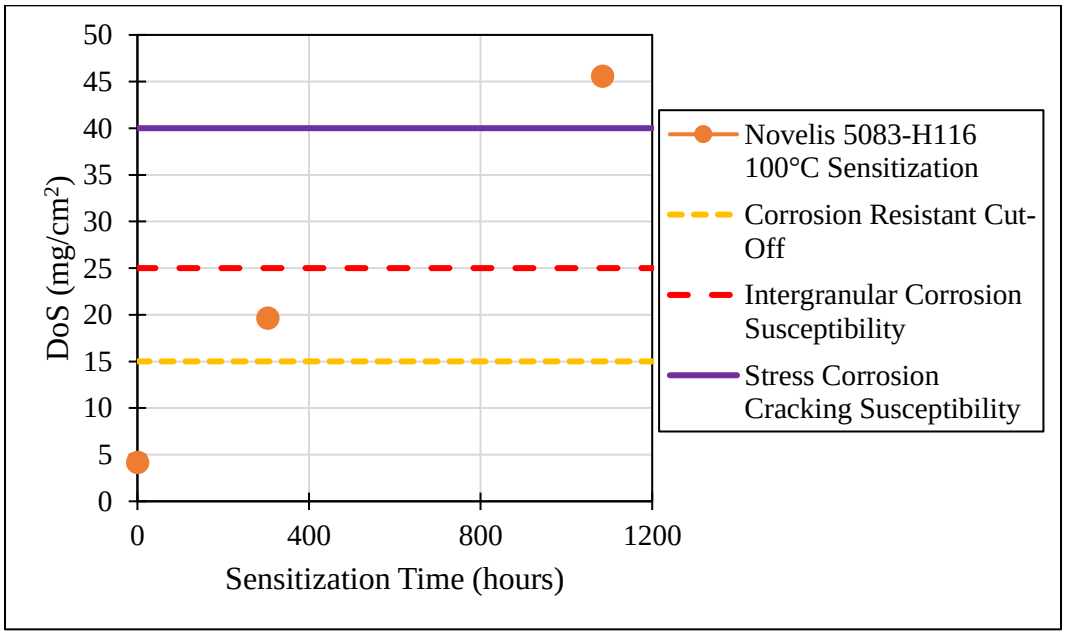

Figure 8-1 Novelis 5083-H116 100°C laboratory sensitization NAMLT results.

In collaboration with the Australian Defense Science and Technology organization, the sensitized Novelis 5083-H116 samples were sent to Cowley Beach in Australia for up to two years exposure. Results are presented in the following sections.

8.2 Beach Exposure of Sensitized 5083-H116

8.2.1 Novelis 5083-H116 Exposure Rack

Dog bone samples were sent to Cowley Beach for exposures of up to two years during the period March 17, 2016 - March 14, 2018. Two types of dog bones were used in this study: one set for

room temperature tension testing and the other for elevated temperature quasi-static tension testing. Figure 8-2 (a) illustrates the samples on Cowley Beach on the exposure rack based upon ASTM G50, with dog bones highlighted by exposure time in Figure 8-2 (b) based on ASTM G50-76 [109]. Samples were removed after exposure to the atmospheric environment for durations of 3, 6, 18, and 24 months.

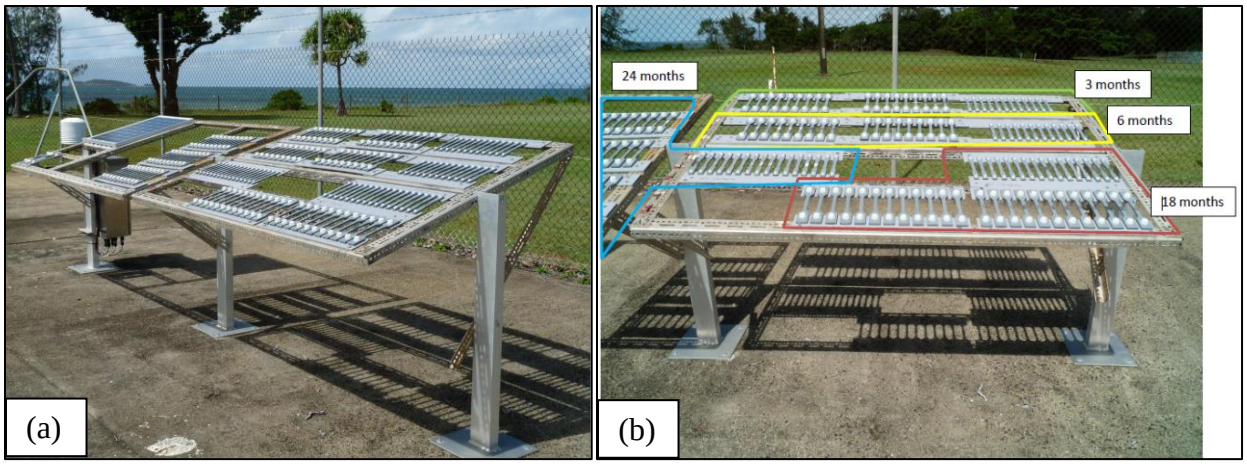

Figure 8-2 Cowley Beach Novelis 5083-H116 atmospheric corrosion exposure setup based on ASTM G50 (a) whole setup and (b) samples highlighted by amount of exposure time [110].

8.2.2 Exposure Rack Data Measurements Station

Various data measurements occurred on the sample exposure rack while at Cowley Beach. Figure 8-3 (a) shows an AR Novelis 5083-H116 dummy plate with a temperature sensor on the top and bottom of the plate. Figure 8-3 (b) shows a sensor for ambient temperature and humidity. The dummy plate is also shown along with a solar cell. Another temperature sensor was employed in an enclosed box presented n Figure 8-3 (b) also. In total, four sets of temperature measurements occurred over the two-year exposure period: ambient temperature (°C), dummy plate top surface temperature (°C), dummy plate bottom surface temperature (°C), and enclosure temperature (°C). Humidity was measure in terms of percent relative humidity (%RH) For all data measurements (five in total), data was collected once every ten minutes for the two-year period. During certain portions of the testing, the data sensor system went offline, and, thus, supplementary data was gathered from other data systems located in Innisfail and South Johnstone. Data gathered from these two sites consisted only of ambient temperature and humidity with data taken in thirty-minute intervals opposed to the ten-minute intervals at Cowley Beach.

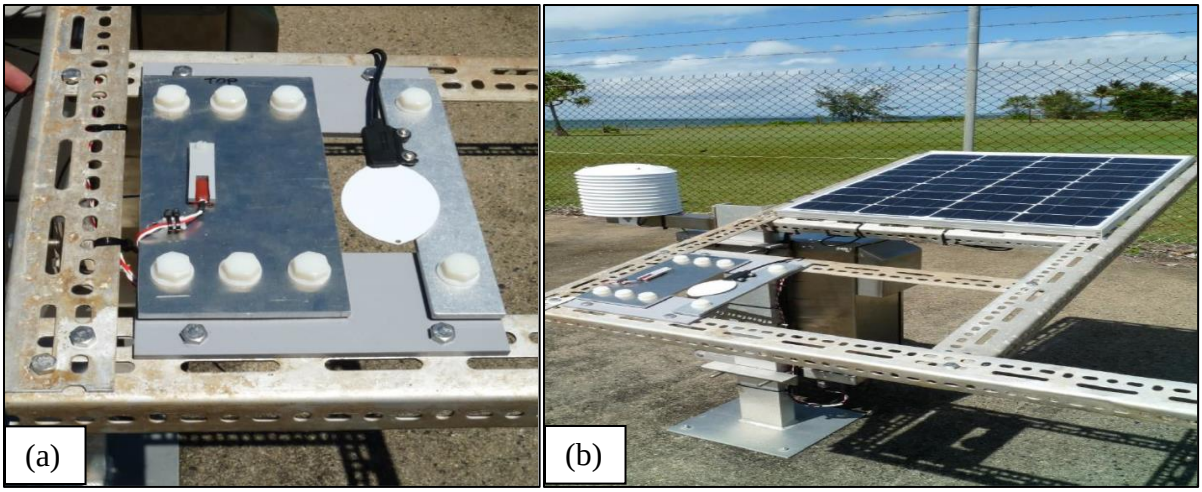

Figure 8-3 Novelis 5083-H116 weather data measurement station at Cowley Beach [110].

8.3 Beach Exposure Data

8.3.1 Temperature and Humidity Measurements

Figures 8-4 through 8-6 provide the data measurements obtained for the beach exposure of the Novelis 5083-H116 samples. Figure 8-4 presents the ambient temperature (°C) obtained over the two-year period from Cowley Beach, along with intermittent ambient temperature data obtained from South Johnstone and Innisfail locations. The data from South Johnstone and Innisfail shows that this data is accurate since the temperature trends from season to season are noticeable for all three locations of temperature measurements. The average ambient temperatures taken at each location were 24.4°C for Cowley Beach, 24.7°C for South Johnstone, and 20.4°C for Innisfail. The average ambient temperatures for all three locations was 24.2°C.

The other remaining temperature measurements, top surface, bottom surface, and enclosure, are listed in Figure 8-5. These temperatures fluctuated between 10 °C and 60°C throughout the two-year exposure period. The median of the top surface was 27.1 °C, the bottom surface was 27.0°C, and the enclosed chamber was 27.6°C. The top and bottom surface temperatures are more representative of the temperatures of the actual dog bones, since they are the same material. Solar heat and the heat capacity of the Novelis 5083-H116 material allowed it to have temperatures higher than the ambient temperatures. Despite this, temperature values obtained from the dummy plate signify that the previously reported lowest sensitization temperature of 40°C was not reached through the majority of the two-year testing period.

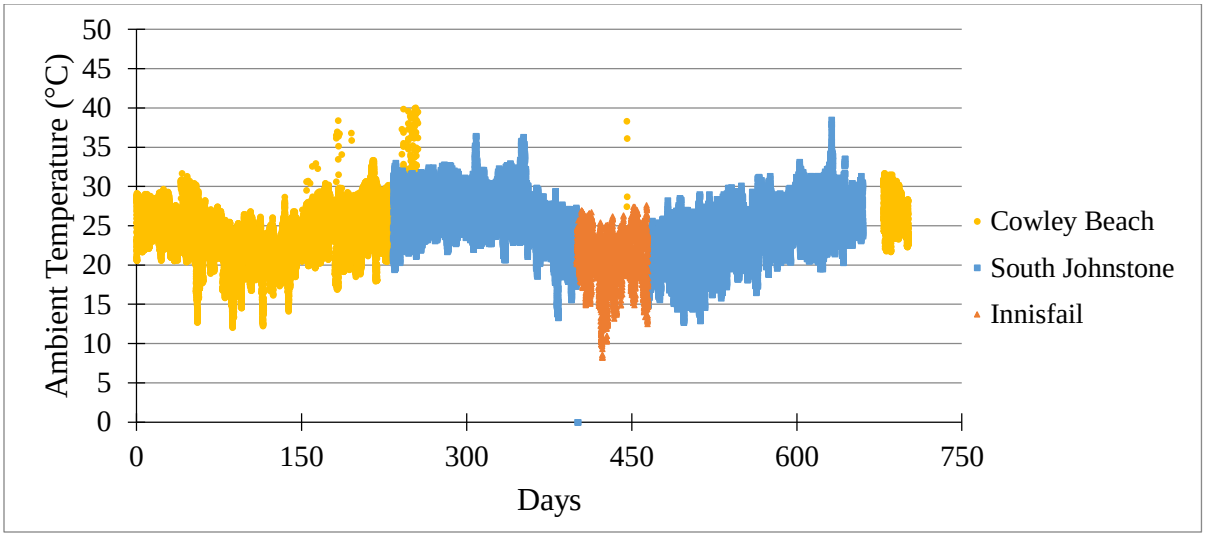

Figure 8-4 Ambient temperature data obtained for the Novelis 5083-H116 Cowley Beach exposure [110].

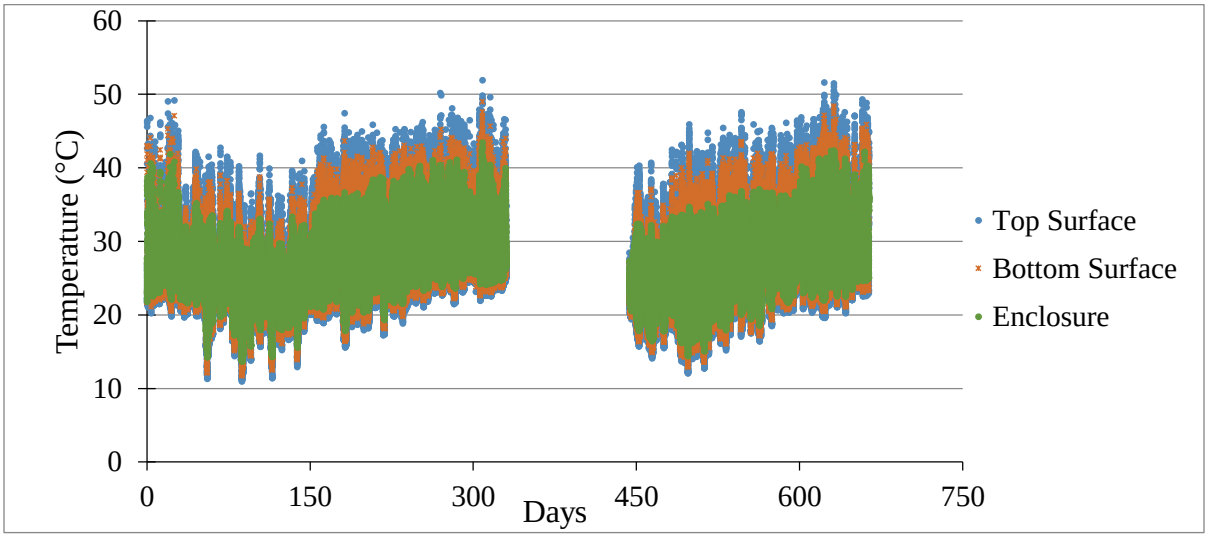

Figure 8-5 Temperature data obtained for the Novelis 5083-H116 Cowley Beach exposure in terms of top surface, bottom surface, and enclosed chamber temperatures [110].

Figure 8-6 contains the %RH data obtained for the two-year Cowley Beach exposure. For the most part, the %RH fluctuated between 40%RH and 100%RH throughout the two-year exposure period. Similar to the ambient temperature measurements, the %RH data is provided for Cowley Beach, South Johnstone, and Innisfail locations. The mean %RH for each location is as follows: 81.8%RH for Cowley Beach, 81.5%RH for South Johnstone, and 86.7%RH for Innisfail. The mean relative humidity for the entire two-year period was 82.2 %RH from these three locations.

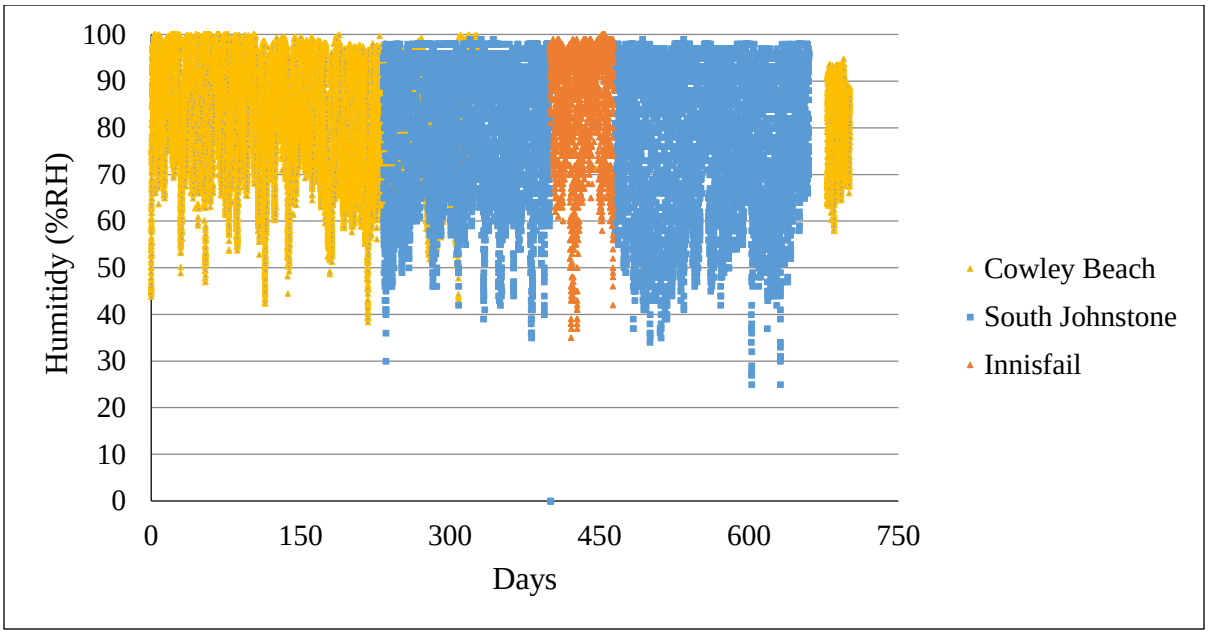

Figure 8-6 Percent relative humidity data obtained for the Novelis 5083-H116 two-year Cowley Beach exposure [110].

8.3.2 Beach Sensitization Alterations

Previous research studies suggested that the sensitization process requires a minimum sensitization temperature of 40°C over an extended period to further sensitize the Novelis 5083-H116 [6], [25], [28], [111]. Figure 8-7 presents the results of the change in DoS of the three different sensitization levels of the Novelis 5083-H116 material from Figure 8-1. The AR Novelis 5083-H116 was not sensitized further over a six-month exposure period. The heavily sensitized (DoS = 46 mg/cm²) samples increased in DoS to 49 mg/cm². Contrary to findings from previous studies, samples with an initial DoS of 20 mg/cm² increased in sensitization to a DoS of 25 mg/cm² after three months of exposure, making the alloy susceptible to IGC damage. After six months of beach exposure, the DoS increased to ~27 mg/cm², which would make it more susceptible to corrosion damage.

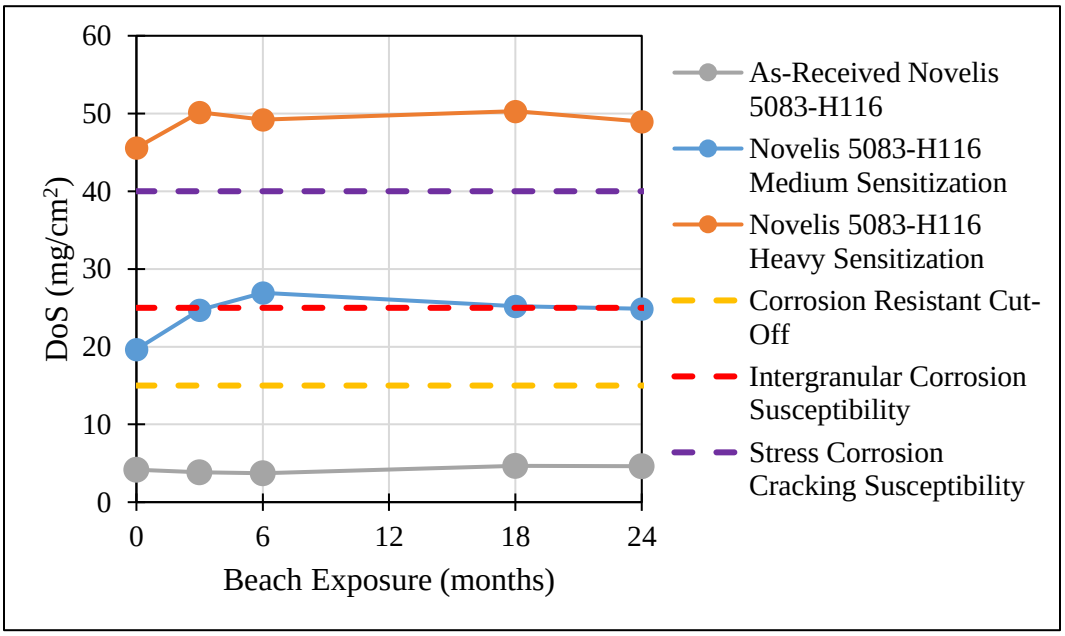

Figure 8-7 Novelis 5083-H116 100°C sensitization NAMLT results.

8.4 Lab and Beach Sensitization Effects on Novelis 5083-H116 Tension Tests

Like the room temperature mechanical testing of the Alcoa 5083-H116 samples, room temperature tension testing was conducted on the Novelis 5083-H116 samples using an Instron 5984 load frame at a displacement rate of 5 mm/min. Results of these tests are presented in the following figures. Figure 8-8 shows the 0.2% offset yield strength results from the 100°C laboratory sensitization and two-year beach exposure (substrate temperature ~27°C and ambient temperature ~24°C). When comparing all three DoS states without beach exposure, the 0.2% offset YS is relatively the same, with the mean values decreasing, but the standard deviation (3 repeats) signifying they are the same. The data from three months and six months seems lower based on the data presented in Figure 8-9; however, an unintentional pre-load of 2 kN was applied when performing the tension tests, and, this as expected, lowered the 0.2% offset YS values. A set of solely lab sensitized samples was tested; the unintentional preloading did lower the apparent 0.2% offset YS by a factor of ~1.08 to 1.10. The three-month and six-month exposed sample 0.2% offset YS values were closer to the solely lab sensitized states of the material at ~255-259 MPa. The 18 month and 24 month exposure of the Novelis 5083-H116 indicated that the 0.2% offset yield strength changed based on sensitization level. The AR material changed from 259 MPa to 258 MPa after two years of exposure at Cowley Beach. The IGC resistant lab DoS 20 mg-cm² changed from 257 MPa to

255 MPa. For both states of the Novelis 5083-H116, beach exposure had no effect on the 0.2% offset YS when standard deviation is accounted for from three repeats at each condition. However, the lab sensitized 46 mg/cm² state of the Novelis 5083-H116 did significantly decrease in 0.2% YS from 255 ± 1 MPa to 248 ± 3 MPa. However, this was only a 2.75% decrease for the heavily sensitized 46 mg/cm² for a two-year beach exposure.

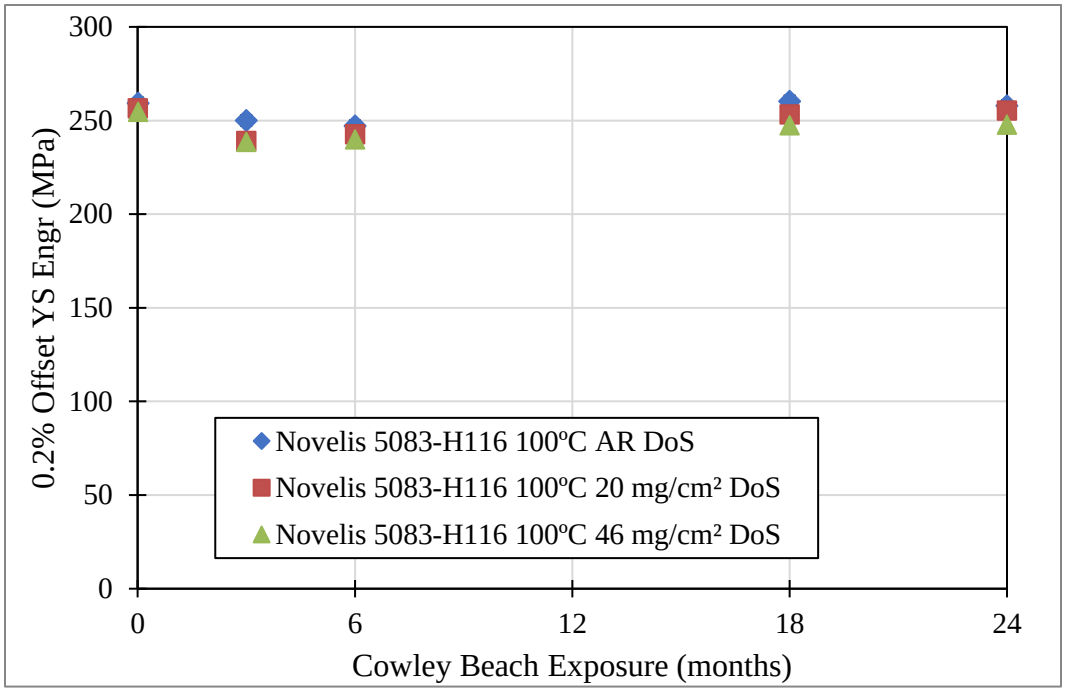

Figure 8-8 Sensitized Novelis 5083-H116 0.2% offset yield strength (engineering) from laboratory sensitization at 100°C along with Cowley Beach exposure up to 24 months.

The UTS is provided in Figure 8-9 for the AR and laboratory 100°C sensitized Novelis 5083-H116 that was exposed at Cowley Beach for up to 24 months. The solely lab sensitized DoS UTS values are as follows: 4 mg/cm² with 366 MPa, 20 mg/cm² with 366 MPa, and 46 mg/cm² with 367 MPa. When including repeatability, none of these are significantly different. The unintended preloading of 2 kN is noticed again in the three-month and six-month UTS data; it was excluded from statistical analysis as the preloading effect would lower the UTS of each tested sample. After 24 months of Cowley Beach environmental exposure, the UTS for the AR Novelis 5083-H116 remained at 366 MPa. For the 24 month exposure of the 100°C, 304 hours lab sensitization DoS 20 mg/cm², the UTS went from 366 ± 0.5 MPa to 367 ± 3.5 MPa. This signified no change in the UTS of the 20 mg/cm² Novelis 5083-H116. However, the UTS of the 46 mg/cm² Novelis 5083-

H116 changed slightly from 366 ± 0.9 MPa to 363 ± 0.66 MPa or roughly a 1.05% decrease in UTS.

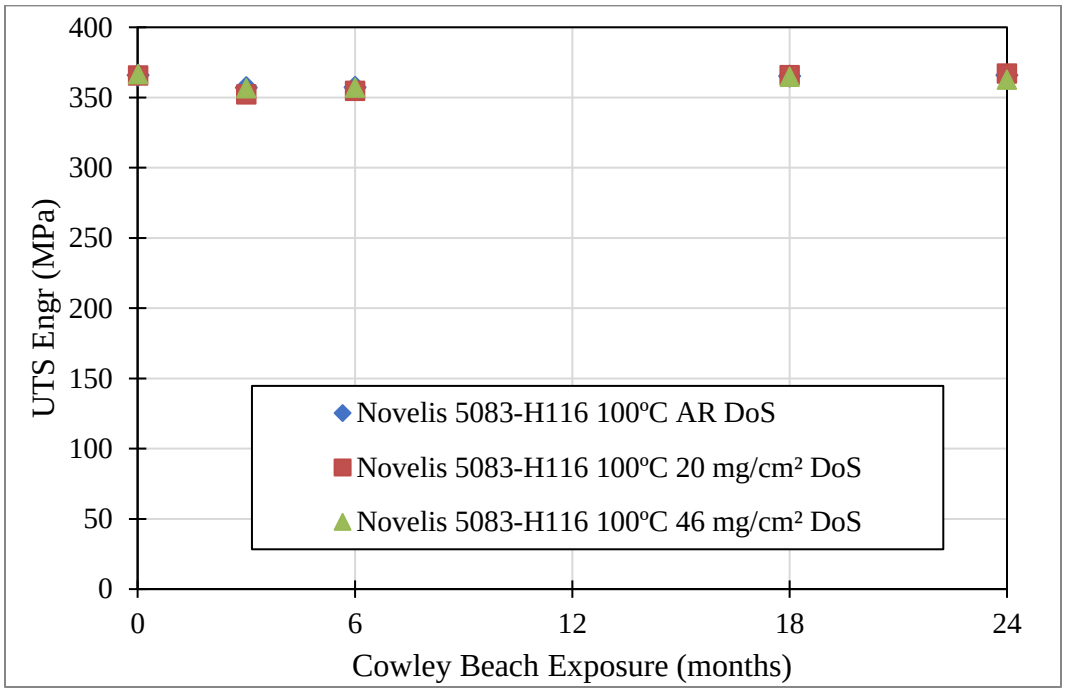

Figure 8-9 Sensitized Novelis 5083-H116 UTS (engineering) from laboratory sensitization at 100°C along with Cowley Beach exposure up to 24 months.

The elastic moduli are shown in Figure 8-10 for the AR and laboratory 100°C sensitized Novelis 5083-H116 that was exposed at Cowley Beach. The solely lab sensitized DoS elastic moduli are listed as follows: 4 mg/cm² with 66.3 ± 2.7 GPa, 20 mg/cm² with 71.2 ± 0.6 GPa, and 46 mg/cm² with 67.8 ± 2.3 GPa. The elastic modulus for the medium sensitization level was statistically higher than the other two DoS. The three-month and six-month data were excluded due to the preloading issue. After 18 months exposure at Cowley Beach, the highest DoS 46 mg/cm² had the highest elastic modulus of 74.7 ± 7.9 GPa; however, this was not significantly higher than the other DoS elastic moduli at this condition. After 24 months of Cowley Beach environmental exposure, the elastic modulus for the 20 mg/cm² Novelis 5083-H116 was the highest at 73.0 ± 5.9 GPa. Once again, with the standard deviation in the elastic moduli at 18 and 24 months, there was no significant difference in the beach exposure effect on the three different DoS used for this study.

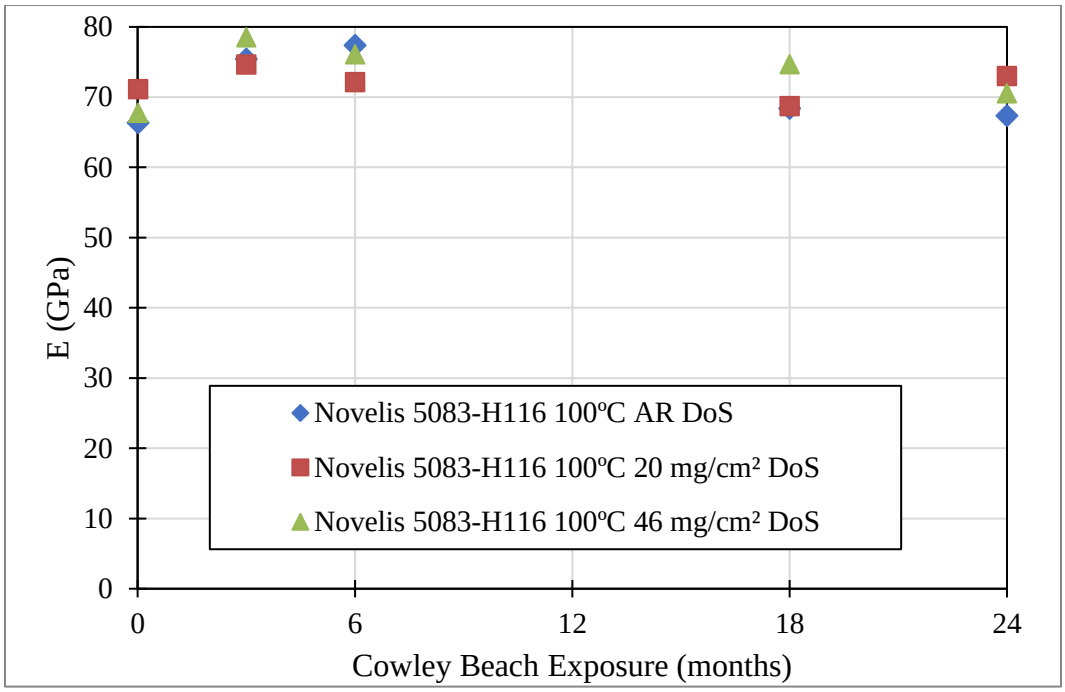

Figure 8-10 Sensitized Novelis 5083-H116 UTS (engineering) from laboratory sensitization at 100°C along with Cowley Beach exposure up to 24 months.

The percent area reduction is provided in Figure 8-12 for the AR and laboratory 100°C sensitized and beach exposed Novelis 5083-H116. The solely lab sensitized DoS %RA values are 4 mg/cm² with 13.5 ± 0.5 %, 20 mg/cm² with 14.4 ± 0.3 %, and 46 mg/cm² with 14.1 ± 0.3 %. The medium sensitization level was statistically higher than the other two DoS once again. The three-month and six-month data were excluded due to the preloading issue again. After 18 months of exposure at Cowley Beach, the medium DoS 20 mg/cm² had the highest elastic modulus of 15.3 ± 0.3%, which was significantly higher than the %RA of the other two DoS. However, after 24 months of Cowley Beach environmental exposure, the %RA for all three DoS was between 14-14.8 %, with no significance between them at the time of exposure. When comparing the 24-month exposure to the laboratory sensitization, the %RA did not change after being exposed to the elements.

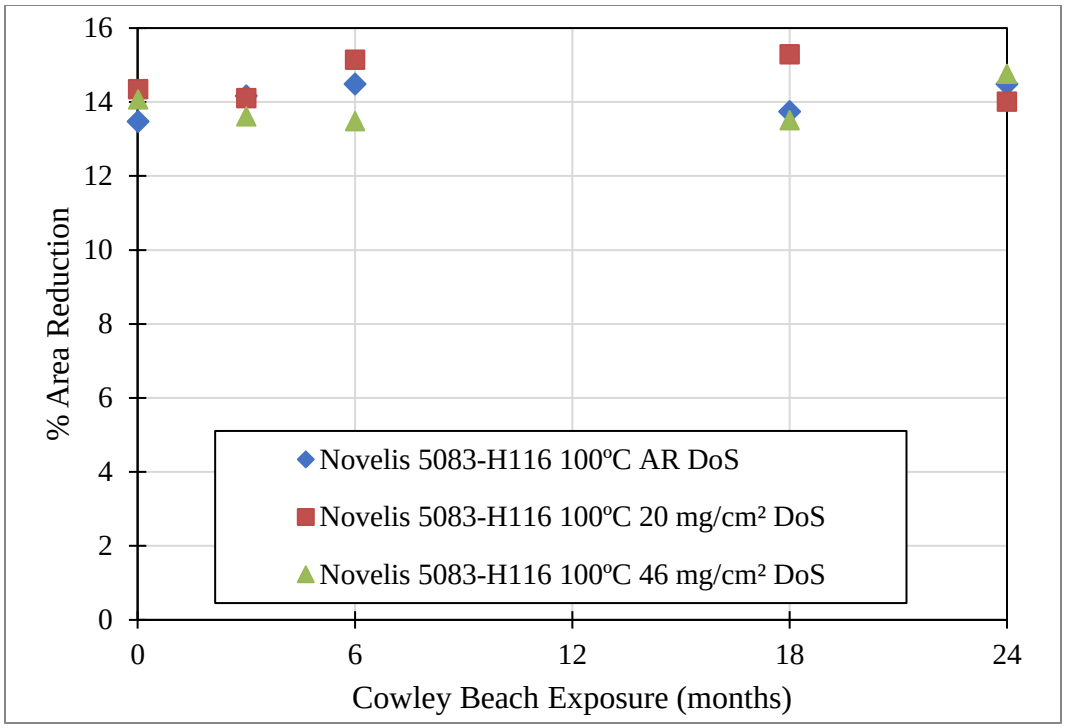

Figure 8-11 Sensitized Novelis 5083-H116 UTS (engineering) shown laboratory sensitization at 100°C along with Cowley Beach exposure up to 24 months.

8.5 Conclusions

Novelis 5083-H116 was sensitized at 100°C for up to 1084 hours and exposed to corrosion on Cowley Beach, Australia for 24 months. Following exposure, NAMLT tests were conducted to identify the extent of additional sensitization damage. Room temperature tension tests conducted on lab sensitized and beach exposed Novelis 5083-H116. Results were quantified in terms of 0.2% offset YS, UTS, elastic moduli, and percent area reduction. Conclusions from this study are as follows:

- Three sensitization levels of Novelis 5083-H116 were exposed for up to 24 months on Cowley Beach. The plate was exposed to ~ 27°C and ~82%RH for the 24-month test. These environmental conditions did not change three sensitization levels of the material. For the IGC resistant samples with a DoS 20 mg/cm², the DoS increased to ~ 25 mg/cm² after three months of exposure. No additional increase in DoS was measured with subsequent beach exposure.
- The Novelis 5083-H116 alloy did demonstrate any significant reduction from the in yield strength, UTS, Young's modulus, or %RA from the 24-month beach exposure when

compared with the AR state of the material. This is consistent with the lack of change in DoS after the 24 month exposure.

9 Conclusions

The research performed in this study relates the sensitization and corrosion effects on 5083-H116 in terms of microstructural and mechanical property changes. Alcoa 5083-H116 was sensitized in an environmental chamber at 100°C and 150°C, leading to different DoS based on times of exposure. Microstructural investigations were conducted on etched sensitized samples. Additionally, samples were subjected to accelerated corrosion for subsequent microstructural investigation and subsequent mechanical (tension and tensile creep) testing. Novelis 5083-H116 was sensitized at 100°C, and dog bone samples were created and exposed for two years in a beach environment to investigate possible sensitization and corrosion effects.

The sensitization and corrosion effects on Alcoa 5083-H116 were investigated in this research study. From the LT surface, the AR 5083-H116 was found to have 89 μm α grain size. The corrosion resistant DoS 20 mg/cm² and corrosion susceptible DoS 51 mg/cm² and 61 mg/cm² had more recrystallized grains (statistically lower), while the DoS 61 mg/cm² was statistically lower at 55 μm than all sensitization levels from the 150°C sensitization. The sensitization levels from the 100°C sensitization showed that α grain size reduction or recrystallization was also present at 31 mg/cm² and 53 mg/cm². No discernible difference was obtained for the LS surface α grain sizes for the AR and sensitized states of Alcoa 5083-H116; however, as expected, the anisotropy index values were higher, which indicates a more elongated grain structure (from the cold-rolling process). As previously reported, increasing DoS led to a more anodic spreading corrosion potential. However, the DoS of 51 mg/cm² (150°C) and 53 mg/cm² (100°C) did have statistically different spreading potentials, which was indicative of differences in B distribution and morphology along GB, respectively at -0.77 V_{SCE} and -0.755 V_{SCE}. Mass loss rates obtained from current density values from potentiostatic holds showed that IGC susceptible DoS material sensitized at 150°C was less corrosion resistant than the material sensitized at 100°C.

On small-scale samples it was found that material sensitized at 150°C had both different forms of corrosion damage (LT exfoliation thickness loss and IGC PD vs LS C-SRS IGC) and differences in thickness loss and penetration depth attack (LT parallel versus. LS perpendicular). The LS surface also experienced more thickness loss and penetration depth (when measured on the corrosion susceptible region) than the LT surface. After 120 hours of accelerated corrosion exposure, the LT surface had uniform exfoliation damage, which increased with DoS for the 150°C

sensitization, while the 100°C DoS had a lowest thickness loss and mainly saw pitting corrosion. However, after 120 hours of corrosion of IGC susceptible 5083-H116, the LS surface reacted the same for both sensitization temperatures utilized in this study.

Tension properties of the Alcoa 5083-H116 were obtained for both sensitization temperatures, along with different exposed corrosion surfaces (LT and LS). The OSA and PCSA assumptions were used to characterize the tension properties (elastic moduli, yield strength, UTS, and percent reduction area). The use of the PCSA assumption allowed for more accurate quantification of the corrosion damage present in the Alcoa 5083-H116 and its relationship to mechanical property degradation. The most significantly affected tension properties were the yield strength and UTS. Without corrosion damage, the yield strength dropped with increasing DoS level for both 100°C and 150°C. When exposed to the corrosion environment for 120 hours, the sensitization 150°C DoS 20 mg/cm² did not drop in YS, while the DoS 51 and >61 mg/cm² had lower YS values. The 100°C only dropped in YS after a corrosion voltage of -0.755 V_{SCE} was used, and the surface orientation did not factor into the YS drop. However, at 51 mg/cm² from the 150°C material, the LT corrosion damage did not lower the YS as much as the LS corrosion damage present. The UTS was not affected by DoS, but corrosion damage did lower the UTS in certain scenarios. For 150°C sensitization and LT corrosion damage, >61 mg/cm² dropped 45 MPa from the AR state of 5083-H116. For the IGC resistant 20 mg/cm² LT corrosion damaged material, the UTS did not drop. Once again, the LT corrosion damage was degrading, but less detrimental to UTS drop for the 150°C DoS 51 mg/cm². For the 100°C 53 mg/cm² corrosion, both the LT and LS corrosion damage lowered the UTS by 18 MPa for -0.755V_{SCE} corrosion, while the -0.77V_{SCE} corrosion did not lower the UTS. The changes in elastic moduli were different, with some conditions increasing and some decreasing in PCSA E with corrosion damage present. In terms of percent reduction area, similar trends were observed, with the higher DoS for 150°C lowering the %RA with corrosion damage, while the corrosion resistant DoS 20 mg/cm² slightly increased with LT corrosion damage. The corrosion damage on the 100°C 53 mg/cm² material lowered the %RA, with the LS corrosion damage causing the most detrimental drop in %RA.

The effects of sensitization and corrosion on the creep behavior of 5083-H116 have been evaluated for the first time. Various sensitization levels were generated after sensitizing AR 5083-H116 at different times at 150°C. Corrosion susceptible sensitized samples were then preferentially

corroded on the rolled LT surface for 120 hours at -0.77 V_{SCE} in an artificial saltwater solution. The LT corrosion damage was accounted for in terms of thickness loss, with the PCSA assumption that any IGC generated negligible penetration depth. Creep testing was performed at a heating rate of 50°C/min and at temperatures 200°C, 300°C, and 400°C. Sensitization damage does not play a role in creep performance of 5083-H116. At 200°C, only 3 mg/cm² and 20 mg/cm² were tested and reacted similarly to the creep environment. At 300°C partial recrystallization likely occurred in the AR and sensitized 5083-H116. Lastly, 400°C creep testing also only had 3 mg/cm² and 20 mg/cm² samples, but full recrystallization occurred. An updated version of the LMP fitting parameters and Kachanov-Rabotnov model were generated, including sensitization and corrosion damage to 5083-H116. While sensitization impacts corrosion susceptibility and the extent of corrosion damage, if the corrosion effects on net section stress are accounted for, there is no significant difference in LMP of AR, sensitized, or sensitized and corroded 5083-H116.

Novelis 5083-H116 was sensitized at 100°C and sent to Cowley Beach for 24 months of environmental exposure. The results were characterized via temperature and humidity monitoring, along with NAMLT and tension testing post beach exposure. The plate was exposed to ~ 27°C and ~82%RH for the 24-month test. The AR DoS was ~4 g/cm² throughout the 24 month exposure, and the corrosion susceptible material increased slightly from 46 mg/cm² to 49 mg/cm². The IGC resistant DoS 20 mg/cm² increased to ~ 25 mg/cm² after three months of exposure and stayed at the same DoS for the remaining beach exposure. The Novelis 5083-H116 did exhibit any significant reduction from the in yield strength, UTS, Young's modulus, or %RA from the 24-month beach exposure when being compared with the AR state of the material.

10 Future Work

Based on the studies presented in this research, a few suggestions for future work are recommended. More sensitization and corrosion damage effects on the microstructure and mechanical properties of 5083 alloys should be investigated.

- Sensitization of 5083-H116 at 175°C or 200°C should be conducted for various lengths of time, with the goal of corrosion and mechanical property investigation. The higher sensitization temperature is known to cause recrystallization, and the added corrosion damage would lower the room temperature tension mechanical properties.

- Creep testing should be conducted at lower temperatures (room temperature up to 200°C). It would be expected that sensitization would have a greater impact on the creep life and the LMP for different sensitization conditions (especially if sensitized at higher sensitization temperatures of 175°C or 200°C). The distinctions between AR and sensitized material creep without corrosion damage would be further characterized at these creep conditions since a lower creep temperature would ensure no temperature dependent mechanical response.

- Etching of the AR and various DoS of the Alcoa 5083-H116 or Novelis 5083-H116 would help reveal the microstructure changes from sensitization. Use of nitric acid or a new phosphoric acid mixed with nitric acid would help better etch GB for a better-quality LT and LS surface α grain size analysis. The emphasis would be to make the grains have more distinct etched GB for automated grain sized analysis on an optical microscope or using the OIM technique from a SEM.

References

[1] F. Latrash, “Advantages of Aluminum in Marine Applications: Lighter, Faster, Stronger,” *Alcoa Defence*, 2010.

[2] M. Skillingberg, “Aluminum at Sea,” *Marine Log*, pp. 27–32, 2007.

[3] M. L. Lim, S. Jain, R. G. Kelly, and J. R. Scully, “Intergranular Corrosion Penetration in AA5083 (UNS # A95083) as a Function of Electrochemical and Metallurgical Conditions,” in *ECS Transactions*, 2012, pp. 177–191.

[4] H. Bushfield, M. Cruder, R. Farley, and J. Towers, “Marine Aluminum Plate—ASTM Standard Specification B 928 and the Events Leading to Its Adoption,” in *October 2003 Meeting of the Society of Naval Architects and Marine Engineers, San Francisco, CA*, 2003, pp. 1–18.

[5] J. L. Searles, P. I. Gouma, and R. G. Buchheit, “Stress Corrosion Cracking of Sensitized AA5083 (Al-4.5 Mg-1.0 Mn),” *Metall. Mater. Trans. A*, vol. 32, no. 11, pp. 2859–2867, 2001.

[6] M. A. Steiner and S. R. Agnew, “Modeling sensitization of Al–Mg alloys via β-phase precipitation kinetics,” *Scr. Mater.*, vol. 102, pp. 55–58, Jun. 2015.

[7] R. H. Jones, D. R. Baer, M. J. Danielson, and J. S. Vetrano, “Role of Mg in the Stress Corrosion Cracking of an Al-Mg Alloy,” *Metall. Mater. Trans. A*, vol. 32, no. 7, pp. 1699–1711, 2001.

[8] D. Jones, *Principles and Prevention of Corrosion*, Second. Prentice-Hall, Inc., 1996.

[9] M. Warmuzek, “Metallagraphic Techniques for Aluminum and Its Alloys,” in *Metallography and microstructures*, Metals Park, Ohio: American Society for Metals, 2004, pp. 711–751.

[10] W. F. Smith, “Chapter 5 Aluminum Alloys,” in *Structures and Properties of Engineering Alloys*, 2nd ed., New York: McGraw-Hill, Inc., 1993, pp. 176–191.

[11] C. Fransson, “Accelerated Aging of Aluminum Alloys,” M.S., Karlstad Universitet, 2009.

[12] R. Abbaschian, L. Abbaschian, and R. E. Reed-Hill, “Chapter 20 Selected Nonferrous Alloy Systems,” in *Physical Metallurgy Principles*, 4th ed., Cengage Learning, p. 660.

[13] K. N. Kulkarni and A. A. Luo, “Interdiffusion and Phase Growth Kinetics in Magnesium-Aluminum Binary System,” *J. Phase Equilibria Diffus.*, vol. 34, no. 2, pp. 104–115, Apr. 2013.

[14] W. D. Callister and D. G. Rethwisch, “Chapter 3 Structures of Metals and Ceramics,” in *Fundamentals of Materials Science and Engineering: An Integrated Approach*, 3rd ed., Danvers, Maryland: John Wiley and Sons, 2008, pp. 37–43.

[15] K. A. Unocic, “Structure-Composition-Property Relationships in 5XXX Series Aluminum Alloys,” PhD, Ohio State University, Columbus, Ohio, 2008.

[16] J. L. Murray, “The Al- Mg (Aluminum-Magnesium) System,” *Bull. Alloy Phase Diagr.*, vol. 3, no. 1, pp. 60–74, 1982.

[17] B. Predel, “Al-Mg (Aluminum - Magnesium,” *Group IV Phys. Chem. Numer. Data Funct. Relatsh. Sci. Technol.*, vol. 12A, pp. 1–5, 2006.

[18] H. Baker, H. Okamoto, and M. Mueller, “Alloy Phase Diagrams: Binary Alloy Phase Diagrams Al-Mg,” in *ASM Handbook*, vol. 3, ASM international/Knovel, 2016, p. 48.

[19] A. Rohatgi, *WebPlotDigitizer*. 2015.

[20] L. Tan and T. R. Allen, “Effect of Thermomechanical Treatment on the Corrosion of AA5083,” *Corros. Sci.*, vol. 52, no. 2, pp. 548–554, Feb. 2010.
[21] R. Goswami, G. Spanos, P. S. Pao, and R. L. Holtz, “Precipitation Behavior of the β Phase in Al-5083,” *Mater. Sci. Eng. A*, no. 527, pp. 1089–1095, 2010.
[22] A. C. Umamaheshwar Rao, V. Vasu, M. Govindaraju, and K. V. Sai Srinadhi, “Influence of Cold Rolling and Annealing on the Tensile Properties of Aluminum 7075 Alloy,” *Procedia Mater. Sci.*, vol. 5, pp. 86–95, 2014.
[23] H. Zhou and T. L. Attard, “Simplified Anisotropic Plasticity Model for Analyzing the Postyield Behavior of Cold-Formed Sheet-Metal Shear Panel Structures,” *J. Struct. Eng.*, vol. 141, no. 7, p. 04014185, Jul. 2015.
[24] P. T. Summers, “Microstructure-Based Constitutive Models for Residual Mechanical Behavior of Aluminum Alloys after Fire Exposure,” Virginia Tech, Blacksburg, VA, 2014.
[25] M. L. Lim, J. R. Scully, and R. G. Kelly, “Intergranular Corrosion Penetration in an Al-Mg Alloy as a Function of Electrochemical and Metallurgical Conditions,” *Corrosion*, vol. 69, no. 1, pp. 35–47, 2013.
[26] M. L. Lim, R. Kelly, and J. Scully, “Overview of Intergranular Corrosion Mechanisms, Phenomenological Observations, and Modeling of AA5083,” *Corrosion*, 2016.
[27] P. Moldovan, C. N. STANICA, and G. CIOBANU, “INTERGRANULAR CORROSION OF AA 5083 - H321 ALUMINUM ALLOY,” *UPB Sci Bull*, vol. 76, no. 3, pp. 169–180, 2014.
[28] A. J. Davenport *et al.*, “Intergranular Corrosion and Stress Corrosion Cracking of Sensitised AA5182,” *Mater. Sci. Forum*, vol. 519–521, pp. 641–646, 2006.
[29] M. Kciuk, “The structure, mechanical properties and corrosion resistance of aluminium AlMg1Si1 alloy,” *J. Achiev. Mater. Manuf. Eng.*, vol. 16, no. 1, p. 6, 2006.
[30] Y.-K. Lin, S.-H. Wang, R.-Y. Chen, T.-S. Hsieh, L. Tsai, and C.-C. Chiang, “The Effect of Heat Treatment on the Sensitized Corrosion of the 5383-H116 Al-Mg Alloy,” *Materials*, vol. 10, no. 275, pp. 1–9, 2017.
[31] D. Singh, P. N. Rao, and R. Jayaganthan, “Microstructures and impact toughness behavior of Al 5083 alloy processed by cryorolling and afterwards annealing,” *Int. J. Miner. Metall. Mater.*, vol. 20, no. 8, pp. 759–769, 2013.
[32] R. Zhang, Y. Zhang, Y. Yan, S. Thomas, C. H. J. Davies, and N. Birbilis, “The effect of reversion heat treatment on the degree of sensitisation for aluminium alloy AA5083,” *Corros. Sci.*, vol. 126, pp. 324–333, 2017.
[33] M. Kciuk, “Structure, mechanical properties and corrosion resistance of AlMg5 alloy,” *J. Achiev. Mater. Manuf. Eng.*, vol. 17, no. 1, p. 4, 2006.
[34] R.-Y. Chen, H.-Y. Chu, C.-C. Lai, and C.-T. Wu, “Effects of annealing temperature on the mechanical properties and sensitization of 5083-H116 aluminum alloy,” *Proc. Inst. Mech. Eng. Part J. Mater. Des. Appl.*, vol. 229, no. 4, pp. 339–346, Aug. 2015.
[35] Y. Chino *et al.*, “Corrosion and Mechanical Properties of Recycled 5083 Aluminum Alloy by Solid State Recycling,” *Mater. Trans.*, vol. 44, no. 7, pp. 1284–1289, 2003.
[36] S. R. Arunachalam, S. E. Galyon Dorman, R. T. Buckley, N. A. Conrad, and S. A. Fawaz, “Effect of electrical discharge machining on corrosion and corrosion fatigue behavior of aluminum alloys,” *Int. J. Fatigue*, vol. 111, pp. 44–53, Jun. 2018.
[37] H. Rahimi, R. Mozaffarinia, and A. Hojjati Najafabadi, “Corrosion and Wear Resistance Characterization of Environmentally Friendly Sol–gel Hybrid Nanocomposite Coating on AA5083,” *J. Mater. Sci. Technol.*, vol. 29, no. 7, pp. 603–608, Jul. 2013.

[38] M. M. Sharma, J. D. Tomedi, and J. M. Parks, “A microscopic study on the corrosion fatigue of ultra-fine grained and conventional Al–Mg alloy,” *Corros. Sci.*, vol. 93, pp. 180–190, Apr. 2015.
[39] E. Bumiller and R. Ruedisueli, “Correlation of electrochemical, ASTM tests and metallographic analyses in the corrosion behavior of 5xx.pdf,” in *NACE International*, 2009, pp. 1–14.
[40] K. Jafarzadeh, T. Shahrabi, and M. G. Hosseini, “EIS Study on Pitting Corrosion of AA5083-H321 Aluminum- Magnesium Alloy in Stagnant 3.5% NaCl Solution,” *J Mater Sci Technol*, p. 5, 2008.
[41] R. H. Jones, V. Y. Gertsman, J. S. Vetrano, and C. F. Windisch, “Crack-particle interactions during intergranular stress corrosion of AA5083 as observed by cross-section transmission electron microscopy,” *Scr. Mater.*, vol. 50, no. 10, pp. 1355–1359, 2004.
[42] M. Kciuk, A. Kurc, and J. Szewczenko, “Structure and corrosion resistance of aluminium AlMg2.5; AlMg5Mn and AlZn5Mg1 alloys,” *J. Achiev. Mater. Manuf. Eng.*, vol. 41, p. 8, 2010.
[43] L. Kramer, M. Phillippi, W. T. Tack, and C. Wong, “Locally Reversing Sensitization in 5xxx Aluminum Plate,” *J. Mater. Eng. Perform.*, 2011.
[44] J. P. Labukas and K. E. Strawhecker, “Scanning Probe Investigation of Pitting Corrosion on Aluminum 5083 H131:,” Defense Technical Information Center, Fort Belvoir, VA, 2014.
[45] J. A. Lyndon, R. K. Gupta, M. A. Gibson, and N. Birbilis, “Electrochemical behaviour of the β-phase intermetallic (Mg2Al3) as a function of pH as relevant to corrosion of a.pdf,” *Corros. Sci.*, vol. 70, pp. 290–293, 2013.
[46] M. Trueba and S. P. Trasatti, “The repassivation response from single cycle anodic polarization: The case study of a sensitized Al-Mg alloy,” *Electrochimica Acta*, vol. 259, pp. 492–499, 2018.
[47] W. Wei, S. González, T. Hashimoto, R. R. Abuaisha, G. E. Thompson, and X. Zhou, “In-service sensitization of a microstructurally heterogeneous AA5083 alloy: Atmosphere temperature sensitization of AA5083 for 40 years,” *Mater. Corros.*, vol. 67, no. 4, pp. 378–386, Apr. 2016.
[48] J. Yan, N. M. Heckman, L. Velasco, and A. M. Hodge, “Improve sensitization and corrosion resistance of an Al-Mg alloy by optimization of grain boundaries,” *Sci. Rep.*, vol. 6, no. 1, 2016.
[49] I. N. A. Oguocha, O. J. Adigun, and S. Yannacopoulos, “Effect of Sensitization Heat Treatment on Properties of Al–Mg Alloy AA5083-H116,” *J. Mater. Sci.*, vol. 43, no. 12, pp. 4208–4214, 2008.
[50] F. Bovard and J. Curran, “Development of Test Specimens for Evaluating SCC Behavior of Marine Aluminum Alloys and Assessment of the Severity of Various Marine Exposure Conditions,” p. 7.
[51] J. K. Brosi and J. J. Lewandowski, “Delamination of a sensitized commercial Al–Mg alloy during fatigue crack growth,” *Scr. Mater.*, vol. 63, no. 8, pp. 799–802, Oct. 2010.
[52] J. C. Chang and T. H. Chuang, “Stress-corrosion cracking susceptibility of the superplastically formed 5083 aluminum alloy in 3.5 pct NaCl solution,” *Metall. Mater. Trans. A*, vol. 30, no. 12, pp. 3191–3199, 1999.
[53] R.-Y. Chen and C.-C. Lai, “Reversing Sensitization of Naturally Exfoliated 5456-H116 Aluminum Alloys,” *J. Mar. Sci. Technol.*, vol. 22, no. 4, pp. 450–454, Aug. 2014.

[54] J. Gao and D. J. Quesnel, “The Effect of Sensitization on Stress Corrosion Cracking of AA5083,” *NACE Int. Coorrosion Expo*, pp. 1–14, 2010.
[55] D. C. Hart, “5xxx Aluminum Sensitization and Application of Laminated Composite Patch Repairs,” in *Joining Technologies for Composites and Dissimilar Materials, Volume 10*, G. L. Cloud, E. Patterson, and D. Backman, Eds. Cham: Springer International Publishing, 2017, pp. 21–32.
[56] N. J. H. Holroyd, T. L. Burnett, M. Seifi, and J. J. Lewandowski, “Improved understanding of environment-induced cracking (EIC) of sensitized 5XXX series aluminium alloys,” *Mater. Sci. Eng. A*, vol. 682, pp. 613–621, Jan. 2017.
[57] R. L. Holtz, P. S. Pao, R. A. Bayles, T. M. Longazel, and R. Goswami, “Corrosion Fatigue of Al 5083-H131 Sensitized at 70,100, and 175°C Relation to Microstructure & Degree of Sensitization,” in *Corrosion Resistant Metallic Alloys II*, La Quinta, CA, 2011, pp. 1–11.
[58] R. L. Holtz, P. S. Pao, R. A. Bayles, T. M. Longazel, and R. Goswami, “Corrosion-Fatigue Behavior of Aluminum Alloy 5083-H131 Sensitized at 448 K (175 °C),” *Metall. Mater. Trans. A*, vol. 43, no. 8, pp. 2839–2849, Aug. 2012.
[59] D. Li, H. Hassan, A. El-Shabasy, and J. J. Lewandowski, “Effect of Sensitization on the Microstructure and the Mechanical Properties of 5xxx Aluminum Alloys,” Case Western Reserve University.
[60] P. S. Pao and R. Goswami, “Corrosion Fatigue Crack Growth in Sensitized Al 5083,” in *Fatigue of Materials Advances and Emergences in Understanding*, 2010, pp. 85–91.
[61] P. S. Pao, R. L. Holtz, R. Goswami, and R. A. Bayles, “Effect of Sensitization on Corrosion-Fatigue Cracking in Al 5083 Alloy:,” Defense Technical Information Center, Fort Belvoir, VA, Jan. 2015.
[62] M. Seifi, I. Ghamarian, P. Samimi, P. C. Collins, N. J. H. Holroyd, and J. J. Lewandowski, “Sensitization and remediation effects on environmentally assisted cracking of Al-Mg naval alloys,” *Corros. Sci.*, vol. 138, pp. 219–241, Jul. 2018.
[63] P. T. Summers, S. W. Case, and B. Y. Lattimer, “Residual mechanical properties of aluminum alloys AA5083-H116 and AA6061-T651 after fire,” *Eng. Struct.*, vol. 76, pp. 49–61, Oct. 2014.
[64] “ASTM G67-13 Standard Test method for Determining the Susceptibility to Intergranular Corrosion of 5XXX Series Aluminum Alloys by Mass Loss After Exposure to Nitric Acid (NAMLT Test),” *ASTM Int.*, pp. 1–3, 2014.
[65] R. Zhang, S. P. Knight, R. L. Holtz, R. Goswami, C. H. J. Davies, and N. Birbilis, “A Survey of Sensitization in 5xxx Series Aluminum Alloys,” *Corrosion*, vol. 72, no. 2, pp. 144–159, Feb. 2016.
[66] S. Syed, “Atmospheric Corrosion of Materials,” *Emir. J. Eng. Res.*, vol. 11, no. 1, pp. 1–24, 2006.
[67] P. R. Roberge and M. Tullmin, “Chapter 18 Atmospheric Corrosion,” in *Uhlig’s Corrosion Handbook*, 2nd ed., New York: Wiley, 2000, pp. 305–321.
[68] K. Barton, *Protection against atmospheric corrosion : theories and methods*. New York,USA: John Wiley & Sons, 1976.
[69] Cohen, “Aluminum,” no. 35, p. 197, 1988.
[70] J. H. Wilkinson and W. S. Patterson, “The influence of humidity on the atmospheric corrosion of zinc, aluminium, and iron coated with electrolytes,” *J. Soc. Chem. Ind.*, vol. 60, no. 2, pp. 42–44, Feb. 1941.

[71] A. Bakhtiarinejad, K. Ranjbar, A. Ashrafi, and B. Rezaei, “PITTING CORROSION AND METASTABLE PITTING INITIATION RATE OF 5083 ALUMINUM ALLOY IN SYNTHETIC SEA WATER AS A FUNCTION OF MEDIUM PH,” p. 9, 2014.
[72] S. Jain, M. L. C. Lim, J. L. Hudson, and J. R. Scully, “Spreading of intergranular corrosion on the surface of sensitized Al-4.4Mg alloys: A general finding,” *Corros. Sci.*, vol. 59, pp. 136–147, 2012.
[73] H. Ezuber, A. El-Houd, and F. El-Shawesh, “A study on the corrosion behavior of aluminum alloys in seawater,” *Mater. Des.*, vol. 29, no. 4, pp. 801–805, Jan. 2008.
[74] N. L. Sukiman *et al.*, “Durability and Corrosion of Aluminium and Its Alloys: Overview, Property Space, Techniques and Developments,” in *Aluminium Alloys - New Trends in Fabrication and Applications*, Z. Ahmad, Ed. InTech, 2012.
[75] M. L. C. Lim, R. Matthews, M. Oja, R. Tryon, R. G. Kelly, and J. R. Scully, “Model to predict intergranular corrosion propagation in three dimensions in AA5083-H131,” *Mater. Des.*, vol. 96, pp. 131–142, Apr. 2016.
[76] L. Tan and T. R. Allen, “Effect of thermomechanical treatment on the corrosion of AA5083,” *Corros. Sci.*, vol. 52, no. 2, pp. 548–554, Feb. 2010.
[77] X. Zhao, “Exfoliation Corrosion Kinetics of High Strength Aluminum Alloys,” Ohio State University, Columbus, Ohio, 2006.
[78] R. Goswami, G. Spanos, P. S. Pao, and R. L. Holtz, “Microstructural Evolution and Stress Corrosion Cracking Behavior of Al-5083,” *Metall. Mater. Trans. A*, vol. 42, no. 2, pp. 348–355, Feb. 2011.
[79] R. K. Gupta, R. Zhang, C. H. J. Davies, and N. Birbilis, “Influence of Mg Content on the Sensitization and Corrosion of Al-xMg(-Mn) Alloys,” *Corrosion*, vol. 69, no. 11, pp. 1081–1087, 2013.
[80] D. Scotto D’Antuono, J. Gaies, W. Golumbfskie, and M. L. Taheri, “Grain boundary misorientation dependence of β phase precipitation in an Al–Mg alloy,” *Scr. Mater.*, vol. 76, pp. 81–84, Apr. 2014.
[81] Y. Zhao, M. N. Polyakov, M. Mecklenburg, M. E. Kassner, and A. M. Hodge, “The role of grain boundary plane orientation in the β phase precipitation of an Al–Mg alloy,” *Scr. Mater.*, vol. 89, pp. 49–52, Oct. 2014.
[82] R. Zhang *et al.*, “The influence of grain size and grain orientation on sensitisation in AA5083,” *Corrosion*, pp. 160-168, 2016.
[83] Y. Zhu, “Chracterization of Beta Phaste Growth and Experimental Validation of Long Term Thermal Exposure Sensitization of AA5XXX Alloys,” University of Utah, 2013.
[84] R. Mills, B. Lattimer, and S. Case, “Corrosion Effects on Mechanical Properties of Sensitized AA5083-H116,” in *TMS 2016 Annual Meeting Supplemental Proceedings*, Nashville, TN, 2016, pp. 625–632.
[85] W. L. Mankins, “Recovery, Recrystallization, and Grain-Growth Structures,” in *Metallography and Microstructures*, vol. 9, ASM International, 2004, pp. 207–214.
[86] K. L. Deffenbaugh, “Grain Size Control in AA5083: Thermomechanical Processing and Particle Stimulated Nucelation,” Master’s of Science, Naval Postgraduate School, Monterey, California, 2004.
[87] O. J. Adigun, “The effect of sensitization on the corrosion susceptibility and tensile properties of AA5083 Al.pdf,” Master of Science, University of Saskatchewan, 2006.
[88] E. C. Cormack, “The effect of sensitization on the stress corrosion cracking of aluminum alloy 5456,” Monterey, California. Naval Postgraduate School, 2012.

[89] J. C. Free, P. T. Summers, B. Y. Lattimer, and S. W. Case, “MECHANICAL PROPERTIES OF 5000 SERIES ALUMINUM ALLOYS FOLLOWING FIRE EXPOSURE,” in *TMS 2016 Annual Meeting Supplemental Proceedings*, Nashville, TN, 2016, pp. 657–663.
[90] Allied High Tech Products, Inc., “Aluminum 5083-H116, 6061-T651 & Powder Metal Copper,” Application Lab Report, 2014.
[91] “ASTM E112-13 Standard Test Methods for Determing Average Grain Size,” *ASTM Int.*, pp. 1–28, 2014.
[92] M. Funk and S. Meister, *LineCut: Grain and Particle Analysis with Line Intersection Methos*. Karlsruhe Insistute of Technology (KIT), 2012.
[93] GAMRY, “Application Note: Reference Electrodes,” *GAMRY Instruments*, 2013. [Online]. Available: https://www.gamry.com/application-notes/electrodes-cells/reference-electrodes/.
[94] GAMRY, “Application Note: Measuring the Impedance of Your Reference Electrode,” *GAMRY Instruments*, 2013. [Online]. Available: https://www.gamry.com/application-notes/electrodes-cells/measuring-the-impedance-of-your-reference-electrode/.
[95] R. J. Mills, “Sensitization and Corrosion Damage of AA5083-H116,” presented at the ONR Review Meeting, Washington, D.C., 2014.
[96] R. J. Mills, “Corrosion Effects on Mechanical Properties of Sensitized AA5083-H116,” presented at the TMS 2016 Annual Meeting Supplemental Proceedings, Nashville, TN, Feb-2016.
[97] “ASTM E139-11 Standard Test Methods for Conducting Creep, Creep-Rupture, and Stress-Rupture Test of Metallic Materials,” *ASTM Int.*, pp. 1–14, 2011.
[98] R.J. Mills, B. Y. Lattimer, S. W. Case, and A. P. Mouritz, “The Influence of Sensitization and Corrosion on Creep of 5083-H116,” *Corros. Sci.*, vol. 143, October, pp. 1–9, 2018.
[99] “ASTM E8/E8M-11 Standard Test Methods for Tension Testing of Metallic Materials,” *ASTM Int.*, pp. 1–28, 2011.
[100] P. T. Summers *et al.*, “Overview of aluminum alloy mechanical properties during and after fires,” *Fire Sci. Rev.*, vol. 4, no. 1, pp. 1–36, 2015.
[101] B. W. Allen, “Creep and Elevated Temperature Mechanical Properties of 5083 and 6061 Aluminum,” M.S., Virginia Tech, Blacksburg, VA, 2012.
[102] N. Cholewa, P. T. Summers, S. Feih, A. P. Mouritz, B. Y. Lattimer, and S. W. Case, “A Technique for Coupled Thermomechanical Response Measurement Using Infrared Thermography and Digital Image Correlation (TDIC),” *Exp. Mech.*, vol. 56, no. 2, pp. 145–164, Feb. 2016.
[103] L. M. Kachanov, “Rupture time under creep conditions,” *Int. J. Fract.*, no. 97, pp. 11–18, 1999.
[104] Y. N. Rabatnov, “Creep problems in structural members,” North-Holland, Amsterdam, 1969.
[105] J. G. Kaufman, *Properties of Aluminum Alloys: Tensile, Creep and Fatigue Data at High and Low Temperatures*. 1999.
[106] J. Yan, N. M. Heckman, L. Velasco, and A. M. Hodge, “Improve sensitization and corrosion resistance of an Al-Mg alloy by optimization of grain boundaries,” *Sci. Rep.*, vol. 6, no. 1, Jul. 2016.
[107] Y. Chen, “Stress-Induced and Post-Fire Response of Aluminum Alloys,” PhD, Virginia Tech, Blacksburg, VA, 2014.

[108] Y. Chen, S. B. Puplampu, P. T. Summers, B. Y. Lattimer, D. Penumadu, and S. W. Case, "Quantification of stress-induced damage and post-fire response of 5083 aluminum alloy," *Mater. Sci. Eng. A*, vol. 641, pp. 369–379, 2015.
[109] "ASTM G50-76 Standard Practice for Conduting Atmospheric Corrosion Tests on Metals," *ASTM Int.*, pp. 1–5, 2003.
[110] M. Mathys, V. Jeleniewski, and I. Burch, "Cowley Beach Exposure," 2015-2018.
[111] D. Li, H. Hassan, A. El-Shabasy, and J. J. Lewandowski, "Effect of Sensitization on the Microstructure and the Mechanical Properties of 5xxx Aluminum Alloys," p. 1.

Appendix A

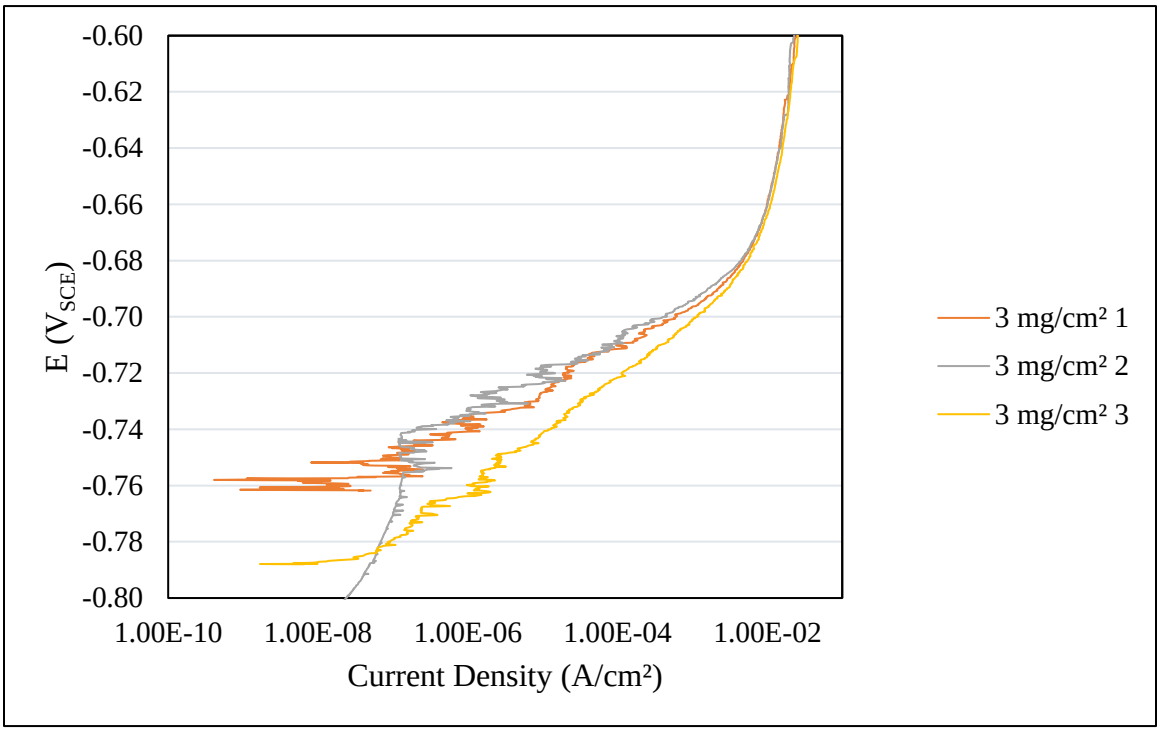

Figure A-1 as-received Alcoa 5083-H116 3 mg/cm² potentiodynamic scans.

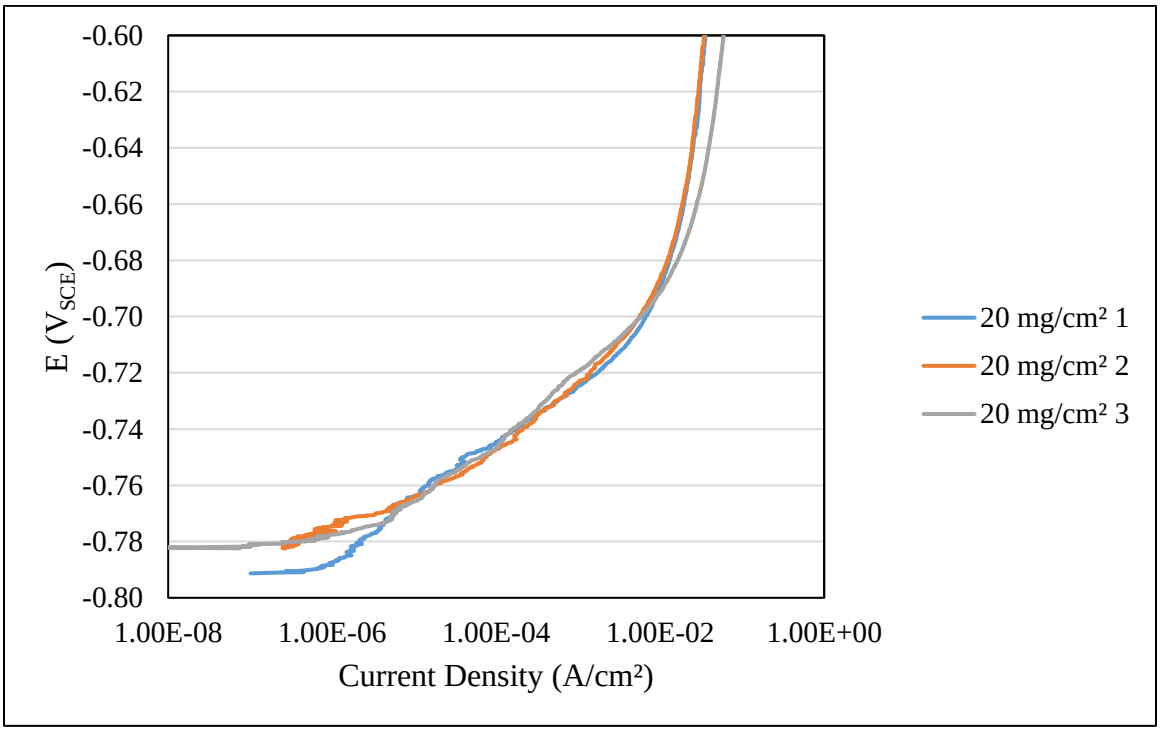

Figure A-2 sensitized (150°C) Alcoa 5083-H116 20 mg/cm² potentiodynamic scans.

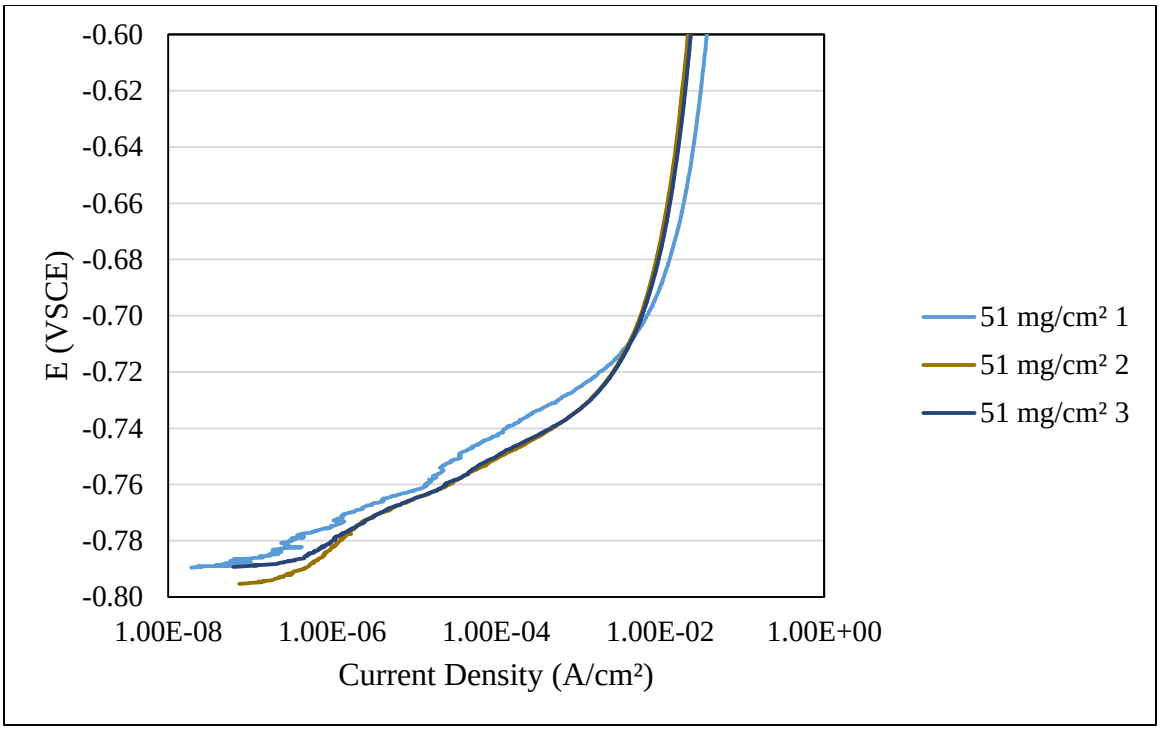

Figure A-3 sensitized (150°C) Alcoa 5083-H116 51 mg/cm² potentiodynamic scans.

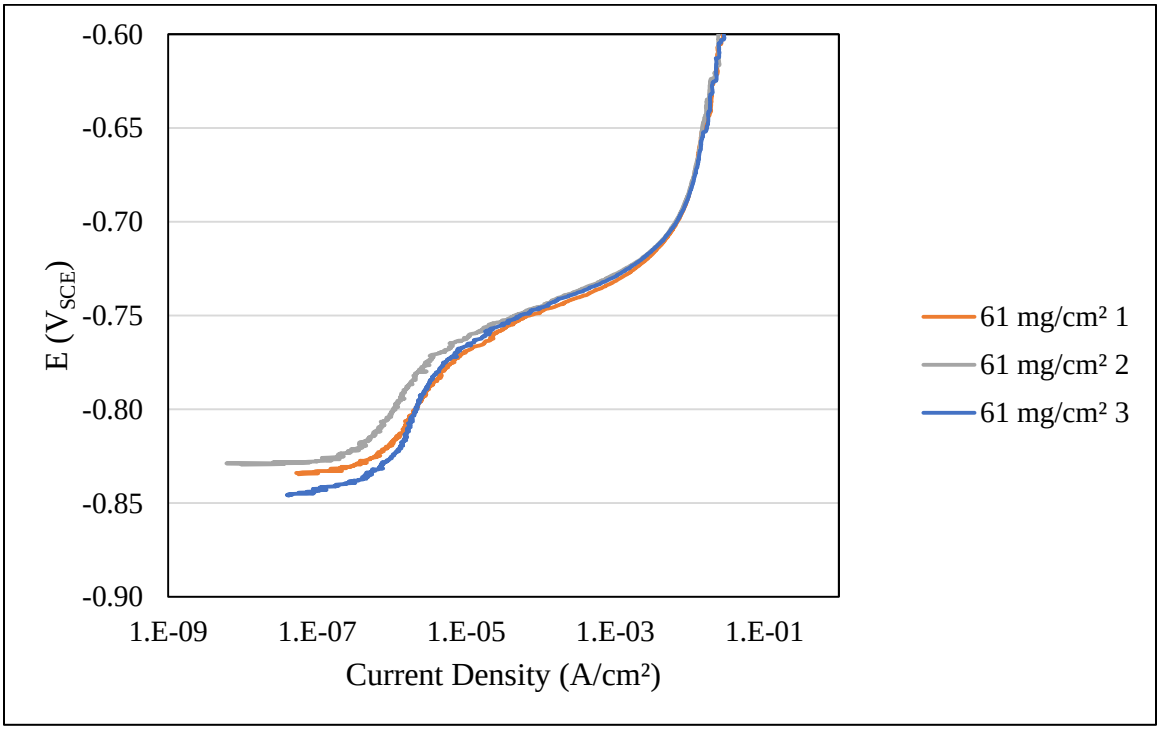

Figure A-4 sensitized (150°C) Alcoa 5083-H116 61 mg/cm² potentiodynamic scans.

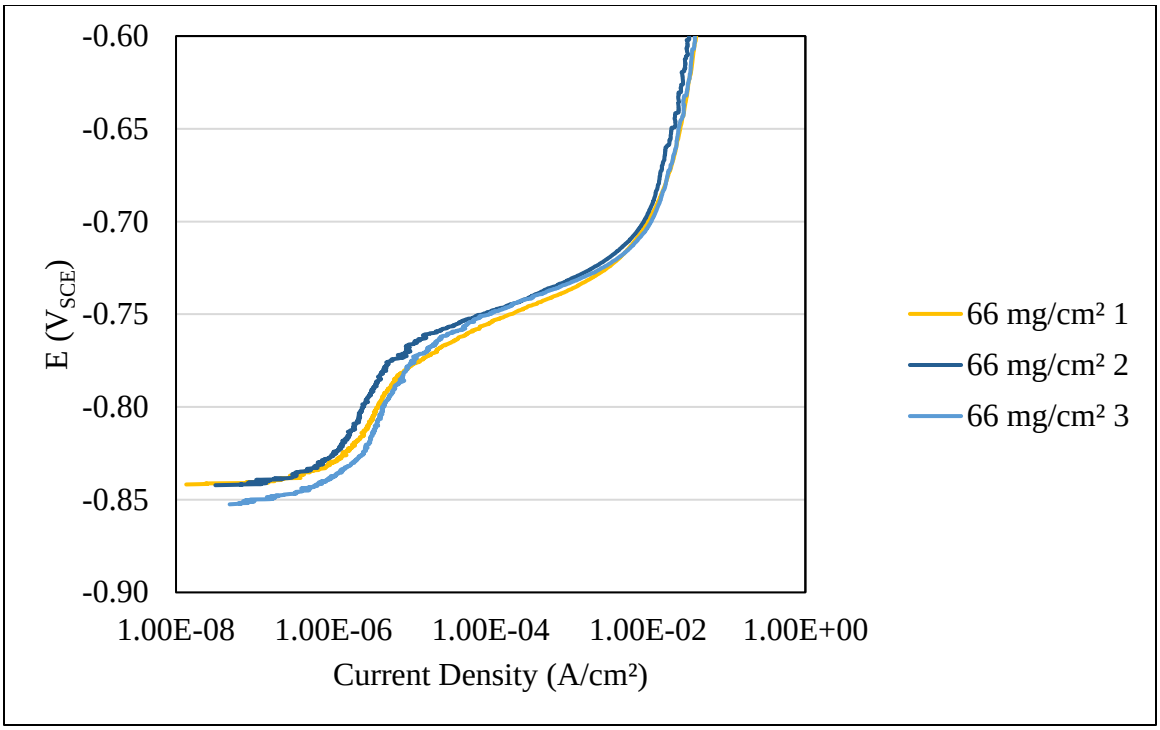

Figure A-5 sensitized (150°C) Alcoa 5083-H116 66 mg/cm² potentiodynamic scans.

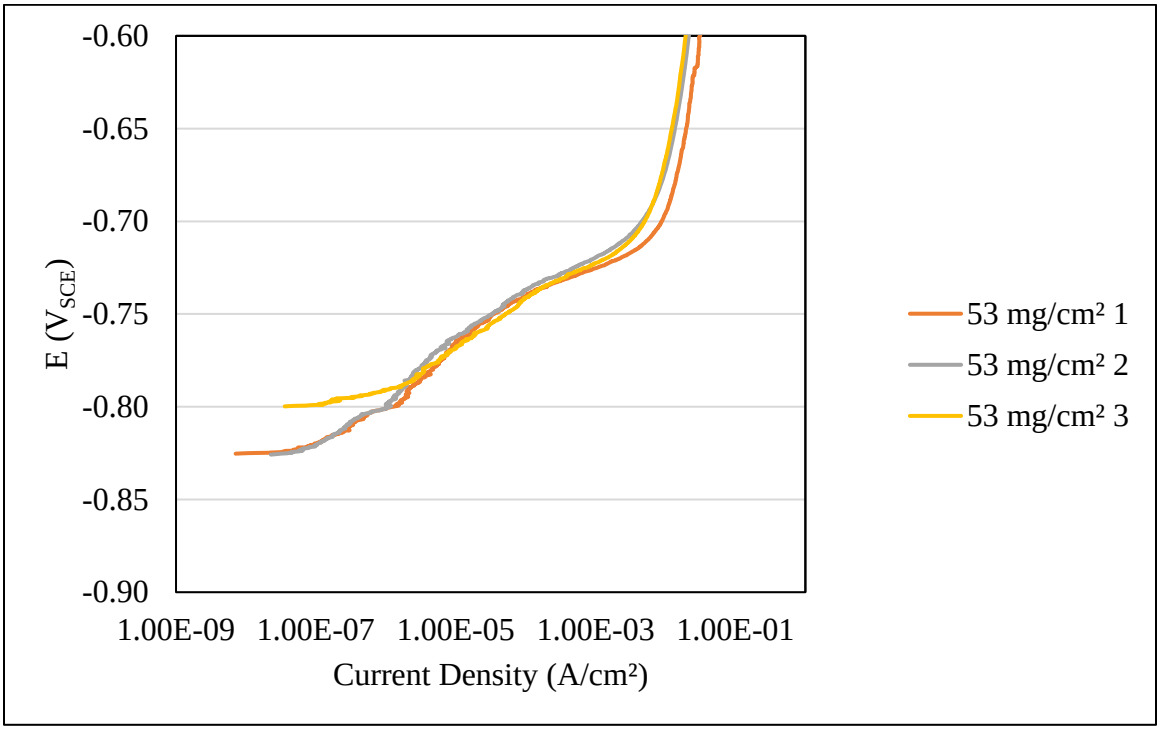

Figure A-6 sensitized (100°C) Alcoa 5083-H116 53 mg/cm² potentiodynamic scans.

Appendix B

Table B-1 Room temperature tension OSA 0.2% offset yield strength data for different 5083-H116 damage states, with standard deviations. * denotes only two test samples at a given condition, all other tests had three replicates.

DoS Temp (°C)	DoS Level (mg/cm²)	Corrosion Time (hours)	Corrosion Surface	Corrosion Potential (V_{SCE})	OSA 0.2% offset YS (MPa)	OSA 0.2% offset YS σ (± MPa)
RT	3	0	NA	NA	276	2.9
100	31	0	NA	NA	259	0.2
100	53	0	NA	NA	256	1.0
100	53	120	LT	-0.77	253	0.8
100	53	120	LT	-0.755	238	10.3
100	53	120	LS	-0.755	232	1.0
150	20	0	NA	NA	248	1.6
150	20	120	LT	-0.77	249	2.2
150	20	120	LS	-0.77	250	1.9
150	51	0	NA	NA	242	1.6
150	51	48	LT	-0.77	222	4.6
150	51	120	LT	-0.77	206	5.8
150	51	120	LS	-0.77	189	2.6
150	>61	0	NA	NA	228	2.9
150	>61	120	LT	-0.77	154*	-

Table B-2 Room temperature tension OSA ultimate tensile strength data for different 5083-H116 damage states, with standard deviations.

DoS Temp (°C)	DoS Level (mg/cm²)	Corrosion Time (hours)	Corrosion Surface	Corrosion Potential (V_{SCE})	OSA UTS (MPa)	OSA UTS σ (± MPa)
RT	3	0	NA	NA	355	0.9
100	31	0	NA	NA	358	0.4
100	53	0	NA	NA	360	1.6
100	53	120	LT	-0.77	357	1.1
100	53	120	LT	-0.755	332	17.8
100	53	120	LS	-0.755	322	3.1
150	20	0	NA	NA	355	3.1
150	20	120	LT	-0.77	353	3.8
150	20	120	LS	-0.77	358	1.2
150	51	0	NA	NA	352	5.9
150	51	48	LT	-0.77	322	3.0
150	51	120	LT	-0.77	299	12.1
150	51	120	LS	-0.77	268	9.8
150	>61	0	NA	NA	342	3.0
150	>61	120	LT	-0.77	229*	-

Table B-3 Room temperature tension OSA elastic moduli data for different 5083-H116 damage states, with standard deviations.

DoS Temp (°C)	DoS Level (mg/cm²)	Corrosion Time (hours)	Corrosion Surface	Corrosion Potential (V_{SCE})	OSA E (GPa)	OSA E σ (± GPa)
RT	3	0	NA	NA	74	1.2
100	31	0	NA	NA	71	5.2
100	53	0	NA	NA	63	1.8
100	53	120	LT	-0.77	65	1.8
100	53	120	LT	-0.755	62	4.4
100	53	120	LS	-0.755	56	0.7
150	20	0	NA	NA	66	2.8
150	20	120	LT	-0.77	64	1
150	20	120	LS	-0.77	71	5
150	51	0	NA	NA	73	4.9
150	51	48	LT	-0.77	66	6.8
150	51	120	LT	-0.77	64	1.6
150	51	120	LS	-0.77	51	2.9
150	>61	0	NA	NA	71	1.4
150	>61	120	LT	-0.77	47*	-

Table B-4 Room temperature tension OSA %RA data for different 5083-H116 damage states, with standard deviations.

DoS Temp (°C)	DoS Level (mg/cm²)	Corrosion Time (hours)	Corrosion Surface	Corrosion Potential (V_{SCE})	OSA %RA (%)	OSA %RA σ (± %)
RT	3	0	NA	NA	15.39	0.59
100	31	0	NA	NA	14.12	0.36
100	53	0	NA	NA	14.49	0.69
100	53	120	LT	-0.77	13.22	0.08
100	53	120	LT	-0.755	14.06	1.14
100	53	120	LS	-0.755	10.80	0.86
150	20	0	NA	NA	15.04	0.22
150	20	120	LT	-0.77	17.24	0.83
150	20	120	LS	-0.77	15.33	0.66
150	51	0	NA	NA	17.26	1.85
150	51	48	LT	-0.77	15.09	0.16
150	51	120	LT	-0.77	20.44	1.90
150	51	120	LS	-0.77	9.13	3.08
150	>61	0	NA	NA	17.26	1.85
150	>61	120	LT	-0.77	35*	-

Table B-5 Room temperature tension PCSA 0.2% offset yield strength data for different 5083-H116 damage states, with standard deviations. * denotes only two test samples at a given condition, all other tests had three replicates.

DoS Temp (°C)	DoS Level (mg/cm²)	Corrosion Time (hours)	Corrosion Surface	Corrosion Potential (V_{SCE})	PCSA 0.2% offset YS (MPa)	PCSA 0.2% offset YS σ (± MPa)
RT	3	0	NA	NA	276	2.9
100	31	0	NA	NA	259	0.2
100	53	0	NA	NA	256	1.0
100	53	120	LT	-0.77	253	0.7
100	53	120	LT	-0.755	245	6.3
100	53	120	LS	-0.755	243	2.0
150	20	0	NA	NA	248	1.6
150	20	120	LT	-0.77	252	1.7
150	20	120	LS	-0.77	251	2.3
150	51	0	NA	NA	242	1.6
150	51	48	LT	-0.77	231	5.5
150	51	120	LT	-0.77	235	3.8
150	51	120	LS	-0.77	215	0.6
150	>61	0	NA	NA	228	2.9
150	>61	120	LT	-0.77	199*	-

Table B-6 Room temperature tension PCSA ultimate tensile strength data for different 5083-H116 damage states, with standard deviations.

DoS Temp (°C)	DoS Level (mg/cm²)	Corrosion Time (hours)	Corrosion Surface	Corrosion Potential (V_{SCE})	PCSA UTS (MPa)	PCSA UTS σ (± MPa)
RT	3	0	NA	NA	355	0.9
100	31	0	NA	NA	358	0.4
100	53	0	NA	NA	360	1.6
100	53	120	LT	-0.77	359	1.1
100	53	120	LT	-0.755	342	12.2
100	53	120	LS	-0.755	338	4.2
150	20	0	NA	NA	355	3.1
150	20	120	LT	-0.77	357	1.5
150	20	120	LS	-0.77	361	0.9
150	51	0	NA	NA	352	5.9
150	51	48	LT	-0.77	335	3.5
150	51	120	LT	-0.77	339	6.0
150	51	120	LS	-0.77	305	7.7
150	>61	0	NA	NA	342	3.0
150	>61	120	LT	-0.77	297*	-

Table B-7 Room temperature tension PCSA elastic moduli data for different 5083-H116 damage states, with standard deviations.

DoS Temp (°C)	DoS Level (mg/cm²)	Corrosion Time (hours)	Corrosion Surface	Corrosion Potential (V_{SCE})	PCSA E (GPa)	PCSA E σ (± GPa)
RT	3	0	NA	NA	74	1.2
100	31	0	NA	NA	71	5.2
100	53	0	NA	NA	63	1.8
100	53	120	LT	-0.77	66	1.8
100	53	120	LT	-0.755	64	3.3
100	53	120	LS	-0.755	59	0.6
150	20	0	NA	NA	66	2.8
150	20	120	LT	-0.77	65	0.7
150	20	120	LS	-0.77	71	5.1
150	51	0	NA	NA	73	4.9
150	51	48	LT	-0.77	69	7.0
150	51	120	LT	-0.77	72	1.4
150	51	120	LS	-0.77	58	2.5
150	>61	0	NA	NA	71	1.4
150	>61	120	LT	-0.77	62*	-

Table B-8 Room temperature tension PCSA %RA data for different 5083-H116 damage states, with standard deviations.

DoS Temp (°C)	DoS Level (mg/cm²)	Corrosion Time (hours)	Corrosion Surface	Corrosion Potential (V_{SCE})	PCSA %RA (%)	PCSA %RA σ (± %)
RT	3	0	NA	NA	15.39	0.59
100	31	0	NA	NA	14.12	0.36
100	53	0	NA	NA	14.49	0.69
100	53	120	LT	-0.77	12.94	0.07
100	53	120	LT	-0.755	11.56	1.21
100	53	120	LS	-0.755	6.33	0.57
150	20	0	NA	NA	15.04	0.22
150	20	120	LT	-0.77	16.48	0.36
150	20	120	LS	-0.77	14.63	0.55
150	51	0	NA	NA	17.26	1.85
150	51	48	LT	-0.77	11.44	0.59
150	51	120	LT	-0.77	7.94	1.25
150	51	120	LS	-0.77	-	-
150	>61	0	NA	NA	17.26	1.85
150	>61	120	LT	-0.77	7.44*	-